

“Linking Laboratory and *in situ* Activation Analysis of Rock-forming Elements using a 14 MeV Neutron Source”

1. The complexity and number of minerals contained in rocks cannot be described by a few elemental concentrations, so it is necessary to expand *in situ* delayed neutron activation measurements of elemental concentrations with as many elements as practical.
2. Activation analysis in a borehole differs substantially from laboratory neutron activation. The former uses high energy (14 MeV) neutrons and large samples with significant self-absorption, while the latter uses thermal (~0.025 eV) neutrons and small samples with negligible self-absorption.
3. Fast neutron sources cause n,p and n,α reactions of which the cross sections often have large uncertainties, and can produce the same activated nuclides from two or more different elements.
4. The predicted response integral, or inner product of the energy-dependent cross sections and the spatially- and energy-dependent neutron flux, can be evaluated by comparison to laboratory measurements of delayed gamma rays.
5. A weighted linear least-squares approach can be used to relate measured gamma-ray intensities to elemental concentrations, even when gamma rays with the same energy are produced by more than one element.
6. Fast neutron activation is affected most by changes in borehole geometry, while thermal neutron activation is primarily affected by the presence of absorbers. Both effects can be adequately determined and corrected by standard geophysical borehole techniques.
7. Simultaneous determination of silicon, aluminium, magnesium, sodium, calcium, iron, and potassium concentrations allows the normative calculation of feldspar, shale, and carbonate volumes.
8. Predictions of the borehole instrument sensitivity to 28 elements demonstrated that 20 additional elemental concentrations can be determined with a 10% precision provided stationary borehole measurements are used.
9. Serious mineralogical research and mineral excavation are acoustically incompatible.
10. Graduate studies are good at any time, but should ideally be completed before embarking on a career, getting married, having children, and reaching forty years of age.

Stellingen behorende bij het proefschrift

“Linking Laboratory and *in situ* Activation Analysis of Rock-forming Elements using a 14 MeV Neutron Source”

1. Aangezien neutronen-activeringsmetingen in boorgaten de complexiteit en het grote aantal mineralen in gesteenten niet eenduidig kunnen beschrijven als slechts de concentratie van een beperkt aantal elementen wordt bepaald, verdient het aanbeveling zoveel mogelijk elementen in de metingen te betrekken.
2. Neutronen-activeringsanalyse in het laboratorium is niet geschikt om de processen die optreden bij boorgatmetingen te beschrijven. In het boorgat worden hoog-energetische neutronen (14 MeV) gebruikt en absorbeert de formatie de straling. In het laboratorium worden thermische neutronen (0.025 eV) toegepast en speelt absorptie bijna geen rol.
3. Hoog-energetische neutronenbronnen veroorzaken n,p en n, α reacties waarvan de activeringsreactie doorsneden vaak onnauwkeurig bepaald zijn. Voorts kan bij deze bronnen eenzelfde isotoop afkomstig zijn van de activeringsreactie van verschillende elementen.
4. Laboratoriummetingen met gemodificeerde gammastraling kan gebruikt worden voor het voorspellen en verifiëren van de doorsnede van berekende activeringsreacties.
5. Ondanks het feit dat gammastraling met eenzelfde intensiteit uitgezonden kan zijn door meerdere elementen, kan een kleinste kwadraten methode worden gebruikt om de intensiteit van gammastraling te relateren aan elementenconcentraties.
6. De activering van hoog-energetische neutronen wordt vooral beïnvloed door veranderingen in de boorgatgeometrie, terwijl de activering van thermische (laag-energetische) neutronen voornamelijk wordt beïnvloed door de aanwezigheid van absorberende isotopen. Voor beide verschijnselen kunnen de neutronenmetingen met behulp van conventionele geofysische technieken worden gecorrigeerd.
7. De gelijktijdige bepaling van de concentraties silicium, aluminium, magnesium, kalium, natrium, calcium en ijzer, maakt het mogelijk om kwantitatief de hoeveelheden feldspar, klei, dolomiet en carbonaat te bepalen.
8. Indien neutronenmetingen in een boorgat zouden worden uitgevoerd met een stilstaand in plaats van een bewegend instrument dan kunnen nog 20 extra elementenconcentraties met een nauwkeurigheid van 10% worden bepaald.
9. Serieus mineralogisch onderzoek en het opgraven van mineralen zijn akoestisch niet te combineren.
10. De kennis en ervaring opgedaan tijdens een universitaire studie zijn immer van nut; het verdient echter aanbeveling deze studie te ondernemen alvorens aan een loopbaan te beginnen, te trouwen, kinderen te krijgen en een veertigste verjaardag te vieren.

Linking Laboratory
and *in situ* Activation Analysis
of Rock-forming Elements using a
14 MeV Neutron Source

**Linking Laboratory
and *in situ* Activation Analysis
of Rock-forming Elements using a
14 MeV Neutron Source**

Proefschrift

ter verkrijging van de graad van doctor
aan de Technische Universiteit Delft,
op gezag van de Rector Magnificus Prof.ir. K.F. Wakker,
in het openbaar te verdedigen ten overstaan van een commissie,
door het College van Dekanen aangewezen,
op vrijdag 6 oktober 1995 te 10.30 uur

door

Jerome TRUAX

Master of Arts in Oceanography and Limnology,
Western Connecticut State University

Bachelor of Science in Geological Engineering,
University of Minnesota

geboren te Pipestone, Minnesota USA



Dit proefschrift is goedgekeurd door de promotor:

Prof.dr. P.J. Ypma

Samenstelling promotiecommissie:

Rector Magnificus, voorzitter

Prof.dr. P.J. Ypma, Technische Universiteit Delft, promotor

Prof.ir. M. Peeters, Technische Universiteit Delft, co-promotor

Prof.dr.ir. J.T. Fokkema, Technische Universiteit Delft

Prof.dr. J. J. van Loef, Technische Universiteit Delft

Dr. R. Kreulen, UHD-U-Utrecht, Inst. Aardwetenschappen

Dr. J. Schweitzer, Schlumberger-Doll Res. Ridgefield USA

Prof.dr.ir. R.H. Heerema, Technische Universiteit Delft

Dipl.-Ing. J.K.Draxler, Hannover, Duitsland

CIP-DATA KONINKLIJKE BIBLIOTHEEK, DEN HAAG

Truax, Jerome

Linking laboratory and in situ activation analysis of rock-forming elements using a

14 MeV neutron source / Jerome Truax. - Delft : Delft University Press. - Ill.

Thesis Delft University of Technology. - With ref. - With summary in Dutch.

ISBN 90-407-1124-0

NUGI 841

Subject headings: neutron flux / activation spectrometry.

Copyright © 1995 by J. Truax

All rights reserved.

No part of the material protected by this copyright notice may be reproduced or utilized in any form or by any means, electronic or mechanical, including photocopying, recording or by any information storage and retrieval system, without permission from the publisher: Delft University Press, Stevinweg 1, 2628 CN Delft, The Netherlands.

Printed in The Netherlands

for Bernice and Tom

Support

Sponsorship by Schlumberger-Doll Research
is gratefully acknowledged by the author.

Table of Contents

Summary	1
Samenvatting	5
1 Introduction	9
1.1 Scope of the project	9
1.1.1 Overview	9
1.1.2 Issues and approaches	10
1.2 Motivation for the project	11
1.3 Borehole-conveyed neutron activation analysis	14
1.4 Comparison of well logging and TNAA	17
2 Scientific Base and Physical Principles	21
2.1 Neutron sources	21
2.1.1 (α ,n) Sources	22
2.1.2 Spontaneous fission neutron source	23
2.1.3 Neutron generators	23
2.2 Neutron interactions and cross sections	24
2.2.1 Elastic scattering	25
2.2.2 Inelastic scattering	28
2.2.3 Radiative capture	28
2.2.4 Particle production during absorption	29
2.3 Gamma ray interactions	29
2.3.1 Compton scattering	30
2.3.2 Photoelectric absorption	31
2.3.3 Pair production	32
2.4 Gamma ray detection and spectroscopy	32
2.4.1 Scintillators	33
2.4.1.1 Scintillation mechanism	33
2.4.1.2 Light collection and photomultipliers	34
2.4.1.3 Energy resolution of scintillator systems	35
2.4.2 Semiconductor spectrometers	37
2.5 Energy deposition in spectrometers	40
2.6 Neutron activation analysis fundamentals	45
2.6.1 Activation buildup and decay	45
2.6.2 Neutron activation cross sections in a mixed flux	47
2.6.3 Competing reactions in a mixed flux	47
2.6.4 Neutron activation in a large sample	48
2.6.5 Conflicting gamma ray energies	50
2.7 Counting statistics in pulse height spectroscopy	50
3 Borehole Nuclear Spectroscopy	53
3.1 Natural activity gamma ray spectroscopy	53
3.1.1 Direct calculation	58
3.1.2 Least squares fitting	59
3.2 Spectroscopy of γ -rays from inelastic neutron scattering	62
3.3 Spectroscopy of gamma rays from thermal neutron capture	68
3.4 Delayed activation gamma ray spectroscopy	68
3.5 Combinations of borehole spectroscopy measurements	69
3.6 Limitations of gamma ray spectrometers	70
3.7 Discussion and implications	70

4 Experimental Configuration	73
4.1 Considerations of the Experimental Design	73
4.1.1 Irradiation facility	74
4.1.1.1 Moderating medium	74
4.1.1.2 Structural aspects	76
4.1.1.3 Sample considerations	76
4.1.1.4 Neutron monitors	79
4.1.1.5 Safety aspects	80
4.1.2 Counting facility	80
4.1.2.1 Germanium detector	80
4.1.2.2 Counting cave	82
4.1.2.3 Data acquisition computer	83
4.2 Energy efficiency of the germanium detector	84
4.3 Summary	85
5 Experimental Procedures	87
5.1 Calculation of the effective source strength	87
5.2 The sample transfer procedure	89
5.3 Analysis of germanium spectra	90
5.4 Summary	95
6 Experimental Results	97
6.1 Magnesium	98
6.2 Sodium	100
6.3 Aluminum	102
6.4 Silicon	104
6.5 Response matrix	106
7 Monte Carlo Modeling of the Experiment	107
7.1 Description of Monte Carlo nuclear modeling	107
7.2 Modeling of neutron activation experiments	109
7.3 Raw modeling results	112
8 Comparison of Modeling and Experiments	115
8.1 Sources of inaccuracy in the comparison	115
8.1.1 Gamma ray transport efficiency	116
8.1.2 Gamma ray detection efficiency	116
8.1.3 Photopeaks and the pulse height spectrum	118
8.1.4 Neutron flux in the sample	118
8.1.5 Timing aspects of gamma ray counting	118
8.1.6 Effective neutron source strength	119
8.1.7 Mass and number of atoms, branching ratios	119
8.2 Normalization of experiments and model	119
8.3 Conclusions	122

9 Monte Carlo Modeling of a Sonde	125
9.1 Setup of the model	125
9.2 Elemental sensitivities in a shaly sand	129
9.2.1 Raw modeling results	131
9.2.2 Response matrix and synthetic data set	133
9.3 Magnesium detection in a carbonate	135
9.4 Environmental effects	136
9.4.1 Borehole conditions	136
9.4.2 Formation parameters	140
9.5 Summary and conclusions	141
9.5.1 Downhole measurement of Na, Mg, Al, Si in a shaly sand	142
9.5.2 Downhole measurement of Mg in a carbonate	143
9.5.3 Borehole environmental effects	143
9.5.4 Formation effects	143
10 Sonde Response to Other Elements	145
10.1 Method	145
10.1.1 Derivation of calibration factor	146
10.2 Results	149
10.3 Summary and conclusions	158
10.3.1 Method to predict the sonde response to other elements	158
10.3.2 Estimation of the sonde response to other elements	158
10.3.3 Limits of the measurement system	159
11 Conclusions	161
References	163
List of Symbols	167
Appendices	
A Effect of Detector Properties on Statistics	169
B Calculations of Neutron Spectra in Infinite Media	173
C Germanium Detector and Signal Electronics	181
D Neutron Monitors	185
E Sample constituents	189
F Isotopic and Nuclear Data	193
Acknowledgements	195
Curriculum vitae	197

Summary

This work examines the ability of a borehole-conveyed delayed neutron activation system to perform elemental analysis of earth formations with the combination of a neutron generator and a large germanium spectrometer. A downhole generator provides many more neutrons than a chemical source while substantially improving the level of personnel safety. High purity germanium spectrometers are now made large enough that detection efficiency rivals that of borehole-compatible scintillators.

The high energy of emitted neutrons, 14 million electron-volts, causes activation reactions in the formation that cannot be induced at significant levels with the less energetic neutrons from chemical sources. Moderation of the neutrons exposes the formation to all energies of neutrons below the emission energy, permitting thermal neutron activation, as well. Subsequent decay of the compound nuclei yields delayed gamma rays that indicate the presence of one or more elements. This indication is often not unique to a single element, because the same compound nucleus may arise from activation of more than one element.

Present borehole measurements using scintillators and chemical sources (^{252}Cf or $^{241}\text{AmBe}$) or D,T-type neutron generators ($^2\text{H} + ^3\text{H} \rightarrow ^4\text{He} + \text{n}$) can at best measure concentrations of ten elements (Si, Al, Ca, Fe, S, Ti, Gd, K, Th, and U). Important rock-forming elements, such as Na and Mg, as well as other important rock-forming elements and others of economic interest cannot be measured.

Elemental concentrations of silicon, aluminum, magnesium, and sodium are important quantities used in the characterization of rocks. A series of activation spectrometry experiments was performed on chemically pure compounds of these elements in a neutron moderating environment similar to what would pertain in a borehole measurement. Then, the geometry of the experimental setup was entered into a radiation transport modeling code based on a Monte Carlo process. The purpose of this exercise was to compare the measured responses with those predicted by the reaction cross sections in the library of the model, which are often ill-defined for high energy neutron interactions. Uncertainties for fast neutron reaction cross sections are significantly larger than for thermal neutron cross sections. The assumption

was made that all other aspects of the model replicated the experiment so well that any discrepancies must be due to an inaccurate representation of the cross sections in the model. Two magnesium reaction rates ($^{25}\text{Mg}(n,p)^{25}\text{Na}$ and $^{26}\text{Mg}(n,\alpha)^{23}\text{Ne}$) of the thirteen reactions studied displayed statistically significant discrepancies (a factor of 1.4 and 0.6, respectively) between measured and predicted responses.

The experimental results were also used to construct a response function for Na, Mg, Al, and Si, consisting of detected intensities at 14 different gamma-ray energy levels. The gamma rays were produced from the activated isotopes ^{24}Na , ^{27}Mg , ^{28}Al , ^{23}Ne , ^{20}F , ^{25}Na , and ^{29}Al , four of which are produced by competing reactions on two or more elements, e.g. $^{26}\text{Mg}(n,\gamma)^{27}\text{Mg}$, $^{27}\text{Al}(n,p)^{27}\text{Mg}$, and $^{30}\text{Si}(n,\alpha)^{27}\text{Mg}$. The response function can be inverted using a weighted least-squares technique to solve for elemental concentrations in a mixture of the elements, despite the presence of several competing reactions.

Next, the response of a neutron activation sonde was modeled using the Monte Carlo program and a neutron output of 10^9 n/s. The earth formations modeled were a dolomite and a shaly sand containing typical concentrations of sodium, magnesium, aluminum, and silicon. A response matrix was also constructed for the sonde, based on the same 14 gamma-ray energies observed in the experiments. For the shaly sand, magnesium density can be determined with a relative precision of 5%. Sodium, aluminum, and silicon densities can be measured with relative precisions less than 1%. In the modeled dolomite, magnesium density can be measured with a relative precision of 0.7%. The model contains an idealized representation of the detector response, so further studies should be performed to establish the precision attainable with a real detector.

Modeling calculations were performed to determine the sonde sensitivity to hole size, standoff, mud weight, salinity, formation density, and the presence of thermal neutron absorbers. Sonde standoff has a large deleterious effect on fast neutron activation and should be eliminated. The effect of chlorine and other absorbers upon the thermal activation response can be compensated using a measurement of the thermal neutron decay time. Other borehole and formation effects are minor or can be compensated.

The ratio of the modeled sonde response matrix to the experimental response matrix was calculated for the four rock-forming elements. The ratio was used in conjunction with a gamma-ray attenuation correction to generate a method of predicting the sonde response to *any* element, using the results of an

activation measurement of the element in the experimental facility. Logging responses were determined for sodium, magnesium, aluminum, silicon, and twenty-four other elements. Many of the additional elemental concentrations can be measured by stationary logging, including geochemically significant elements, such as Mn, Co, Sc, Br, Sr, and I, and elements of economic interest, such as Cu, Mo, Ag, Sn, and Au. A few elements, most notably V and Hf, are likely to be detected in a continuous measurement.

Samenvatting

Dit onderzoek behandelt de mogelijkheid om met behulp van neutronen-activerings analyse (NAA) gesteente-vormende elementen via een sonde in een boorgat kwantitief te analyseren. De sonde bestaat uit een neutronenbron en een stralingsspectrometer. Als neutronenbron wordt bij dit onderzoek een mini-versneller van het type D,T ($^2\text{H} + ^3\text{H} \rightarrow ^4\text{He} + \text{n}$) gebruikt. Deze bron genereert een neutronenstroom die verscheidene orden van grootte hoger is (10^8 tot 10^{10} n/sec) dan bereikt kan worden met de gebruikelijke chemische bronnen, welke bovendien milieu-technische bezwaren hebben. Als stralingsspectrometer wordt een met vloeibaar stikstof gekoelde Ge-halfgeleider gebruikt van grote zuiverheid (HPGe) en een dusdanig volume, dat de efficiëntie vergelijkbaar is met de gebruikelijke scintillatie-detectoren maar met een veel groter oplossend vermogen.

De hoge energie neutronen veroorzaken activeringsreacties in de formatie die de lagere energetische neutronen van de chemische bronnen niet kunnen teweegbrengen. Door botsingen met de formatie verliezen de neutronen energie, wanneer de energie laag genoeg is ontstaan thermale neutron activeringsreacties. Na activering van de nucleï vervalt deze weer terug naar een lagere energietoestand waarbij gamma energie vrij komt, uniek voor één of meerdere elementen. De uitgezonden gamma energie is vaak niet uniek voor één enkel element omdat eenzelfde activeringsproduct het resultaat kan zijn van de activeringsreactie van meer dan één element.

Huidige boorgat metingen gebruik makend van scintillatie-detectoren en chemische bronnen ($^{241}\text{AmBe}$ en ^{252}Cf) of D,T versnellers kunnen op zijn best de concentratie van tien elementen bepalen (Si, Al, Ca, Fe, S, Ti, Gd, K, Th en U). Belangrijke gesteente vormende elementen zoals Na en Mg en andere geochemisch en economisch interessante elementen kunnen niet bepaald worden.

De concentratie van Si, Al, Mg and Na zijn belangrijke grootheden voor de beschrijving van het gesteente. Activerings experimenten zijn uitgevoerd op chemisch zuivere verbindingen van deze elementen. Gebruik werd gemaakt van een proefopstelling die de spectrale samenstelling van de neutronen stroom in een boorgat zo dicht mogelijk benaderde. Een Monte Carlo programma voor neutronen en gamma stralings-transport is gebruikt om de gemeten resultaten

te vergelijken met gemodelleerde resultaten die berekend zijn met bekende relatieve neutronen doorsneden. Echter de waarden voor de relatieve activeringsreactie doorsneden bij neutronen van hoge energie zijn niet volledig bekend. De onzekerheid in de relatieve doorsneden voor de activeringsreactie bij hoog energetische neutronen is significant hoger dan die voor thermale neutronen. Aangenomen is dat het Monte Carlo model het experiment dermate goed simuleert dat ontstane verschillen alleen het gevolg kunnen zijn van onnauwkeurigheden in de gebruikte relatieve activeringsreactie doorsneden. Het bleek, dat - na normalisatie door middel van de nauwkeurig bekende thermale neutronen reacties - twee van de dertien reacties namelijk de $^{25}\text{Mg}(n,p)^{25}\text{Na}$ en de $^{26}\text{Mg}(n,\alpha)^{23}\text{Ne}$ aanzienlijk (resp. +2,1 en -4,0 standard deviaties) verschilden van de gemeten waarden, vanwege onjuiste gegevens betreffende neutronen doorsneden in het Monte Carlo bestand.

De experimentele resultaten van Si, Al, Mg and Na zijn gebruikt om een matrix van reactie vergelijkingen te creëren omdat vele intermediaire nucliden niet specifiek zijn voor een enkel element en het gamma stralings piek gebied een samengestelde waarde vertegenwoordigt. De veertien geproduceerde gamma pieken zijn afkomstig van het verval van de intermediaire producten: ^{24}Na , ^{27}Mg , ^{28}Al , ^{23}Ne , ^{20}F , ^{25}Na en ^{29}Al . Vier van de intermediaire producten zijn ontstaan uit de concurrerende activeringsreactie van twee of meer elementen (b.v. $^{26}\text{Mg}(n,\gamma)^{27}\text{Mg}$, of $^{27}\text{Al}(n,p)^{27}\text{Mg}$ of $^{30}\text{Si}(n,\alpha)^{27}\text{Mg}$). Met behulp van de kleinste kwadraten methode kan de matrix van reactievergelijkingen geïnverteerd worden om de concentratie van de verschillende elementen in een mengsel te berekenen ondanks de aanwezigheid van enkele concurrerende reacties.

Vervolgens is met het Monte Carlo programma de respons van de neutronen activerings sonde gemodelleerd waarbij een neutronen intensiteit van 10^9 n/s werd aangehouden. De gemodelleerde gesteenteformaties zijn een dolomiet en schalie-houdende zandstenen welke kenmerkende concentraties Na, Mg, Al en Si bevatten. Een matrix van reactie vergelijkingen voor de sonde is opgesteld gebaseerd op dezelfde veertien gamma stralings energiën geobserveerd in de experimenten. De magnesium dichtheid voor een schalie-houdend zand kan met een relatieve fout van 5% berekend worden. Natrium, aluminium en silicium dichtheden kunnen berekend worden met een relatieve fout kleiner dan 1%. In een dolomiet kan de magnesium dichtheid met een relatieve fout van 0.7% bepaald worden. Het model geeft een geïdealiseerde

voorstelling van de detector respons weer, verder onderzoek moet gedaan worden om de precisie bij gebruik van een echte detector te bepalen.

Het sonde model is tevens gebruikt om de invloed van boorgat diameter, excentriciteit van de sonde, soortelijk gewicht van de spoeling en neven gesteente, zoutgehalte van formatie water, en de aanwezigheid van neutronen absorberende elementen te bepalen. Wanneer de sonde niet goed tegen de boorgatwand geplaatst is zal het aantal hoge energie neutron activeringsreacties drastisch verminderen wat voorkomen zal moeten worden. Het effect van chloor en andere neutronenvangers op de thermale activerings respons kan gecompenseerd worden met thermale neutron verval tijd metingen. Ander boorgat en formatie effecten zijn minimaal of kunnen worden gecompenseerd.

De verhouding tussen de gemodeleerde sonde matrix en de geexperimenteerde matrix is bepaald voor de vier gesteente vormende elementen. Deze verhouding is samen met de gamma straling verzwakkings correctie gebruikt om een methode te ontwikkelen die de sonde respons van elk element kan voorspellen. Deze methode maakt gebruik van de resultaten van geexperimenteerde activeringsreactie metingen van een element. Sonde respons waarden zijn bepaald voor natrium, magnesium, aluminium, silicium en vierentwintig andere neven-elementen. Het bleek dat maar weinigen van de 24 onderzochte neven-elementen in de te verwachten concentraties met een continu bewegende sonde (180 m/uur) bepaald kunnen worden. Behalve voor Hf en V zijn stationaire metingen nodig, maar dan kunnen ook geochemisch interessante elementen zoals Mn, Co, Se, Br, Sr, en I, en elementen van economisch belang zoals Cu, Mo, Ag, Sn, en Au in het boorgat bepaald worden.

1.1 Scope of the project

1.1.1 Overview

Wireline logging tools are sensor-equipped instruments that are suspended in a borehole at the end of an electrical cable. The tools measure a large range of physical properties of the subsurface layers penetrated by the borehole, most commonly electrical resistivity, acoustic wave velocity, and attenuation of neutrons and gamma rays. Gamma-ray spectroscopy is also used routinely in several ways to determine elemental concentrations in the earth formations. The energy spectra of naturally occurring gamma rays in the layers are used to measure concentrations of K, Th, and U. Spectroscopy of prompt gamma rays induced by neutron interactions is routinely performed to derive concentrations of Si, Ca, Fe, S, Gd, and Ti or the relative concentrations of C and O. Analysis of delayed gamma rays induced by neutrons is currently restricted to Al because of limitations in the measurement system.

The purpose of this research project is to expand the capabilities of borehole-conveyed delayed neutron activation spectrometry for elemental analysis of earth formations. Goals consist of an increase in the number of measurable elements, and an improvement in statistical and systematic robustness through inclusion of fast neutron activation reactions in the analysis. Much of the focus is on the measurement of sodium, magnesium, aluminum, and silicon concentrations, which are all important rock-forming elements. Concentrations of Na and Mg cannot be measured with existing borehole instruments, and are of paramount importance for the evaluation of feldspars, clays, and mica.

Recent advances in accelerator and detector technologies provide the potential for expansion of an *in situ* neutron activation measurement. High purity germanium spectrometers can now be manufactured large enough that absolute detection efficiencies and peak-to-Compton ratios are greatly enhanced over what has been previously available. Additionally, downhole accelerators that are capable of generating high energy neutrons at a rate one hundred times that of practicable isotopic sources are now realizable. The combination of an efficient detector and a high output accelerator in an activation sonde raises several research issues that are addressed in this thesis.

1.1.2 Issues and approaches to issues

In contrast with thermal neutron activation analysis (TNAA), where the capture cross sections of elements are usually very precisely known, the cross sections that govern the interaction between fast neutrons and nuclei are often ill-defined. Also, the neutron flux in a borehole measurement is disturbed by the borehole fluids and the earth formation itself, and the sample size is not fixed due to the variation in neutron transmissive and absorptive properties of the layers.

When high energy neutrons are used in a bulky medium, there is exposure of the medium to the entire energy range as neutrons lose energy from the emission energy to thermal levels. Activation reactions in this type of neutron flux, with continuous energy distribution, can be broadly classified into two groups. Thermal neutron activation occurs following capture of a slow neutron, and fast neutron activation occurs when an energetic neutron is absorbed by a nucleus, which typically ejects a proton, alpha particle, or two or more neutrons. Several kinds of activated nuclei may often be created from an element, which are partially or wholly indicative of the element. Each activated nuclide may not be entirely diagnostic of the element because of competing reactions from other elemental targets that result in identical activated nuclides.

Reactions leading to multiple activated nuclides from the same element, a positive aspect of a fast neutron source, and the competing reactions, a negative aspect, must be well characterized to ensure a meaningful elemental analysis. Most of the work in this thesis is directed toward that end.

The reaction rate cross sections relevant to a high energy neutron source typically have large uncertainties in their published values. This can lead to ambiguities in the response of a sonde, especially in the instances of competing reactions populating an activated nuclide. A method is developed to evaluate high energy neutron cross sections, by the performance of activation measurements on small samples in a neutron flux similar to what would pertain in a borehole environment. Monte Carlo calculations are made from the published cross sections and a model of the experimental geometry. Comparison of the experimental and modeling results leads to an integral evaluation of the cross sections. The method is applied to sodium, magnesium, aluminum, and silicon activation cross sections.

When there are multiple gamma rays from each element, and some of the gamma rays may be indicative of more than one element, an inversion technique must be developed to solve for the elemental concentrations. A response matrix is constructed from the experimental data, and a weighted least

squares technique is developed and its statistical performance examined for the case where sodium, magnesium, aluminum, and silicon are present.

A modeled representation of a possible sonde is also used to perform Monte Carlo calculations of responses to sodium, magnesium, aluminum, and silicon concentrations in earth formations. The cross section evaluations performed earlier are used to adjust the calculated responses based on the assumption that the spatially dependent neutron flux is similar to that of the experiments. A response matrix is constructed, a weighted least squares inversion process is developed to solve for the elemental concentrations, and its statistical performance is examined.

In a borehole geometry, an activation sonde will be sensitive to borehole and formation environmental parameters in addition to elemental concentrations of the formation. Monte Carlo calculations of the sonde response are made for several environmental conditions. Hole size, tool standoff, mud weight and salinity, and formation density and salinity are varied to determine the range and relative importance of the effects on both thermal and fast neutron activation.

Observations of the response matrices from experiments and the sonde model lead to the development of a method to determine the sonde response to concentrations of any element, utilizing laboratory activation measurements on a small sample. This method is applied to determine the sonde response to concentrations of twenty-four additional elements in an earth formation.

1.2 Motivation for the project

Nuclear logging techniques in boreholes were first used in 1939 [1], about a dozen years after the invention of wireline logging, and only several decades after the discovery of radioactivity. Since then, there have been several generations of nuclear logging sonde design, particularly for gamma-gamma density logging [2,3], neutron porosity logging [4], natural gamma-ray logging [5], and thermal neutron decay logging [6]. These outstanding inventions, along with resistivity and acoustic logging techniques, have become the mainstay of formation evaluation and assessment of prospective petroleum reservoirs. They are used at least once in nearly every wellbore for estimation of reserves and producibility.

Nuclear logging systems to record elemental concentrations were introduced to the oil industry in 1974 [7,8]. Currently, concentrations of ten elements can be continuously recorded from the borehole in a single pass with an elemental analysis system [9]. These are either the main constituents of the

rock or a few of the lesser constituents whose nuclear properties make them unusually easy to measure. The measurable elements are:

Si, Ca, Al, K, Fe, S, Ti, Th, U, and Gd.

Large signals are also obtained from chlorine and hydrogen, which are associated mostly with the fluids rather than the rock. The ratio of carbon to oxygen, used to estimate hydrocarbon saturation, may also be measured [7] by making an additional descent into the wellbore. In the above list of elements, only aluminum is currently measured by delayed neutron activation [9,10].

A set of elemental logs from a sand, shale, and lime sequence is illustrated in Figure 1-1 [11]. The continuous traces are log-derived elemental concentrations, which are plotted on the same scale as thermal neutron activation analysis data obtained from core samples. Agreement between the two methods is outstanding. Elemental logs such as these are utilized in a variety of scientific projects [13-15, 24], as well as in the oilfield.

There is a potential ability to add many more elements to this list by means of downhole neutron activation analysis, using a miniaturized neutron generator and taking advantage of recent improvements in high-purity germanium gamma-ray detector technology. The rock-forming elements magnesium and sodium are the most obvious candidates for addition to the list of measurable elements because they often comprise significant percentages of the rock matrix, and possess favorable nuclear properties. Inclusion of these rock-forming elements will be beneficial to mineralogical interpretation of elemental analyses. Estimates of feldspar, clay, and mica content and type can be improved [16-18]. In carbonate reservoirs, dolomitic content can be determined. For reasons that will be more fully explained in the following chapters, the measurement of magnesium and sodium concentrations necessarily involves the simultaneous measurement of aluminum and silicon [19], thus sensitivities to these elements will also be studied.

A continuous borehole log of additional elemental concentrations has the potential to enhance geochemical analyses of oilfield strata [17,20] and to enhance efficiency of mineral exploration and orebody delineation in the mining industry [21]. Elements which are geochemically interesting or economically significant include Sc, Ti, V, Cr, Mn, Fe, Co, Ni, Cu, Zr, Ag, Hf, and Au. While it is not expected that an elemental log could entirely supplant more conventional assay methods, it has the possibility of being used as a supplemental screening technique.

For example, in a potential orebody containing disseminated gold, a continuous log of gold concentration could provide a delineation of acceptable levels of gold *in place*, providing a basis for further investigation such as fire assay to determine *extractable* gold.

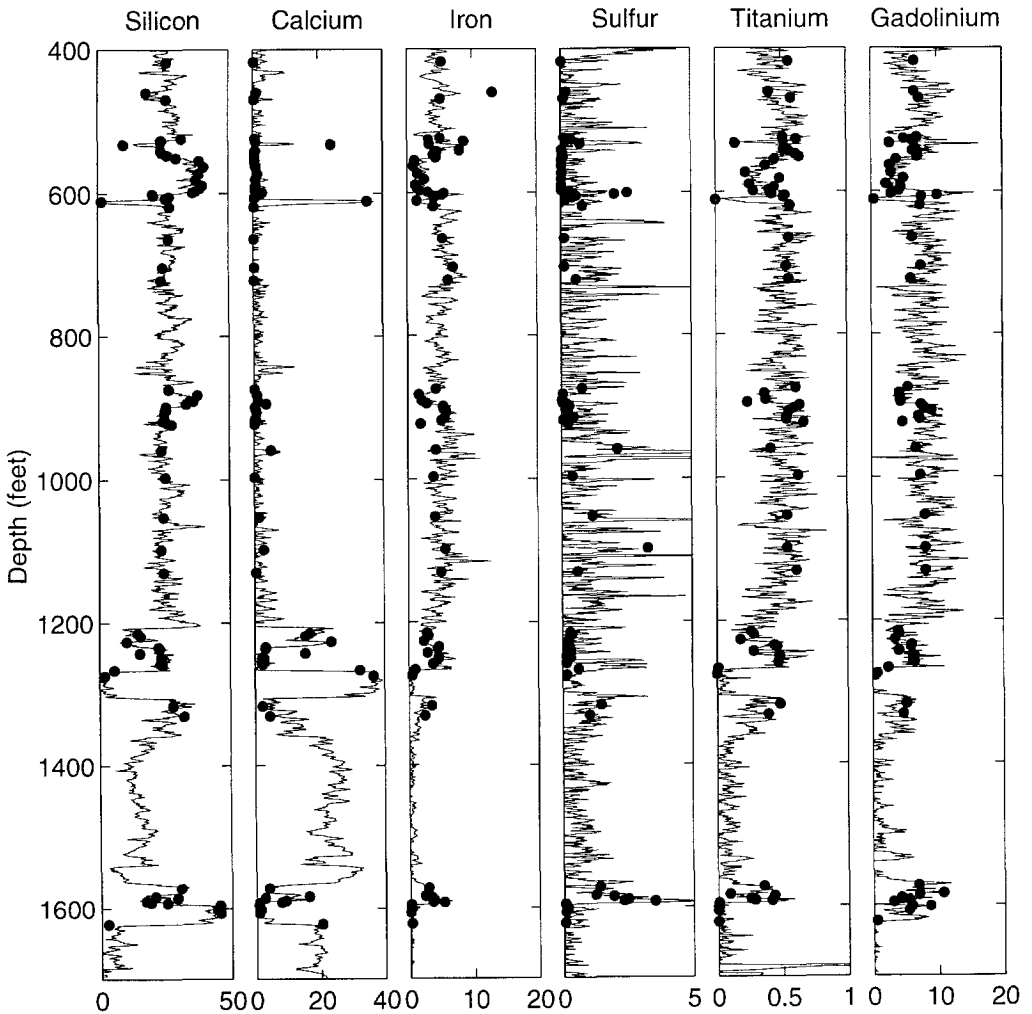


Figure 1-1 A comparison between core and log elemental concentrations shows excellent agreement and demonstrates the attainable accuracy and precision of elemental logging. Concentrations are in percent by weight, except gadolinium, which is stated in parts per million. Data provided by Susan Herron.

1.3 Borehole-conveyed neutron activation analysis

A downhole neutron activation measurement system and techniques will be summarized in this section. For detailed discussions of the applicable neutron and gamma-ray physics, please see Chapter 2. The current status and experience of several borehole nuclear spectroscopy methods are outlined in Chapter 3, including neutron activation analysis for aluminum concentration. A sonde for activation analysis would essentially consist of a neutron source and a gamma-ray spectrometer, as shown in Figure 1-2. The source-to-detector spacing is at least two meters, and neutron shielding material may occupy some of the intervening space. The relatively large spacing ensures that there will be no significant detection of prompt gamma ray activity. Additionally, activation of the detector region of the sonde itself will be reduced to an insignificant level because of the long spacing and the neutron shielding material.

As the sonde is pulled upward, the neutron source irradiates the earth formation, causing activation of a small fraction of atoms by nuclear interactions. A few species of activated nuclei are stable, but many undergo a decay with a characteristic half life. Emission of one or more gamma rays usually accompanies the decay, with gamma-ray energies that are characteristic of the activated nuclei. The spectrometer, trailing behind, samples the gamma-rays, which results in a pulse height spectrum similar to that of Figure 1-3. Each peak in the spectrum comes from the decay of a specific nuclide. The measured area of a peak is adjusted for variations in gamma-ray detection efficiency, neutron source intensity and corrected for logging speed using the known half life. The corrected peak area will then be proportional to the mass concentration of the original isotope. Deviations from proportionality of the response will result from a variety of environmental conditions, including borehole size and rugosity, sonde standoff and tilt, mud weight and salinity, formation density, and formation water salinity.

Another possible logging technique involves stationary measurements. The sonde is held in a single position with its neutron source adjacent to the formation of interest. After a suitable time, the sonde is moved uphole so that the gamma-ray spectrometer is adjacent to the activated formation. While delayed gamma-ray activity is being recorded, the neutron source is activating the next station level of the formation. Regular station intervals may be attained in this manner.

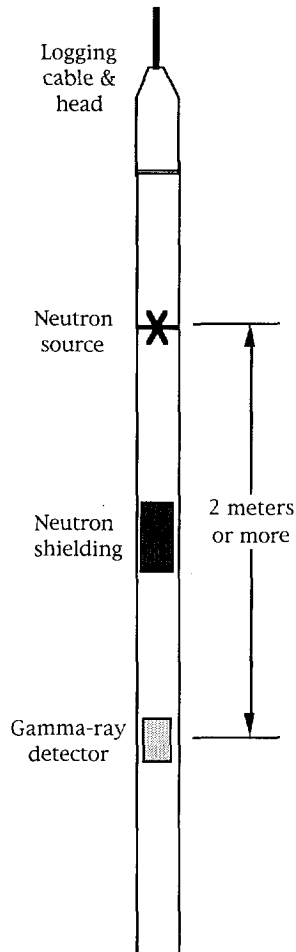


Figure 1-2. Schematic illustration of a possible neutron activation sonde. A pulsed or non-pulsed neutron generator, or a radioisotope neutron source may be used. For this project, a non-pulsed neutron generator is used. The large spacing prevents detection of any prompt gamma-ray activity.

The neutron source may be an encapsulated chemical source or an accelerator source. Pulsing of the accelerator has no bearing on the measurement. All timing required by the measurement is determined by the half-life, the logging speed, and the spatial separation of source and detector. The use of a miniaturized neutron generator can provide 10 to 100 times more neutrons than is practical with a radioisotope source while substantially

improving the level of personnel safety. The high energy of emitted neutrons, 14 MeV, * causes activation reactions that cannot be seen when less energetic sources are used. The reactions may be diagnostic of an element, but more typically create identical activated nuclei from several different types of atoms.

For example, high energy neutrons may react with ^{28}Si atoms, causing the formation of activated ^{28}Al nuclei. As the neutrons slow down to thermal levels, they may react with ^{27}Al atoms to also form activated ^{28}Al nuclei. These *competing reactions* must be understood and accommodated in the elemental analysis. The reaction *cross sections*, or effective nuclear areas for the neutron reaction, can be used to predict the reaction rates, but estimates of the cross sections for the high energy reactions have large uncertainties in most cases.

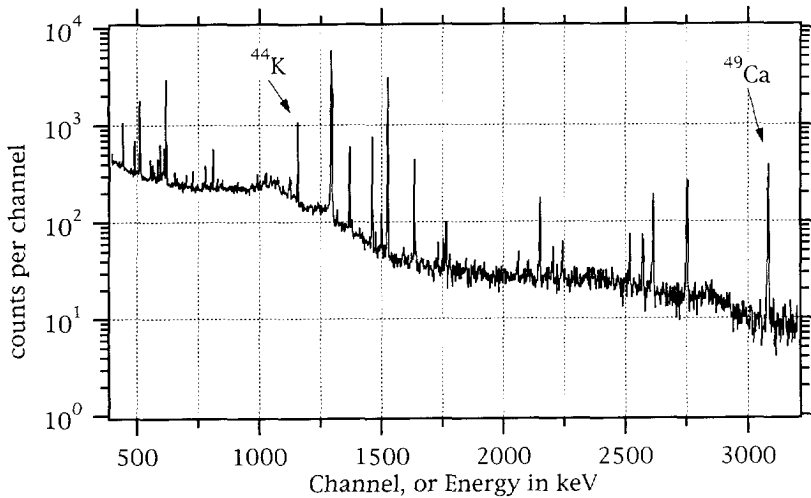


Figure 1-3. An activation pulse height spectrum obtained from limestone, using a neutron generator and a high-purity germanium spectrometer. The peak at 3084 keV is from the decay of ^{49}Ca , which is formed from ^{48}Ca by a thermal neutron capture reaction, and has a half-life of 8.72 minutes. The peak at 1157 keV is one of many that results from the 22 minute half-life decay of ^{44}K , formed when a fast neutron is absorbed by ^{44}Ca and a proton is ejected. Similar descriptions may be written for each peak in the spectrum.

* The unit of energy used throughout the discussion is the electron-volt (eV), equal to the kinetic energy gained by an electron when accelerated by a potential of one Volt. Thousands and millions of electron-volts (keV) and (MeV) are convenient units, also. There are also some broad classifications of neutrons according to their energies. Thermal neutrons have a distribution of energies around 1/40 eV, the epithermal range extends up to several eV, and the fast neutron range is above this.

The gamma-ray spectrometer may be a scintillator or a semiconductor. Features of these detectors are discussed in the next chapter. The semiconductor detectors inherently possess excellent gamma-ray energy resolution, but have suffered from low detection efficiency due to their small size. Recent industrial capability for growth of large high-purity germanium has developed to the point that crystals of 400 cm³ volume are commercially available for use as high resolution gamma-ray detectors.

1.4 Comparison of well logging and TNA

Features of a well-logging activation measurement differ substantially from thermal neutron activation analysis (TNA) as it is usually performed. The differences are summarized in Table 1-1.

Feature	TNA	Well Logging
Neutron energy	Thermal neutrons (reactor)	Fast neutrons (accelerator or isotopic source)
Neutron source intensity	10^{13} n/sec/cm ²	10^8 to 10^{10} n/sec/4 π
Sample effects	Thin sample, little or no self-shielding	Bulky sample, self-shielding and moderation of neutrons and gamma rays
Sample size	Well-defined sample geometry	Unknown sample dimensions
Environmental conditions	Standardized measurement conditions	Unknown and variable conditions (borehole and formation fluids, and sonde application)
Acquisition times	Suitable activation, delay, and measurement times	Brief acquisitions (seconds or a few minutes)
Activated nuclides	One activated nuclide per measured element	Usually two or more activated nuclides per measured element
Complexity of data	Unambiguous spectral data	Ambiguities from competing reactions populating the same activated nuclide
Cross sections	Well known	Large uncertainties

Table 1-1 Many aspects of a borehole-conveyed neutron activation measurement are dissimilar to the conditions of traditional thermal neutron activation analysis.

The first two measurement features are the neutron energy and source intensity. When TNAA is performed at a reactor site, the energy distribution of the neutron flux in the irradiation area is well known. The flux is typically nearly all thermalized, with perhaps one epithermal neutron in several hundred thermal neutrons. [22] Typical flux intensities are on the order of 10^{13} n/sec/cm². Borehole-compatible sources, whether accelerators or isotopic, emit fast neutrons. For example, the accelerator used in this project emits neutrons at 14 MeV. The output intensity from accelerators of this type range from 10^8 to 10^{10} n/sec/4 π .

Samples in TNAA are generally very thin, particularly when compared to the mean free path of the incident neutrons, so that attenuation of neutrons and gamma rays in the sample is very small. This will not be the case for an *in situ* measurement. The energy distribution of the neutron flux will vary spatially within the sampled region, and will also differ between samples. In general, the distribution of the neutrons and their energy spectrum is controlled by three main parameters of the sampled region: bulk density, hydrogen index, and presence of absorbers such as chlorine, boron, and gadolinium [23]. The sampling region is also large compared to the mean free path of photons in the media, leading to scattering and absorption that will have an effect on the number of full-energy photons reaching the detector. This effect is essentially dependent on the density of the formation. The neutron and gamma ray self-shielding also leads to uncertainty in the extent of the sampled region, an effect also listed in Table 1-1.

Environmental conditions, such as the size and shape of the borehole, and the fluid content of the borehole and formation, also have an effect on the neutron and gamma-ray transport and interactions. Replicable and adequate application of the sonde to the formation is a problem that affects most downhole measurements. Additionally, measurements must typically be performed in a few seconds for a continuous log, or a few minutes for a station measurement.

The last three rows of Table 1-1 list further consequences of using a fast neutron source for an *in situ* measurement. The use of a well-thermalized source in TNAA makes the analysis much simpler because each activated state can arise from only a unique elemental isotope. For a *purely thermal* flux, the decay of ²⁴Na, for example, with a half-life of 15.02 hours and the emission of gamma rays at 1368.6 and 2754.1 keV, is entirely diagnostic of the sodium content of a sample. In this case, the intermediate nuclide must have arisen

from the thermal neutron reaction $^{23}\text{Na}(n,\gamma)$ (Notation explained in footnote †). See Table 1-2, which is a compilation of the sodium, magnesium, aluminum, and silicon activation reactions useful in an in situ measurement. Thermal neutron activation reactions are entered in bold typeface.

A fast neutron source brings into consideration the n,p and n,α reactions that have thresholds of a few MeV, resulting in the production of identical activated nuclides from two or more original elements. For the case of the activated nucleus ^{24}Na mentioned above, we must now also consider contributions to the activation from the MeV-energy-range reactions $^{24}\text{Mg}(n,p)$, and $^{27}\text{Al}(n,\alpha)$.

initial nuclide	reaction	intermediate nuclide	half-life	γ rays (keV)
^{23}Na ^{24}Mg ^{27}Al	(n,γ) (n,p) (n,α)	^{24}Na	15.02 h	1368.6, 2754.1
^{26}Mg ^{27}Al ^{30}Si	(n,γ) (n,p) (n,α)	^{27}Mg	9.45 m	843.8, 1014.4
^{27}Al ^{28}Si	(n,γ) (n,p)	^{28}Al	2.246 m	1778.8
^{23}Na ^{26}Mg	(n,p) (n,α)	^{23}Ne	37.6 s	439
^{23}Na	(n,α)	^{20}F	11.0 s	1633.1
^{25}Mg	(n,p)	^{25}Na	60 s	390.7, 585.9, 975.2, 1611.9
^{29}Si	(n,p)	^{29}Al	6.52 m	1273, 2028, 2426

Table 1-2 Seven intermediate nuclides from sodium, magnesium, aluminum, and silicon result in decay gamma rays potentially detectable in a borehole device. Four of the seven intermediate nuclides have competing reactions leading to them. Thermal neutron reactions are entered in bold typeface. There are more possible reactions from Na, Mg, Al, and Si that are not suitable for further consideration because of their half-lives, cross sections, or branching ratios. The thermal neutron activation of ^{30}Si is omitted for these reasons.

† A notation used often in the discussion of particle interactions has the form (x,y) , where x represents a particle type incident on a nucleus, and y represents a particle subsequently emitted from the nucleus. n - neutron; p - proton; α - alpha particle; γ - gamma ray

The common rock forming elements sodium, magnesium, aluminum, and silicon include several of these competing reactions, listed in Table 1-2. In addition to the competing reactions, the fast neutrons introduce additional reactions so that, there are now seven measurable activities from which the concentrations of the four elements can be determined. Published estimates of energy-dependent cross sections for the fast neutron reactions listed in Table 1-2 have large uncertainties [19], making their use difficult in calculating the response of an activation sonde.

The purpose of this chapter is to review the basic principles of radiation interaction and detection that pertain to well-logging measurements of delayed neutron activation. This compilation is undertaken because features of the well-logging measurement differ substantially from thermal neutron activation analysis (TNAA), as discussed in the preceding chapter. The chapter will be elementary for nuclear physics-oriented readers, but is intended to bring together diverse aspects of neutron and gamma-ray physics to provide background for the following chapters, particularly for readers distant from the nuclear physics field.

A well-logging measurement sonde uses a fast neutron source to activate a bulky region of the earth formation under uncertain and variable conditions. The formation, borehole, and sonde cause scattering and slowing down of the neutrons, exposing the formation to a continuous energy distribution of neutrons, down to thermal energies. More than one type of activation reaction is then possible for most elements contained in the formation. The same activated nuclide may be created from two or more original elements in this environment. Gamma rays produced by the decay of activated nuclei may also undergo scattering in the sampling region before detection by the spectrometer.

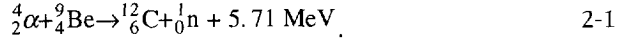
This chapter begins with a discussion of various neutron sources applicable to a borehole-conveyed instrument. The nature and behavior of neutron interactions with materials will be described, including interactions leading to gamma-ray production. Photon transport and interactions with materials will be discussed, and methods of gamma-ray detection and spectroscopy will be presented. The chapter will be completed by a brief discussion of counting statistics applicable to neutron activation.

2.1 Neutron sources

There are three main practical types of neutron sources applicable to use in well logging, each with significant advantages and disadvantages for specific applications [25]. The first two types use radioisotopes, and are usually referred to as "chemical" sources. The third type of source is a deuterium accelerator.

2.1.1 (α, n) Sources

When an energetic alpha particle strikes an appropriate target material there is a small likelihood, about 0.01%, that a neutron will be produced [26]. The first, most common, and most efficient material to be used as a target is beryllium, where neutrons are produced by the following reaction.



As an alpha-particle emitter, ${}^{241}\text{Am}$ is convenient in terms of its specific activity of decay and 433 year half-life, and it is commonly used. Intimate mixtures of the americium and beryllium are constructed with relative proportions of the two materials such that the neutron yield is maximized. The energy distribution of the neutrons is broadly peaked at about 4 MeV, and extends beyond 10 MeV (Figure 2-1).

Reliable encapsulation of the sources for use in wellbores has been achieved using a welded, double wall stainless steel pressure vessel construction. The requirements for limited physical size of the pressure vessel and source, as well as safety concerns, limit the achievable source output to about 5×10^7 n/sec for a ${}^{241}\text{AmBe}$ source.

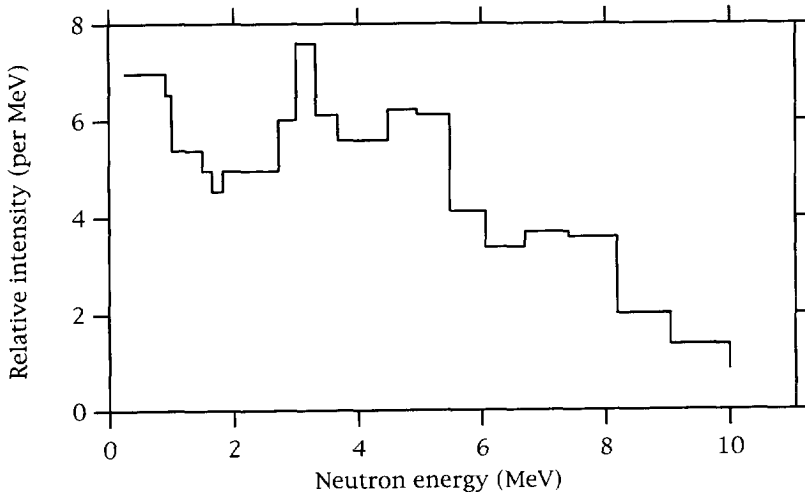


Figure 2-1 The measured energy spectrum of a 4×10^7 n/s ${}^{241}\text{AmBe}$ source. [27]

2.1.2 Spontaneous fission neutron source

As a source of neutrons, ^{252}Cf is the most widely used of the spontaneously fissionable transuranic elements. The neutron production rate is 2.3×10^6 n/s per microgram of ^{252}Cf , thus only about 50 micrograms of material are required for a source approaching the reasonable limits of safety considerations, or about 1.2×10^8 n/s. The californium is usually encapsulated in a pressure vessel similar to that of an (α, n) source, with thick walls to stop unwanted beta particles, low energy x-rays, and heavy fission products. The half-life of ^{252}Cf is 2.65 years, making it somewhat inconvenient for use in well logging because of the replacement expense as the neutron output falls off.

The energy distribution is peaked between 0.5 and 1 MeV (Figure 2-2), making it convenient for use in certain types of neutron-induced gamma ray spectroscopy measurements, as will be explained in later sections. However, there is an exponential tail of the energy distribution that extends above 10 MeV.

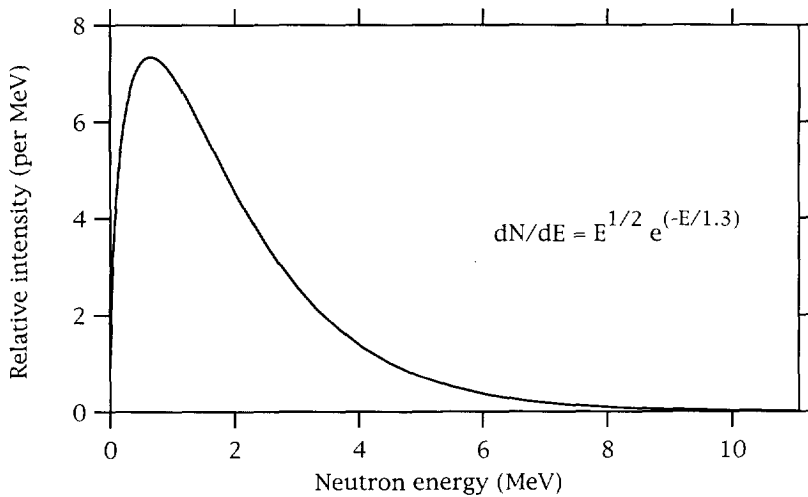
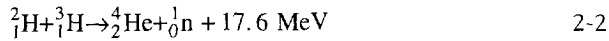


Figure 2-2 Calculated neutron energy spectrum from the spontaneous fission of ^{252}Cf . [28]

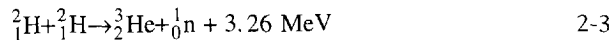
2.1.3 Neutron generators

Miniaturized accelerators, small enough to be accommodated in production logging equipment, have been used as neutron sources in wellbores for a few decades [29, 30]. They consist of a high voltage power supply and a sealed tube containing a target and a source of ions. Most are based on what is known as the D-T reaction, deuterium ions that are accelerated into tritium targets by potentials of perhaps 100 kilovolts.



Some of the energy from this reaction is taken up by the recoil alpha particle, leaving 14 MeV as the emission energy of the neutron. There is a very slight angular dependence of both the neutron energy and the intensity, which for practical purposes may be ignored. Outputs of approximately 10^9 n/s can be achieved.

Neutron energy from the D-D reaction is about 2.5 MeV, making it attractive for certain types of measurements. The D-D reaction is less commonly utilized, however, because of the diminished output intensity that can be achieved, approximately 100 times less than the D-T reaction for the same operating conditions of the accelerator.



A distinct advantage of neutron generators is that they can be switched on and off at will, making them much safer than encapsulated sources. They can be cyclically switched on and off (pulsed) in the microsecond time regime in such a manner that timing of the resulting radiations can be recorded. Another advantage is that source outputs can be considerably greater than those of encapsulated chemical sources. Output depends on the accelerator design and operating conditions, and can range from 10^8 to 10^{10} n/sec. Neutron generators are more expensive, however, and require some maintenance for proper operation. Reliability has improved over the years, but the sealed tube and high voltage sections of the accelerator occasionally experience failures, and must be repaired or replaced.

2.2 Neutron interactions and cross sections

Lacking any charge, neutrons do not interact by Coulomb forces as charged particles do, but slow down by scattering from nuclei as they penetrate matter, or they are absorbed by a nucleus [31]. Neutrons can traverse many centimeters of earth materials without any interaction. The average distance of travel without interaction, termed the *mean free path*, is about 7 centimeters in limestone for a 14 MeV neutron [32]. Because of this penetrating nature and the features of their four main types of scattering and absorption reactions, explained in the following sections, neutrons provide a good means of investigating the properties of earth materials. The rate for a scattering or absorption reaction Y_i is given by the following expression [33].

$$Y_i = N\phi\sigma_i \quad 2-4$$

Neutron flux ϕ is defined to be the product of number density of neutrons (number/volume) and their velocity (length/time). Flux thus has dimensions of number/area/second and is usually expressed as n/cm²/s. N is the number of target nuclei, and σ is the cross section for the reaction of type i . The cross section is the effective size of a target nucleus for the reaction and has the dimensions of area, usually stated in barns, where 1 barn = 10⁻²⁴ cm². Both the cross section and the neutron flux typically vary strongly with neutron energy E . Typical cross section dependencies on energy are illustrated in Figure 2-3(a-d), and will be discussed in the following sections.

The macroscopic cross section Σ for a particular reaction is a useful bulk property of a material. It is the reciprocal of the mean free path discussed earlier, and thus has dimensions of inverse length, representing the probability of a reaction occurring in unit length.

$$\Sigma = \sigma \frac{N_{Avo}\rho_b}{A} \quad 2-5$$

In this expression ρ_b is bulk density (g · cm⁻³), A is atomic mass (g · mole⁻¹), σ is the cross section (cm²) and N_{Avo} is Avogadro's number (mole⁻¹), meaning that the macroscopic cross section Σ has units cm⁻¹.

2.2.1 Elastic scattering

Scattering can occur either elastically or inelastically. In elastic scattering, total kinetic energy of the neutron and target nucleus remains constant. Figure 2-3(a) is a plot of elastic scattering cross section with energy, for magnesium. The elastic cross sections are usually about 1 barn. The neutron slows down, or *moderates*, by imparting a fraction of its kinetic energy to the struck nucleus. The amount of energy given up depends on the scattering angle and the mass A of the nucleus [32]. It can be shown through a kinematic analysis that the fraction of energy remaining with the neutron is

$$f = \frac{A^2 + 2A \cos \Theta + 1}{(A + 1)^2} \quad 2-6$$

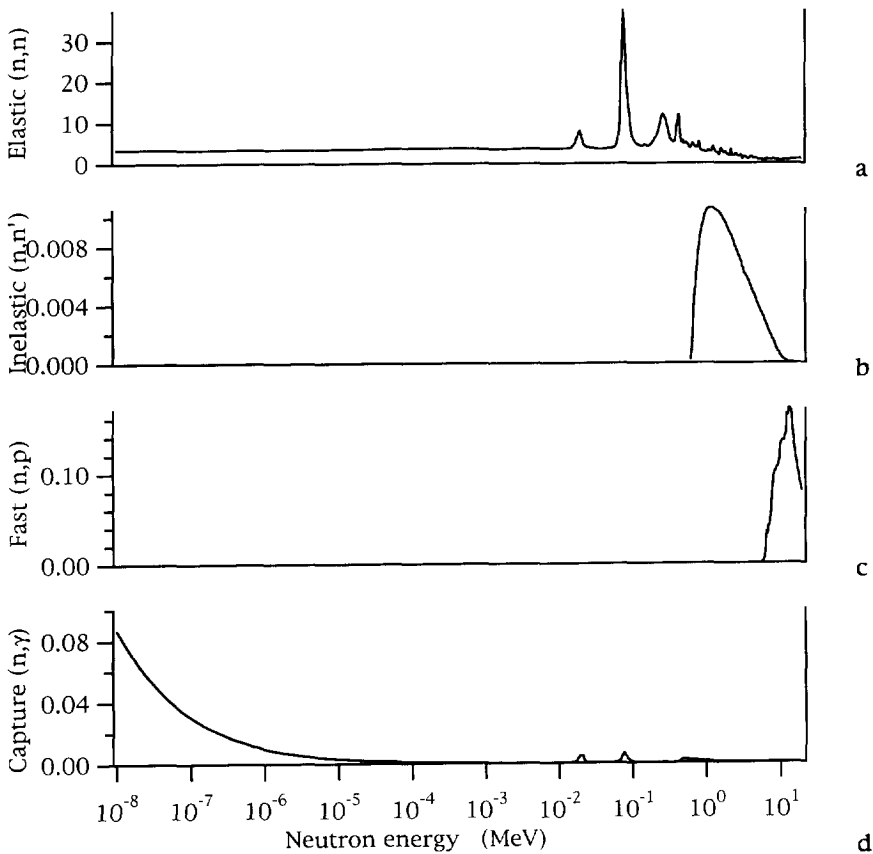


Figure 2-3 (a-d) Four neutron cross sections for magnesium. Vertical axes are in barns. Plot (b) is for interactions leading to the first excited state of the nucleus. Other excited states are possible. [34]

where Θ is the scattering angle. This function is plotted in Figure 2-4 for several common elements in the earth, plus a few light elements. It is apparent that hydrogen has, by far, the greatest neutron moderating power when considering elastic scattering. All kinetic energy may be lost when scattering from hydrogen. For this reason, neutrons have been used to measure the hydrogen content of earth formations for fifty years. It is apparent from the possible ranges of fractional energy loss that higher concentrations of the lighter elements, in particular hydrogen, will result in moderation to thermal energies in fewer scattering events.

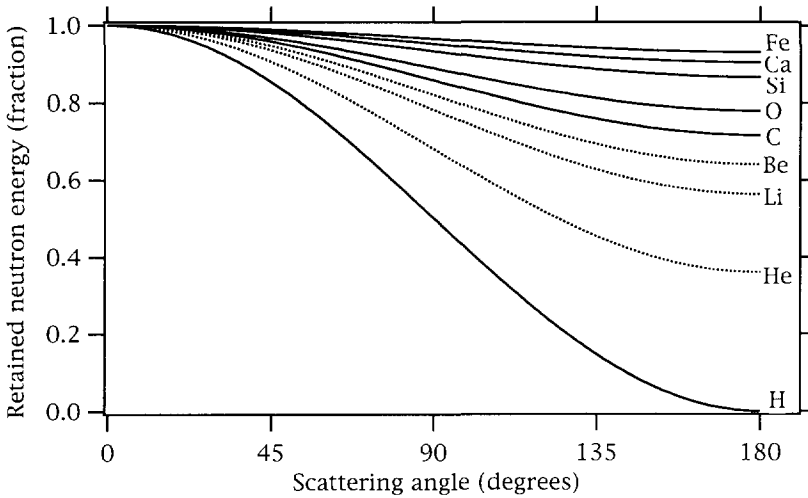


Figure 2-4 The fractional energy retained by a neutron after elastic scattering depends on the scattering angle and the mass of the target nucleus.

Further kinematic consideration of the distribution of scattering angles will lead to an expression for the average fractional energy retained after scattering from large nuclei.

$$\ln(\bar{f}) = \frac{-2}{A + 2/3} \quad 2-7$$

Then, the average number of scatters \bar{n} to slow down neutrons to a lower energy may be calculated. Table 2-1 contains calculated values of the average retained energy fraction and average number of collisions for slowing down neutrons from 14 MeV to 0.5 eV for common elements and two limestones with different porosities.

Material	(\bar{f})	\bar{n}
H	0.37	17
C	0.85	109
O	0.89	143
Si	0.93	247
Ca	0.95	349
Fe	0.97	481
Water	0.40	19
20 pu limestone, water filled	0.60	33
0 pu limestone	0.89	149

Table 2-1 Average fractional energy retained after scattering and average number of collisions to slow down a neutron from 14 MeV to 0.5 eV.

The discussion of the number of scattering events for neutron slowing down was presented because it is useful to demonstrate a point about the spatial distribution of neutrons at any given energy. Consider a homogeneous medium with an isotropic point source of high energy neutrons. Because of the random nature of scattering, a medium requiring more collisions for slowing down will have its low energy neutrons distributed more widely. This is the basis for borehole measurement of porosity, since it can be seen from the limestone and water values in Table 2-1 that a more porous rock (with water in the pore space) will require fewer scattering events for slowing down, thus the moderated neutrons will generally be closer to the source point.

A parameter called the slowing down length L_s has been defined to be the root-mean-square displacement required for thermalization of a source neutron. It depends primarily on the hydrogen content of the medium, and to a lesser extent on the density. It can be shown that the flux of neutrons ϕ at a distance r from a source, relative to the flux ϕ_0 that would be seen if there was no intervening scattering medium, is described by equation 2-8.

$$\phi = \phi_0 e^{-r/L_s} \quad 2-8$$

2.2.2 Inelastic scattering

When incident neutron energy is greater than some threshold, which is specific to the target nuclide, reflecting the energy of the first excited state, kinetic energy may be lost by the neutron to an excitation of the target nucleus [28]. Several excited states are typically possible. This phenomenon is known as inelastic scattering, and results in a greater energy loss by the neutron than a similar elastic scattering event. The recoiling nucleus de-excites rapidly, usually producing a gamma ray. Detection of these gamma rays forms a basis for carbon-oxygen logging and other forms of elemental analysis, since the gamma ray energy is *characteristic* of the nuclide. Figure 2-3(b) contains a plot of the inelastic cross section for the first excited state of magnesium. The neutron energy threshold for this cross section is about 700 keV.

2.2.3 Radiative capture

There is a likelihood that a neutron will be captured as it approaches a nucleus, forming a compound nucleus, particularly when it has slowed down to thermal energies [31]. Several nuclides, such as boron, chlorine, gadolinium, and samarium demonstrate a great affinity for absorption of thermal neutrons. A typical cross section plot for neutron capture is presented in Figure 2-3(d). There is only a small likelihood of capture at most energies, but at energies

below a few eV, the cross section increases, exhibiting a shape proportional to $1/\sqrt{E}$. Also, there are a few small peaks in the cross section, known as the resonance region, in the vicinity of 100 keV.

The resulting excited compound nucleus de-excites quickly to its ground state, with the emission of one or more characteristic gamma rays. Additionally, the ground state of the compound nucleus may decay later with a half-life and gamma-ray emission characteristic of the *activated intermediate nucleus*. These two types of gamma ray emission form the bases for two types of spectroscopic measurements. Detection of promptly emitted capture gamma rays can be used to identify the presence and concentration of some elemental concentrations in earth media. The same can be accomplished using the delayed activity gamma rays. More commonly, a reactor is used as a source of thermal neutrons to activate a small sample for subsequent counting of the characteristic gamma rays. Mass concentrations of fifty or so elements can be measured in this fashion.

2.2.4 Particle production during absorption

When the neutron energy is greater than the required threshold for a specific nuclide, an α -particle, proton, or one or more additional neutrons may be produced by some target nuclides during or following absorption of the fast incident neutron [31]. A cross section for a reaction of this sort with a threshold of about 2 MeV is displayed in Figure 2-3(c). The transformed nucleus may be stable, or may decay with a half-life and gamma-ray emission characteristic of the intermediate state.

2.3 Gamma ray interactions

Similarly to neutrons, gamma rays react with matter by scattering and absorption. The interactions are with the electron field or the atom as a whole, resulting in transfer of photon energy to electron energy. Three important mechanisms for absorption and scattering, among the many that are possible, predominate the transport and attenuation of gamma rays in earth media [32]. Prevalence of the three reactions is predominantly dependent on gamma ray energy and the atomic numbers Z of the medium.

A convenient mathematical construction for gamma ray transport problems is the *linear attenuation coefficient* μ , defined to be the probability per unit path length that any scattering or absorption event will occur, and usually stated in cm^{-1} . The linear attenuation coefficient is analogous to the macroscopic cross section defined for neutrons in section 2.2 above. For a

gamma-ray intensity I_0 that would be observed at a distance r without an absorber, the unscattered intensity I at r will be as follows.

$$I = I_0 e^{-\mu r} \quad 2-9$$

A more convenient construction when dealing with mixtures of materials is the mass attenuation coefficient ξ , defined as the linear attenuation coefficient divided by the density, and thus having dimensions area per mass.

$$\xi = \frac{\mu}{\rho} \quad 2-10$$

For a specific gamma-ray energy, ξ is a weakly varying property of the atomic species only, thus for a mixture of elements, a summation weighted by the fractional mass w_i of each element will provide the mass attenuation coefficient of the mixture.

$$\xi_{mix} = \sum_i w_i \xi_i \quad 2-11$$

Furthermore, ξ is about the same for most earth materials, varying only to the extent that A/Z deviates from 2. Substitution of the mass attenuation coefficient into the previous expression for the unscattered gamma ray intensity gives the following expression.

$$I = I_0 e^{-\xi \rho r} \quad 2-12$$

2.3.1 Compton scattering

When considering earth materials and the energies of gamma rays generated by neutron activation, Compton scattering is the most important interaction governing the transmission of gamma rays, and is dominant for energies from 100 keV up to several MeV. The reaction rate for this mechanism, direct scattering from electrons, is essentially proportional to the number density of electrons in the scattering medium.

The incident gamma ray with energy E_γ imparts some of its energy to the electron, which initially can be considered to be at rest. The gamma ray is deflected by an angle θ of from 0 to 180 degrees. The amount of kinetic energy E_{e^-} assumed by the recoiling electron is

$$E_{e^-} = E_{\gamma} \left(\frac{(E_{\gamma}/m_0c^2)(1-\cos\theta)}{1+(E_{\gamma}/m_0c^2)(1-\cos\theta)} \right) \quad 2-13$$

which will approach zero in the limit as the scattering angle becomes very slight, and will reach a maximum, short of full energy transference, for direct backscattering. In this expression, the rest mass of the electron m_0 times the square of the speed of light c is equal to 511 keV. The fractional quantity of energy imparted to the electron

$$E_{e^-}/E_{\gamma} \quad 2-14$$

is plotted against scattering angle in figure 2-5 for several gamma-ray energies across the range of interest.

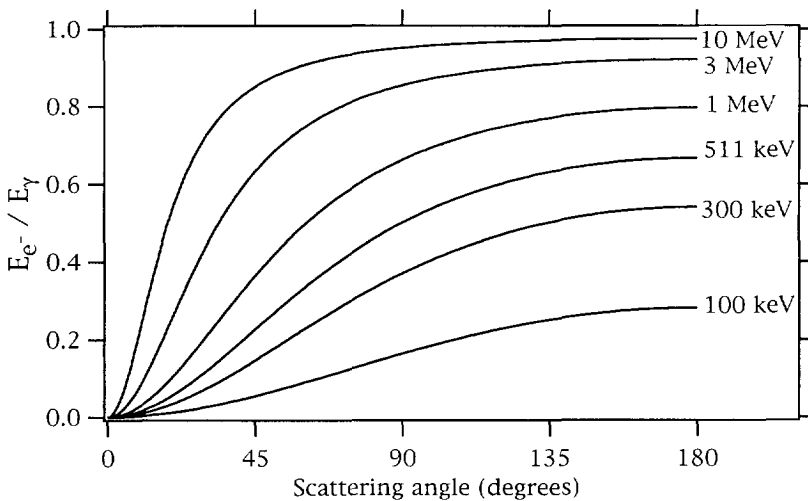


Figure 2-5 The fraction of incident gamma-ray energy imparted to an electron in Compton scattering depends on the scattering angle.

2.3.2 Photoelectric absorption

As Compton scattering results in lower and lower energy photons, a photoelectric absorption reaction becomes more likely, and is the dominant reaction below about 80-100 keV. Low energy gamma rays may be completely absorbed by an atom which ejects a bound electron, often from the K shell. The electron emerges with a kinetic energy equal to the incident photon energy minus the electron binding, or orbital, energy. If the incident photon has an energy less than the binding energy of a K shell electron, then an electron

from a less tightly bound shell may be ejected. K-shell orbital binding energies range from about 1 keV for light elements to several tens of keV for the heavier elements. Probability P for the reaction increases quickly with atomic number Z and falls off strongly with increasing gamma ray energy, and has been approximated [28] by variants (in the exponents) of the general form below.

$$P \sim \frac{Z^{(4.5)}}{E_{\gamma}^{(3.5)}} \quad 2-15$$

The deficiency created in the electronic structure is quickly compensated by electrons in the other atomic shells or in the region of the newly formed ion, which may result in the emission of characteristic X-rays.

2.3.3 Pair production

At gamma-ray energies above $2m_0c^2$ (1.022 MeV), the complete absorption of a gamma ray and production of a positron-electron pair becomes possible within the Coulomb field of a nucleus. The cross section for the pair production reaction is small at this energy, but increases strongly with energy. The relative strength of the reaction on total gamma-ray transport in earth materials only becomes important when considering gamma rays of several MeV. Pair production cross sections exhibit a strong dependence on the atomic number, or charge of the nucleus, increasing approximately as Z^2 .

At the onset of pair production, all the photon energy in excess of $2m_0c^2$ is split between the electron and positron as kinetic energy. The positron is quickly annihilated by an electron after almost certainly traveling less than a centimeter, resulting in the creation of a pair of gamma rays of energy m_0c^2 (511 keV).

2.4 Gamma-ray detection and spectroscopy

There are two main types of detectors that are suitable for resolving gamma-ray energy: scintillators and semiconductor detectors. Each must perform two functions to be a viable spectrometer. First, it must utilize one or more of the three types of gamma-ray interactions described in the preceding sections to transfer the photon energy to electrons in a proportional manner. Second, it must detect the electrons, preserving some degree of the energy proportionality in conversion of the gamma-ray to an electrical pulse [28].

The first function of the spectrometer would be performed ideally by converting the energy of each incident photon entirely into electron energy contained within the detector. The two ways to approach this unachievable

goal, for both scintillators and semiconductors, are to make the detector as big and as dense as possible. Recall that the likelihood of photoelectric, Compton, and pair production interactions increased as $Z^{(4-5)}$, Z , and Z^2 respectively. Obviously, high- Z materials will make a difference. Size also helps by giving the incident photon, secondary electrons, and secondary photons more material to interact in without leaving the detector. Differences between semiconductors and scintillators are in the mechanisms for performance of the second function. These mechanisms have large effects on the attainable resolution of gamma-ray energy.

2.4.1 Scintillators

There are two main types of scintillators, classified by their general form and mechanism. The organic materials rely on single molecular energy transitions to generate fluorescence and are generally amorphous liquids or plastics, except for a few pure organic crystals. These materials, composed of low- Z elements, have a density of around 1 gram per cubic centimeter and thus, poor efficiency for detection of MeV gamma radiation. They will not be discussed further in this report.

Sodium iodide doped with thallium became available in the 1950's and, together with the development of the photomultiplier tube for conversion of the weak light pulse to a reasonable electrical signal, made gamma ray spectroscopy applicable to many fields. Today sodium iodide is by far the most popular gamma-ray detector material and serves as the standard against which prospective new detector materials are compared. It is an inorganic scintillator, with a regular crystalline lattice and about 0.001 mole fraction thallium dopant, which serves as an *activator*. Many other scintillating materials have been developed which have favorable properties for use in certain applications.

2.4.1.1 Scintillation mechanism

Sodium iodide and other insulators (and semiconducting materials) possess only discrete bands of permissible electron energies, called the valence band for electrons bound at lattice sites and the higher energy conduction band for free electrons. The difference between the two energy bands is the band gap. Energetic charged particles moving through the crystal will cause a proportional number of electron-hole pairs to form as electrons acquire energies of non-bonding orbitals of the conduction band. In a pure sodium iodide crystal, the band gap is typically large enough that the subsequent de-excitation of the electron to the valence band would result in an emission of a

photon more energetic than those of the visible region in which photomultipliers function.

The activator, thallium, distributed throughout the crystal lattice, serves to locally modify the energy bands, providing an efficient pathway for de-excitation of the electrons. Holes are drawn rapidly to the impurity site in the lattice and ionize the activator. A free electron subsequently falls into the site, creating an excited energy state of the impurity atom which can de-excite with an emission of light in the visible region. The choice of an activator must meet three broad criteria to make the scintillation process an efficient one. First, the activator must be of the proper size that its substitution will not cause disruptions in the crystal structure. Second, it must act as a hole trap, providing a preferential attraction to the positively charged holes. And third, it must possess excited states with permissible transitions to the ground state that are in the visible light region, or in the near ultraviolet or infrared regions.

2.4.1.2 Light collection and photomultipliers

Ideally, all the light from the scintillation event would be collected by the photomultiplier tube. In practice, this is not the case because of a number of mechanisms. The light may be absorbed by the crystal, though most commercially available crystals have a very low degree of opacity unless there has been some damage such as clouding or fracturing. A more severe problem is caused by imperfect reflection at the crystal surfaces. Because the light is emitted from activator sites in all possible directions, it may have to undergo several reflections before leaving the crystal through the face coupled to the photomultiplier. Imperfect reflection is a certainty, typically minimized by proper surface preparation, including a slightly roughened surface and the use of a diffuse reflector such as packed MgO powder at the crystal faces. No internal reflection, another unachievable goal, is desired at the interface between crystal and photomultiplier. Matching of refractive indices is the strategy used in maximization of the transmission through the crystal-coupling-photomultiplier interfaces.

The photomultiplier tube essentially performs two functions. First the incident visible light photons are converted to electrons near the coupled surface of the tube in the *photocathode*. The electrons migrate to the inner surface of the photocathode and escape with a kinetic energy of about 1 eV. This photoemission process typically has an efficiency dependent on the wavelength of the light, which peaks at about 25%. Second, the electrons are accelerated by approximately 100 volts through a series of about ten electron multiplication

stages, each with a gain of about 4-5, resulting in an overall gain in the tube on the order of 10^6 or 10^7 .

2.4.1.3 Energy resolution of scintillator systems

The observed pulse height spectrum will be degraded, or broadened, due to the finite energy resolution of a detector system, defined as

$$R = \frac{FWHM}{U} \quad 2-16$$

where U is the average pulse height measured for the gamma ray full energy and $FWHM$ is the full width of the peak at half its maximum value, as pictured in Figure 2-6. A Gaussian shape of the peak is assumed or imposed by a fitting routine. The $FWHM$ is also equivalent to 2.35 times the standard deviation of a Gaussian peak. For scintillator systems, the resolution is often measured using the 662 keV gamma ray from the decay of ^{137}Cs . A good sodium iodide system is capable of about 6% energy resolution for these gamma rays. Peak resolution is normally monitored throughout the use of a spectroscopy system to verify proper operation.

A major factor controlling the energy resolution is the light output of the scintillator. Sodium iodide has an efficiency of about 11% in conversion of electron energy to photons, each with an energy of about 3 eV, meaning that for a 662 keV gamma ray that is fully absorbed, about 25000 visible-range photons will result. The statistics of this number of events corresponds to a cesium peak resolution broadening representing the intrinsic resolution of an ideal NaI(Tl) crystal.

$$R = 2.35 * Std. Dev. = 2.35 / \sqrt{25000} = 0.015 = 1.5\% \quad 2-17$$

A real crystal, particularly a sizable one, will not be homogeneous, and the resulting variation in the light output will cause approximately 2% broadening of the lines in sodium iodide. More degradation is caused in two ways by failure to achieve total internal reflection at the crystal surfaces. First, the total number of photons reaching the photomultiplier will be diminished, and second, scintillation events in regions of the detector remote from the photomultiplier will likely require more reflections than close-up events before reaching the photomultiplier, making the light output vary with position throughout the detector. Additional degradation can be caused by cloudiness in the crystal.

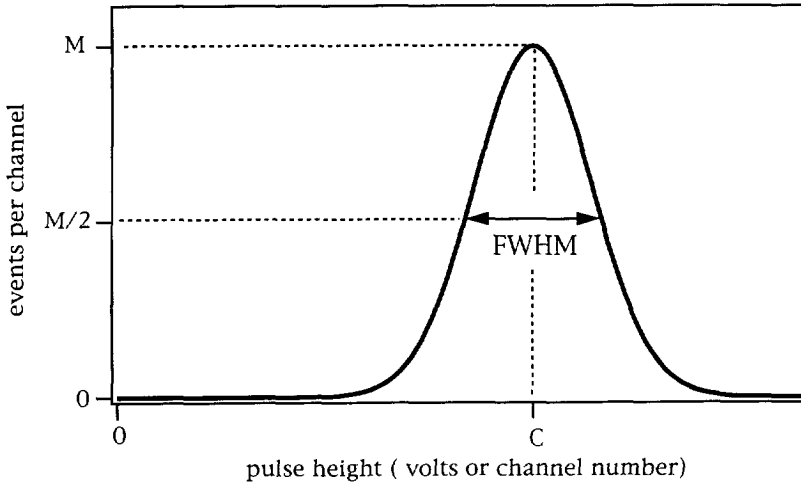


Figure 2-6 Idealized representation of a Gaussian pulse height distribution illustrates the parameters used for expressing the energy resolution. If the peak shape is governed solely by counting statistics, it will have a Gaussian shape.

Suppose we have a small crystal that it is indeed homogeneous, and that we have achieved uniform reflection at the surfaces, albeit with 20% losses, and that losses due to trapping of light by internal reflection at the interface of the photomultiplier amount to another 10%. Then the number of photons presented to the photocathode from a 662 keV gamma ray would be about 18000, and since quantum efficiency of the photocathode is approximately 20%, 3600 electrons would be produced at the photocathode inner face for acceleration to the first multiplication dynode. In this example, 3600 is the minimum number of events N that occur in the process of assessing the energy of our 662 keV gamma ray, corresponding to an energy broadening of 3.9%. Because the response of this example system is nearly linear with photon energy, resolution will be inversely proportional to the incident gamma ray energy.

$$N \propto E \quad \& \quad R \propto \frac{1}{\sqrt{N}} \quad \Rightarrow \quad R \propto \frac{1}{\sqrt{E}}$$

2-18

The degradations ignored in our example calculation of energy resolution, that is, crystal inhomogeneity and surface reflection inhomogeneity, will slightly lower the number of photoemissive electrons, but

will broaden the peaks by a greater factor than the square root of events alone would indicate, causing a deviation of the resolution from its proportionality to the inverse square root of photon energy. Additional degradation may be caused by temperature effects, which reduce the light output for a given gamma-ray energy, but these generally occur slowly enough that an instrumental gain adjustment system can fully compensate for them. High count rates, such as those encountered when operating in conjunction with a pulsed source, can cause a perturbation in the gain of the photomultiplier tube. Special power supply circuitry applied to the multiplication electrodes of the photomultiplier can minimize this problem.

2.4.2 Semiconductor spectrometers

The discussion of scintillators showed that limitations in energy resolution are attributable to statistical fluctuations in the small number of electrons attainable from the photocathode in a photomultiplier tube. Semiconductor detectors do not suffer from this problem, because the intermediate steps of converting the electron energy to light and back again to electrons are not required, and thus they can provide excellent energy resolution [28]. Germanium and silicon are the two main types of semiconductors used as radiation detectors. Silicon has low Z and a large band gap, so it is generally only useful for detecting x-rays. Further discussion will be confined to germanium detectors.

Lithium-drifted germanium detectors, or Ge(Li), have been in use since the 1960's. These detectors have undergone an ion drift process with lithium, a donor, implanted in the crystal to compensate for the predominance of acceptor impurities. The drifting process is able to achieve a level of uncompensated impurities of only about 10^9 per cm^3 . Mobility of the lithium ions is high at room temperature, so to maintain the proper lithium distribution, Ge(Li) detectors must be kept at liquid nitrogen temperatures at all times.

In the 1980's high purity germanium, or HPGe, became widely available, with levels of impurity only 10^9 to 10^{10} atoms per cm^3 , about 1 part per 10^{13} . Attaining such purity is a painstaking process, and the material remains expensive. A locally molten region is repeatedly moved through the stock, taking advantage of the solubility affinity that impurities will have for the melt. Crystals are then grown from the purified germanium. Remaining contamination, depending on whether it is dominantly a donor or an acceptor, will cause a slight n - or p -type behavior. The distinct advantage of HPGe is that the detector does not need to be maintained at liquid nitrogen temperatures, except when being used.

Because a bias voltage must be applied across the crystal, "blocking" contacts are used to prevent leakage current, which would provide a source of noise larger than the desired signal. The blocking contact consists of a p-n junction that is reverse-biased, preventing the flow of current in one direction, and configured so that the desired signal will flow across the junction. Ion implantation is used on one face of the crystal to provide the junction. A very favorable aspect of the p-n junction is that, if the detector has a low enough impurity level and a sufficient bias is applied, the entire crystal becomes a zone of electron-hole depletion. Charge carriers created by radiation interactions in the detector are rapidly collected with minimum trapping loss. Additional applied voltage will hasten the drift velocity with which electrons and holes are swept from the detector, up to a saturation velocity.

Leakage currents are the main sources of noise in depleted detectors, and come from either bulk leakage or surface leakage, which are dependent on material purity and manufacturing processes. The small bandgap in germanium crystals, about 0.7 eV, requires that the temperature be reduced to nominal liquid nitrogen temperature to further reduce the thermally induced leakage current. The crystals are housed in vacuum-tight cryostats (see Figure 2-7 for an example) which are equipped with an insulated liquid nitrogen reservoir. The input stage of a signal preamplifier is also chilled in the cryostat to reduce noise and to keep it close to the detector.

Coaxial detector geometry, pictured in the figure, is commonly used when large detector volumes are required. The outer surface of the crystal, including the bottom, is one electrode, and the inner cylinder is used as the other electrode. The rounded shape of the bottom, called *bulletized*, and the depth of the inner cylinder are designed to optimize the shape of the electric field in the crystal and thus maximize charge collection.

Resolution of a germanium detector system is the quadrature sum of three resolution factors. The inherent statistics of the charge carriers makes up one factor. For a semiconductor, the number of electron-hole pairs is not strictly a Poisson process for reasons that are not totally understood. Apparently, ionization events are not independent, resulting in better statistics than would be predicted using only the total gamma-ray energy divided by the ionization energy H equal to 3 eV. An additional quantity called the Fano factor F has been introduced to compensate for the deviation from Poisson statistics. The fractional peak broadening due to charge carrier statistics R_D then is described in Equation 2-19.

$$R_D = 2.35 * \sqrt{F} * Std. Dev = 2.35 * \sqrt{F \frac{H}{E}} \quad 2-19$$

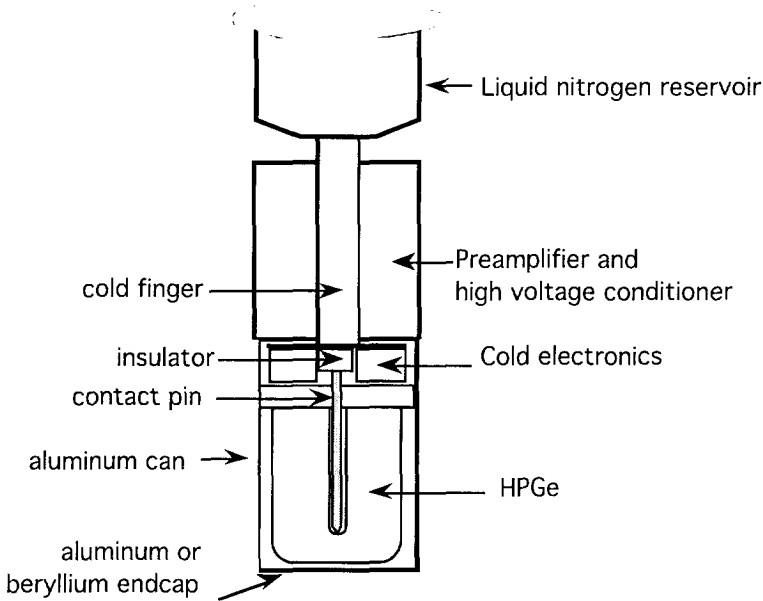


Figure 2-7 The main features of a Dewar and cryostat containing a closed-ended, bulletized coaxial germanium detector.

Fano factors are often observed to be about 0.2. For the 662 keV gamma ray from cesium, electron-hole statistics will be about

$$R_D = 2.35 * \sqrt{0.2 * \frac{3}{662,000}} = 0.002 = 0.2\% \quad 2-20$$

where an ionization energy of 3 eV is used in the calculation.

The second source of peak broadening is due to incomplete collection of the charge R_X , particularly in large detectors where there may be some irregularities in the electric field, and where the larger distances that carriers must travel makes them more likely to be trapped. Losses are nearly proportional to the energy deposited in the detector. This is usually the largest source of degradation in the pulse height spectrum.

The third mechanism for resolution degradation is the effect of electronics and cables for processing of the signal R_E , which often amounts to a steady value of about 1 keV across the entire energy spectrum. Thus the noise is more significant at lower gamma ray energies. Total resolution is the vector sum of the three parts.

$$R_{TOTAL} = \sqrt{R_D^2 + R_X^2 + R_E^2} \quad 2-21$$

An additional effect of the three separate factors is that resolution does not scale with the square root of energy as it often does for scintillators. Resolutions of larger germanium detectors used for gamma-ray spectroscopy are usually stated in keV FWHM of the 1.333 MeV gamma-ray line from the decay of ^{60}Co . A typical good value for a large volume detector is 2.0 keV.

2.5 Energy deposition in spectrometers

The three types of gamma-ray scattering and absorption interactions described above lead to energy deposition in a detector. Ideally, all energy from an incident gamma ray would be deposited in the detector, but this is only occasionally the case. Photoelectric absorption comes the closest to this ideal, since the liberated electrons do not typically escape from the detector. A monoenergetic flux of low energy gamma rays, with energy perhaps in the tens of keV, will result in an energy deposition distribution from photoelectric absorption resembling Figure 2-8.

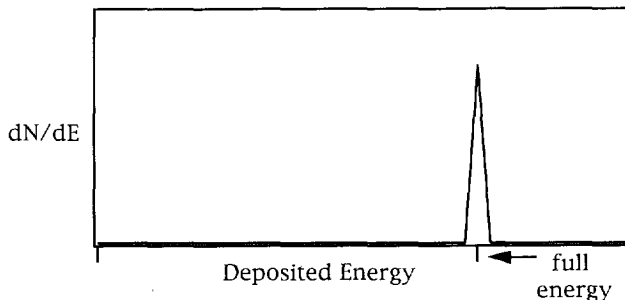


Figure 2-8 Deposited energy from photoelectric absorption assuming no photoelectrons leave the detector

Compton scattering will result in a distribution of energy imparted to an electron, which depends on the scattering angle (see Equation 2-13). It can be verified that some of the energy is retained by the scattered gamma ray even in the case of direct backscattering ($\theta = 180$ deg), and that, as gamma ray energies become very large, the value of the retained energy approaches half the rest mass of an electron, or 0.256 MeV. The maximum recoil electron energy is the most energy that can be imparted to the detector from a single Compton scattering event, and defines the "Compton edge" as shown in Figure 2-9.

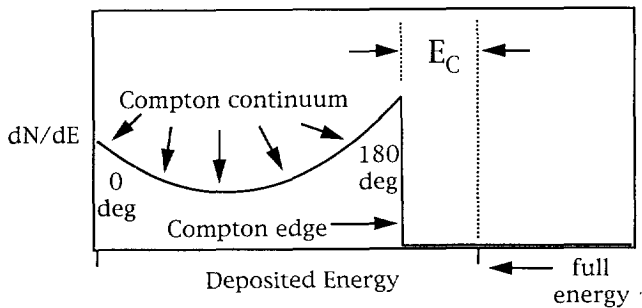


Figure 2-9 Energy deposited in a detector from a series of single Compton scattering events. The series spans all the possible scattering angles.

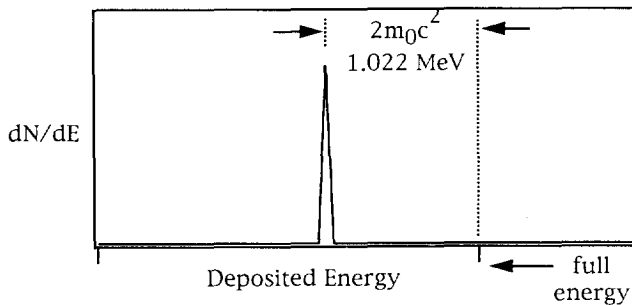


Figure 2-10 Energy deposited in a detector from pair production events. To detect the full energy, the pair of subsequent annihilation gamma rays must be fully absorbed by the detector.

The difference between the incident gamma ray energy and the maximum recoil energy of the electron is found by rearranging Equation. 2-13, using a value of 180 degrees for the scattering angle.

$$E_C = E_\gamma - E_{e^-} @ \theta=180 = \frac{E_\gamma}{1 + 2E_\gamma/m_0c^2} \quad 2-22$$

Pair production imparts incident gamma-ray energy in excess of $2m_0c^2 = 1.022\text{MeV}$ to electron and positron kinetic energy, which is quickly absorbed by the detector as these particles slow down, resulting in energy deposition as shown in Figure 2-10. The subsequent pair of annihilation gamma rays, which are produced when the positron annihilates with an electron, will be subjected to additional scattering and absorption.

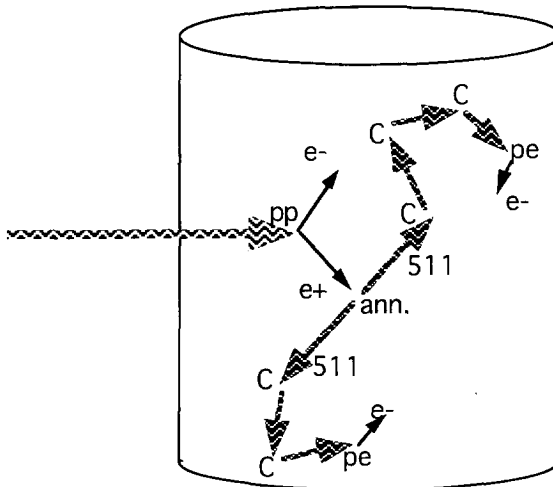


Figure 2-11 One possible scenario for complete absorption of a high energy gamma ray. pp - pair production. C - Compton scattering. pe - photoelectric absorption. ann - annihilation.

Because only photoelectric interactions result in the complete absorption of gamma-ray energy by the detector, it is obvious that multiple events such as those depicted in Figures 2-8, 2-9, and 2-10 must occur in the detector if there are to be any full energy peaks in the pulse height spectrum for high energy gamma rays. One of many possible scenarios is depicted in Figure 2-11 for full energy absorption of an incident high energy gamma ray, which causes

production of a positron electron pair. The kinetic energy of the pair is quickly absorbed, and the positron is annihilated. The resulting pair of 511 keV gamma rays undergo multiple Compton scattering, and finally are absorbed. If one or both of the annihilation gamma rays are the *only* radiation to "escape" the detector, then the event will appear in the single or double escape peak of the pulse height spectrum. Escape of other secondary gamma rays (or electrons) will cause the event to be recorded in the continuum underlying the peaks. It is clear from these considerations that making a detector larger will enable it to contain more secondary photons and thus detect the full energy of incident gamma rays with a higher efficiency. Figure 2-12 is an example of a pulse height spectrum obtained with a large (400 cm^3) germanium detector. The detector has diameter 7.6 cm and length 8.8 cm. Several of the prominent features in the spectrum have been labeled.

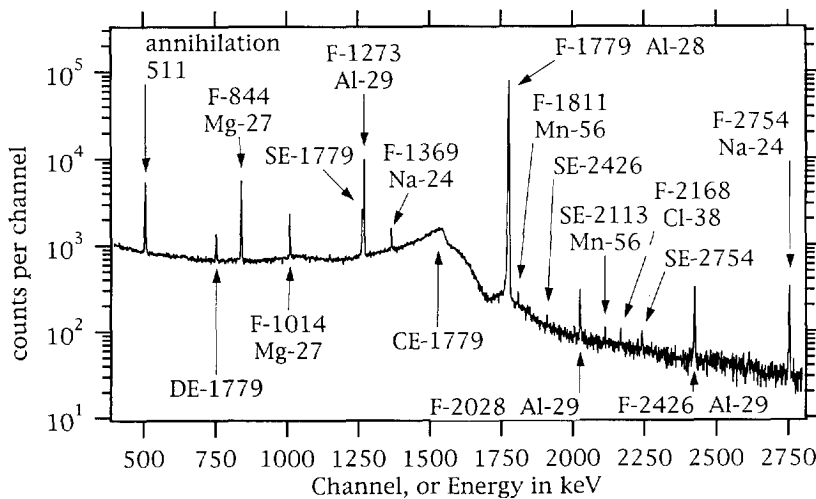


Figure 2-12 Example of a pulse height spectrum from a large (400 cm^3) germanium detector. Prominent features are labeled. F - full energy peak. SE - single escape peak. DE - double escape peak. CE - Compton edge. Numbers are full peak energies in keV.

The largest peak in the spectrum is the full energy peak at 1779 keV. The Compton edge and single and double escape peaks corresponding to this full energy peak are visible in the spectrum. The Compton edge does not display the sharp drop as depicted in Figure 2-9, the main reason being that energy from subsequent Compton scatters of the same event have been added.

Though the single escape peak at 1268 keV is directly adjacent to a full energy peak from a different decay, at 1273 keV, an expansion of the data in Figure 2-13 reveals that the two peaks are separable. Usually, a fitting routine is used to impose near-Gaussian shapes to the peaks, resulting in an estimate for areas of both peaks. Notice that the double escape peak for the 2754 keV gamma ray in Figure 2-12 is not visible. It's position would be just to the left of the 1779 keV peak, where the continuum has risen sharply and has covered up any double escape events.

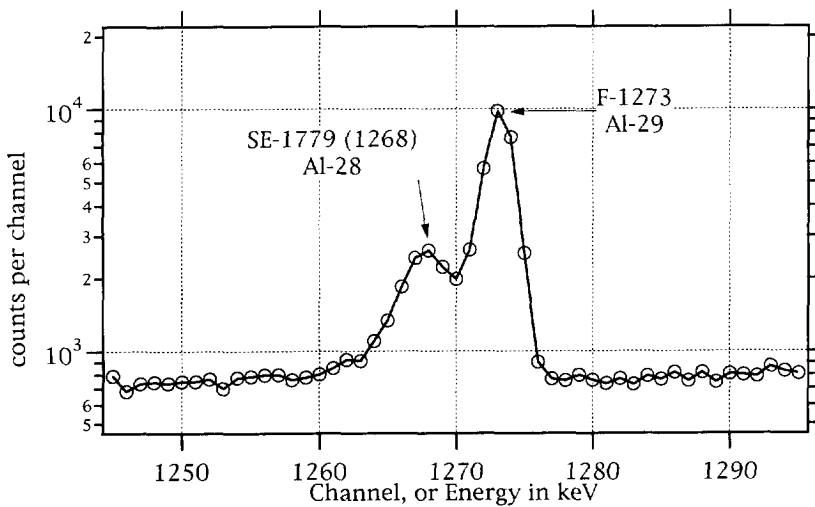


Figure 2-13. An expansion of the previous figure reveals an additional utility of good detector energy resolution by partial separation of the two peaks.

There are several quantities used as measures of detector ability to collect the full energy of an incident gamma ray. The *peak-to-Compton* ratio is defined as the ratio of counts in the highest peak channel to the counts in a representative channel in the flat part of the Compton continuum. This region is at 370 keV for 662 keV gamma rays from the decay of ^{137}Cs , and at 1070 keV for 1333 keV gamma rays from the decay of ^{60}Co . Another closely related quantity is the *photofraction*, defined as the fraction of counts from interacting incident gamma rays that appear in the full energy peak. Escape peaks are a prominent feature of many pulse height spectra, particularly for small detectors, where the escape peaks may contain more counts than the full energy peak. The ratio of an escape peak area to the full energy area is also used as a measure of detector performance.

Efficiency of germanium detectors \mathcal{E} or \mathcal{E}_{3X3} is often quoted relative to the efficiency of a 3 inch diameter by 3 inch length sodium iodide crystal, for the full-energy detection of 1333 keV gamma rays from the decay of ^{60}Co . High purity germanium detectors with values of $\mathcal{E}_{3X3} = 100\%$ have been available since about 1990.

2.6 Neutron activation analysis fundamentals

The elements of radiation interactions, neutron sources, and gamma ray detection pertaining to borehole neutron activation analysis (NAA) have been discussed in the preceding sections. This section will describe the neutron activation analysis NAA in more detail. Activation, transfer, and counting form the three main parts of a neutron activation measurement, aside from sample preparation and data reduction.

For equations relating to activation analysis, it is more convenient to use the natural time constant for decay τ , rather than the half-life $t_{1/2}$. The two are related by the expression below.

$$\tau = \frac{t_{1/2}}{\ln(2)} \quad 2-23$$

As mentioned in sections 2.2.3 and 2.2.4 above, neutron interactions may cause the formation of activated nuclei, which will subsequently decay with a characteristic half-life. Half-lives may vary from fractions of a second to many years, but the useful range of half-lives for neutron activation analysis, unless unusual measures are taken, is in the range from several seconds to a few days. Decay products are normally beta particles, often accompanied by gamma rays, whose energies are characteristic of the decaying nuclide. Often, not all decays will result in the same particle emission. The percent of decays that will result in a particular emission is termed the branching ratio b . Subsequent analysis of the gamma radiation with respect to energy and time can be quantitatively diagnostic of the intermediate nuclide, and thus, the original element.

2.6.1 Activation buildup and decay

When a small amount of sensitive material is exposed to a constant neutron flux of a single or narrow range of energy, the reaction rate Y and cross section σ are related by Equation 2-24.

$$Y = N\phi\sigma \quad 2-24$$

The assumptions are made that there are so few N atoms of material which are so spread out that no perturbation of the neutron flux ϕ occurs, that no appreciable amount of material is used up, and that no pre-existing activity was present in the material. At any instant, the rate of change of the number of activated nuclei η is given as.

$$\frac{d\eta}{dt} = Y - \frac{\eta}{\tau} \quad 2-25$$

where η/τ represents the rate of decay D . For the conditions stated above, integration yields the number of activated nuclei as a function of time.

$$\eta = Y\tau(1 - e^{-t/\tau}) \quad 2-26$$

It is convenient to rearrange this expression in terms of the decay rate D .

$$D = \frac{\eta}{\tau} = Y(1 - e^{-t/\tau}) \quad 2-27$$

Notice that for long times, D asymptotically approaches a saturation activity D_∞ , equal to Y . Conventionally, t_0 is the duration of irradiation.

$$D_0 = D_\infty(1 - e^{-t_0/\tau}) \quad 2-28$$

At t_0 the sample is removed from the neutron field and transferred to a position near a gamma ray detector. At any time t after t_0 , the activity will be described by Equation 2-29.

$$D = D_0 e^{(t_0-t)/\tau} \quad 2-29$$

If the detector records decay gamma rays between times t_1 and t_2 , and the sample is small enough that there is no internal absorption or scattering, then the observed number of counts C will be the integral of the above expression times absolute efficiency ϵ and the branching ratio b .

$$C = b\epsilon\tau D_0 \left(e^{(t_0-t_1)/\tau} - e^{(t_0-t_2)/\tau} \right) \quad 2-30$$

Counts can be related to the saturated activity by substitution of Equation 2-28 into 2-30, yielding the following expression.

$$C = b\epsilon\tau D_\infty (1 - e^{-t_0/\tau}) \left(e^{(t_0-t_1)/\tau} - e^{(t_0-t_2)/\tau} \right) \quad 2-31$$

2.6.2 Neutron activation cross sections in a mixed-energy flux

For a well-thermalized neutron flux, such as found at reactor sites where *thermal* neutron activation analysis TNA is performed, or for any approximately monoenergetic flux of neutrons, the reaction rate Y and cross section σ in a thin sample are adequately described by Equation 2-24.

When a mixed-energy flux of neutrons is used, the response Equation 2-24 must be integrated over the energy domain, since both the flux and cross sections will exhibit energy dependence. The reaction rate for a thin target in a mixed flux is given by the integral of the cross section times flux over energy E , and is called the response integral.

$$Y = N \int_E \phi(E) \sigma(E) dE \quad 2-32$$

Knowledge of thermal neutron cross sections is essentially complete for all the elements, but this is not the case for the cross sections that apply to mixed-flux activation. While the database of fast neutron particle production cross sections is immense, it has not approached the precision of thermal neutron data in most cases. Large uncertainties exist in cross sections for many threshold reactions, often tens or even up to fifty percent for some nuclides. Often, the energy of the neutron flux used to measure cross sections has an uncertainty of 400 keV.

2.6.3 Competing reactions in a mixed flux

When NAA is performed at a reactor site, the energy distribution of the neutron flux in the irradiation area is well known. Furthermore, the flux is typically nearly all thermalized, with perhaps one epithermal neutron in several hundred thermal neutrons [22]. The use of a well-thermalized source makes the analysis much simpler, in one sense, because each activated state can arise from only a unique elemental isotope. For a purely thermal flux, the decay of ^{24}Na , for example, with a half-life of 15.02 hours and the emission of gamma rays at 1.3688 and 2.7541 MeV, is entirely diagnostic of the sodium content of a sample. In this case, the intermediate nuclide must have arisen from the large cross section thermal reaction $^{23}\text{Na}(n,\gamma)$.

When a mixed flux is used, it brings into consideration the n,p and n,α reactions that typically have thresholds of a few MeV, resulting in the doubtless production of identical activated nuclides from two or more original elements. For the case of the activated nucleus ^{24}Na mentioned above, we must now also consider contributions to the activation from the similarly probable MeV-energy reactions $^{24}\text{Mg}(n,p)$, and $^{27}\text{Al}(n,\alpha)$.

initial nuclide	reaction	intermediate nuclide	half-life	γ rays
²³ Na ²⁴ Mg ²⁷ Al	(n, γ) (n,p) (n, α)	²⁴ Na	15.02 h	1368.6, 2754.1
²⁶ Mg ²⁷ Al ³⁰ Si	(n, γ) (n,p) (n, α)	²⁷ Mg	9.45 m	843.8, 1014.4
²⁷ Al ²⁸ Si	(n, γ) (n,p)	²⁸ Al	2.246 m	1778.8
²³ Na ²⁶ Mg	(n,p) (n, α)	²³ Ne	37.6 s	439
²³ Na	(n, α)	²⁰ F	11.0 s	1633.1
²⁵ Mg	(n,p)	²⁵ Na	60 s	390.7, 585.9, 975.2, 1611.9
²⁹ Si	(n,p)	²⁹ Al	6.52 m	1273, 2028, 2426

Table 2-2. Seven of the intermediate nuclides from sodium, magnesium, aluminum, and silicon that result in decay gamma rays. Four of the seven nuclides have competing reactions leading to them. There are more possible reactions from Na, Mg, Al, and Si that are not suitable for further consideration because of their half-lives, cross sections, or branching ratios.

The group of common rock forming elements consisting of silicon, aluminum, sodium, and magnesium include several of these competing reactions [19], which are listed in Table 2-2. In addition to the competing reactions, the fast neutrons introduce additional reactions with unique intermediate nuclides so that there are now seven measurable activities from which the concentrations of the four elements can be deduced after considering the proper environmental corrections to each.

2.6.4 Neutron activation in a large sample

If a sample with tangible size is used, another dimension must be added to the reaction rate equation (Equation 2-32) because the distribution of neutron energies and the total neutron flux vary spatially across the sampled region V , due to scattering and volumetric dispersal. A homogeneous medium in V is assumed and N is therefore left outside the integral.

$$Y = N \int \int_V \phi(E, V) \sigma(E) dE dV$$

2-33

This expression is general enough that V is not required to encompass all space, but only a region of interest such as a sample. Recent works by several researchers have led to a better understanding of the large sample effects on neutron flux [35-37].

Sampling of the subsequent decay gamma rays by a detector will be dependent on the spatial variation in activated nuclei, scattering and absorption in the sample, and volumetric dispersal. Any one volume element in V will have an associated transmission efficiency $\Omega(V)$ for unscattered transport of the gamma rays to a detector position.

If the sample remains in a constant neutron flux from time $t = 0$ until time t_0 , then at some later time t_1 the resulting flux of unscattered gamma rays at some detector can be stated as

$$I = bN \left(1 - e^{-t_0/\tau}\right) \left(e^{(t_0-t_1)/\tau}\right) \int \int_{VE} \phi(E, V) \sigma(E) \Omega(V) dE dV \quad 2-34$$

where b is the branching ratio for the gamma-ray emission. If the two terms relating to the saturation are incorporated as a function $g(t, \tau)$, and the detector has efficiency \mathcal{E} , then the count rate observed in the detector will be as follows.

$$C. R. = g(t, \tau) \mathcal{E} b N \int \int_{VE} \phi(E, V) \sigma(E) \Omega(V) dE dV \quad 2-35$$

One approach to solution of Equation 2-35 is by simulation of neutron and gamma-ray behavior using a Monte Carlo method, where all possible scattering and absorption cross sections are used to track the progress of individual neutrons and gamma rays [34,35]. This method will be discussed in chapter 7.

For the special case of an infinite homogeneous medium with both neutron source and gamma ray detector at the origin, and a reaction cross section that is significant only in a narrow range of neutron energy, a characteristic length L for the slowing down of neutrons to that energy (similar to the slowing down length discussed in section 2.2.1) may be used to determine the neutron flux at a spherical surface of radius r .

$$\phi(r) = \phi_0 e^{-r/L} \quad 2-36$$

Similarly, the mass attenuation coefficient ξ and bulk density are sufficient to determine the gamma-ray transport efficiency Ω .

$$\Omega(r) = e^{-\xi \rho_b r} \quad 2-37$$

Using these simplifying assumptions, Equation 2-35 may be reduced to the following workable form.

$$C. R. = g(t, \tau) \epsilon b N \int_{r=0}^{\infty} \phi_0 \sigma e^{-r(1/L + \xi \rho_b)} \quad 2-38$$

2.6.5 Conflicting gamma-ray energies

Occasionally there will be gamma rays from different activated nuclides that nearly coincide in energy. An example is the reaction $^{56}\text{Fe}(n,p)^{56}\text{Mn}$ in which ^{56}Mn decays with a 2.6 hour half-life and the emission of an 846.6 keV gamma ray, which nearly coincides with the 843.8 keV gamma ray from the 9.45 minute decay of ^{27}Mg . These conflicts can be minimized by maintaining good energy resolution in the spectrometer apparatus. When peaks are partially overlapping, fitting routines can be used to determine the area of each peak, with uncertainties determined by the sizes, widths, and proximity of the peaks.

2.7 Counting statistics in pulse height spectroscopy

When performing radioactive decay measurements, the probability of recording an event is small compared to the number of nuclei involved. In the parlance of the statistician, the probability of success for each trial is small compared to the number of trials. Thus the Poisson distribution, a simplification of the more general binomial distribution, is used in assessing the statistical fluctuation in the sampling of these events [39]. In a Poisson distribution, the square root of the mean \bar{x} is used as the predicted value for standard deviation. When assessing a single measurement, the number of counted events N is used as an estimate for the mean number of events to be expected \bar{x} if the measurement were repeated several times. Then \sqrt{N} is used as an estimate for $\sqrt{\bar{x}}$. If a measurement is repeated a number of times, then the average measured value \bar{N} is used to estimate \bar{x} , and a comparison can be made between the distribution of measured values and the distribution predicted by \bar{x} .

In pulse height spectroscopy, the events that are counted are signals falling into the several channels of a multi-channel analyzer. A portion of a simple pulse height distribution is shown in Figure 2-14. Here, the number of full-energy gamma rays sampled in the measurement is the summation of the events counted in channels 1773 through 1785, minus a background level which is present in all channels and is determined by averaging the number of events found in three channels flanking each end of the peak.

The significance of the peak area in terms of its standard deviation σ can be estimated by summing the effect of standard deviations in each channel, using the basic rule of error propagation, as follows. If y is a function of independent variables x_i where $i = 1$ to n , then the following equation is useful.

$$\sigma_y^2 = \sum_{i=1}^n \left(\frac{\partial y}{\partial x_i} \right)^2 \sigma_{x_i}^2 \quad 2-39$$

For a summation of thirteen channels across the region of the pulse height spectrum, minus a background level established by six flanking channels, the peak area and standard deviation are given by the following expressions.

$$y = \left[\sum_{i=1773}^{1785} x_i \right] - \frac{1785 - 1773 + 1}{6} \left[\sum_{i=1770}^{1772} x_i + \sum_{i=1786}^{1788} x_i \right] = 18325 \quad 2-40$$

$$\sigma_y^2 = \left[\sum_{i=1773}^{1785} x_i \right] + \left(-\frac{13}{6} \right)^2 \left[\sum_{i=1770}^{1772} x_i + \sum_{i=1786}^{1788} x_i \right] = 61443 = 248^2 \quad 2-41$$

The effect of detector properties on the statistics of peak areas is discussed further in Appendix A, using the data of Figure 2-14.

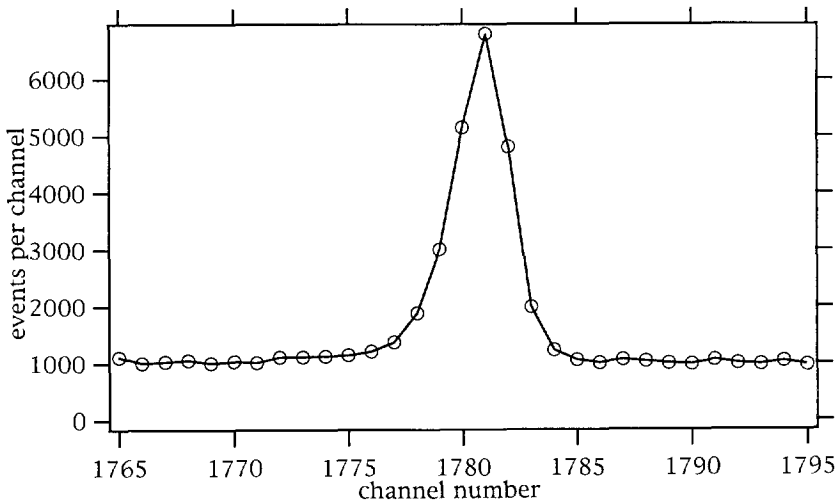


Figure 2-14. Portion of a pulse height distribution with an essentially flat background component.

This chapter will outline the experience gained to date in the application of nuclear spectroscopy techniques to the borehole environment. Today, there are four types of gamma-ray spectroscopic measurements in use which result in estimates of elemental concentrations in the rock and contribute to the geochemical analyses. Borehole logging of natural gamma-ray activity, pulsed-neutron gamma-ray spectroscopy from both inelastic and capture reactions, and delayed gamma-ray activity are performed separately or in combination to provide elemental analyses.

Most implementations of the methods rely on inorganic scintillators, either thallium-activated sodium iodide, NaI(Tl), bismuth germanate, BGO, or gadolinium orthosilicate, GSO. Germanium detectors are used in several research instruments. Development and application of gamma-ray spectroscopic technology for use in boreholes has proceeded since the 1970's, and geochemical analyses based on this technology have become useful in diverse situations. Gamma-ray spectroscopy is used for in situ geologic analysis in oilfield, mining, and scientific drilling programs [12-18, 40-48]. Additionally, instrumentation relying on these methods is being developed for incorporation into spacecraft for analyses of planetary surfaces [24].

Borehole delayed neutron activation techniques based on large spatial separation of source and detector are more closely related to natural gamma-ray techniques than to pulsed neutron spectroscopic methods. Because of the long time constants of decay, they operate independently of the source pulsing method and do not rely on precise spectral gating techniques. Additionally, and similar to the natural radioisotopes, the decay gamma rays are typically emitted at only one or a few energies, as opposed to the dozens of gamma-ray emission energies possible from many inelastic and prompt capture reactions. Because of this similarity in techniques, much of the discussion in this chapter is related to the experience gained with natural gamma-ray logging.

3.1 Natural activity gamma-ray spectroscopy

The first nuclear well logs were recordings of the total natural gamma ray activity of the formation, which were used to delineate shales from other rocks because of the generally higher concentrations of radioactive elements

associated with clay minerals. This primary feature of total gamma ray logs has made them invaluable in assessment of individual formations and as correlative tools for mapping of geologic structure, as well as provision of depth control for subsequent descents into the wellbore. Estimates of clay fraction from total gamma-ray logs have been a standard part of formation evaluation for many years and have undergone many refinements. However, it is well recognized that the radioactivity of an earth formation is not *strictly* related to clay mineral content, but can be related to other features such as feldspar content and fracturing, among others. Also, the radioactivity of clay minerals varies widely depending on clay type and origin.

It has long been recognized that the gamma-ray activity of the earth comes from decay of potassium (^{40}K) and the decay series of both thorium and uranium, and that these three elements are concentrated or depleted preferentially by provenance of source material and by geological processes during and after lithification. For example, uranium concentration is often associated with solution processes, and thorium with heavy accessory mineralization. Potassium, of course, is a constituent of orthoclase and micas. So it is possible to learn something about the rock and clay mineralogy by measurement and separation of the natural gamma-ray components.

Natural gamma ray spectrometry is an extension of total gamma ray logging which spectrally separates gamma rays into the three groups and provides a continuous log of mass concentrations [5]. Due to the introduction of this measurement, the definition of clay minerals was refined, as the uranium content could be separated [70]. With this separation, new additional aspects opened, such as the identification of graphite in crystalline rocks which is normally associated with slickensides and faults, and organic material in dolomite. A correlation has also been observed between high thorium content and permeability, particularly in crystalline rocks [70].

The instrumentation for natural gamma ray spectrometry is fairly simple, consisting of as large a gamma-ray detector as is reasonable to incorporate in a sonde, plus associated electronics including an analog-to-digital converter (ADC) and cable telemetry. A pulse height spectrum of natural radioactivity as recorded by a large germanium detector is presented in Figure 3-1. Peaks in the pulse height spectrum have been identified by their energies that result from decay of specific nuclides in the decay series. Prominent features representing the uranium series are from the decay of ^{214}Bi . Decay of ^{208}Tl results in the most prominent emissions of the thorium series. It can be demonstrated that the photopeak areas are proportional to mass concentrations

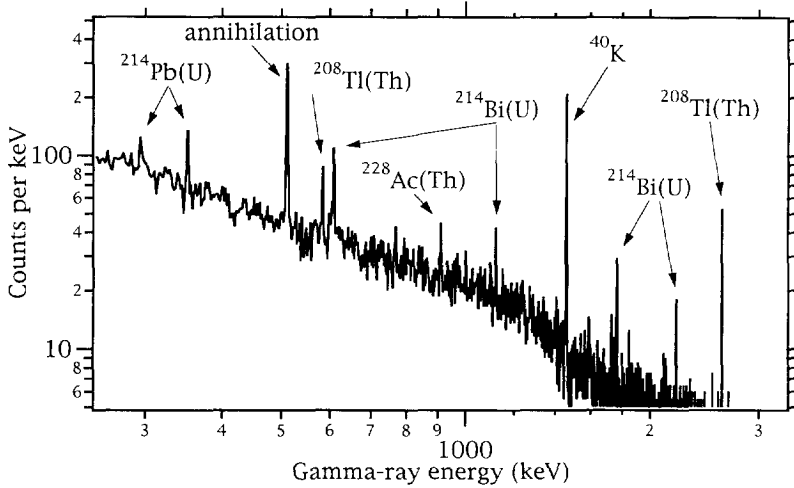


Figure 3.1 The pulse height spectrum of natural gamma rays as recorded by a large germanium detector records shows activity from the thorium and uranium series and from the decay of ^{40}K .

of the decaying species by applying Equation 2-37, the expression for gamma ray transport efficiency $\Omega(r)$, to a case where gamma ray source strength s does not vary with position in an infinite homogeneous medium. A small volume element of the medium at a distance r from some detector position, with radial thickness dr and spatial angle $d\theta$ will have volume $r^2 dr d\theta$, thus the number of particles emitted per unit of time will be $s r^2 dr d\theta$. The volume element will contribute an unscattered flux $d^2 I$ at the detector position.

$$d^2 I = \frac{\Omega(r)}{4\pi r^2} s r^2 dr d\theta \quad 3-1$$

There is no angular dependence of s or Ω , so the integration over θ can be made easily.

$$dI = \frac{\Omega(r)}{4\pi} s dr \int_{\theta} d\theta = \Omega(r) s dr \quad 3-2$$

Integration over the radius results in the flux I of unscattered gamma rays at the detector position. Examination of the dimensions in this expression reveals that a sampling of I by a detector will be proportional to s/ρ_b , because the mass attenuation coefficient ξ only changes to the extent that A/Z deviates from 2

(equal to the extent that bulk density deviates from electron density, as explained in the previous chapter). Count rates indicative of s/ρ_b can thus be expressed as mass concentrations.

$$I = s \int_{r=0}^{\infty} \Omega(r) dr = s \int_{r=0}^{\infty} e^{-\xi} \rho_b r dr = \frac{s}{\xi \rho_b} \quad 3-3$$

Accuracy of the mass concentrations obtained in this fashion will be affected by eccentricity of the sonde in the borehole, and by borehole size, shape, and contents. These factors will alter the flux of unscattered gamma rays reaching the detector by changing the distance and the scattering medium which gamma rays must traverse. The borehole may also contain substantial potassium in the form of "KCl mud", causing high apparent values for potassium concentration. When operating in cased wells, the casing and cement will also have an effect, as will the buildup of scale which often contains uranium. Correction algorithms are usually applied to compensate for these environmental effects, when they are recognized. The industry standard for absolute calibration of natural gamma ray spectrometers is a synthetic formation maintained at the University of Houston, containing known amounts of K, U, and Th. [23]

Because photopeak contributions of the individual radioactive elements are resolvable in a germanium spectrometer, precision of the mass concentrations will simply be the precision of the photopeak areas. Thus, absolute detector efficiency and integration time for the measurement will determine the precision. For potassium, there is only one photopeak, so the fractional uncertainty of the mass concentration will be the same as the fractional uncertainty of the peak area. Concentrations of Th and U may be calculated using each representative photopeak, assuming equilibrium conditions of the decay series, and averaged in an appropriately weighted fashion to optimize the precision of the measurement.

A calculated, noise-free pulse height spectrum of natural activity as would be seen by a BGO crystal is displayed in Figure 3-2 (a). Resolution of the detector system is 13% FWHM at 662 keV. Despite the poor energy resolution of BGO as compared to sodium iodide, there are advantages from its use in this application. Its high density, almost twice that of NaI, and the atomic number of 83 for bismuth result in a higher efficiency for energy deposition, larger photofraction, larger peak-to Compton ratio, and lesser prominence of escape peaks than in NaI.

Contributions to the pulse height spectrum from each of the radioactive elements are also displayed in the figure. The shape of the contributions, or *standards*, has been determined by a combination of experimental and modeling data. Methods that must be used to extract mass concentrations from the pulse height spectrum are based on the shape of the standards, and fall into the main groups of *direct* calculation or *least-squares* fitting. In either case, the practice has generally been the representation of principal components in the data by summation of the pulse height spectrum into a handful of energy *windows* W_i as illustrated in Figure 3-2(b).

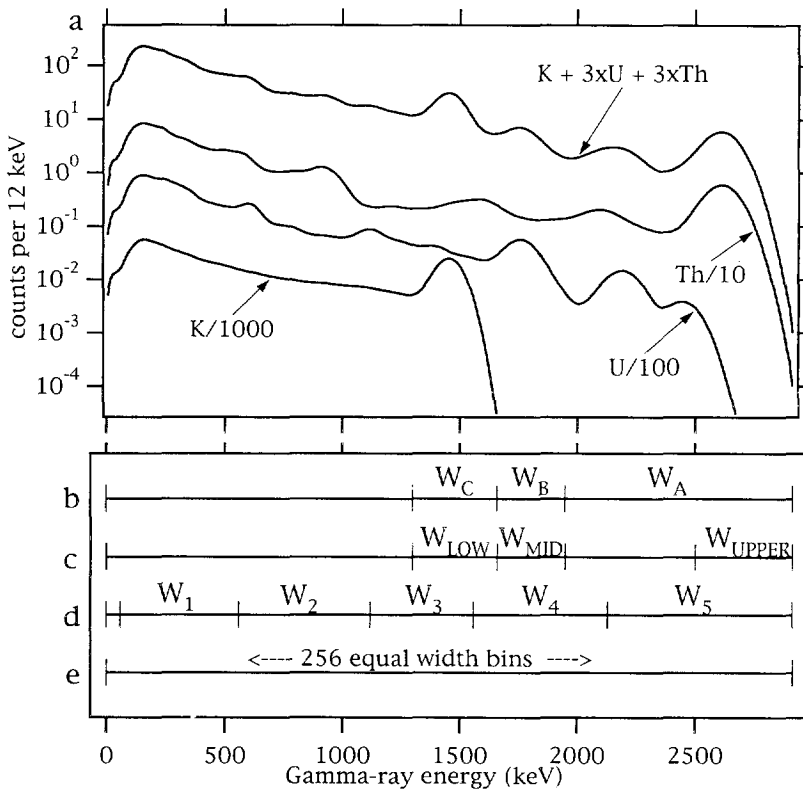


Figure 3-2 (a) The simulated, noise-free pulse height spectrum of natural gamma ray activity, as would be seen by a BGO detector, is the uppermost curve in the plot. Beneath the spectrum are the spectral standards for K, U, and Th, which have been divided by 1000, 100, and 10, respectively, before plotting. The shape of the simulated spectrum is obtained by mixing standards for K:U:Th in the ratio 1:3:3, and is normalized so that the total number of counts in the spectrum is 14000. This represents about ten seconds of wireline logging in a shale. (b)-(e) Several energy window configurations have been used for spectral separation.

3.1.1 Direct calculation

If there are three windows, then the number of counts C attributable to each of the three unknowns Th, U, and K can be calculated directly, since the events from each element will be distributed amongst the three windows in known fractional amounts α as determined from the standards.

$$\begin{bmatrix} C_{Th} \\ C_U \\ C_K \end{bmatrix} = \begin{bmatrix} \alpha_{Th,a} & \alpha_{Th,b} & \alpha_{Th,c} \\ \alpha_{U,a} & \alpha_{U,b} & \alpha_{U,c} \\ \alpha_{K,a} & \alpha_{K,b} & \alpha_{K,c} \end{bmatrix} \begin{bmatrix} W_a \\ W_b \\ W_c \end{bmatrix} \quad 3-4$$

Statistical uncertainties σ in the number of events C will be as follows.

$$\begin{bmatrix} \sigma_{Th}^2 \\ \sigma_U^2 \\ \sigma_K^2 \end{bmatrix} = \begin{bmatrix} \alpha_{Th,a}^2 & \alpha_{Th,b}^2 & \alpha_{Th,c}^2 \\ \alpha_{U,a}^2 & \alpha_{U,b}^2 & \alpha_{U,c}^2 \\ \alpha_{K,a}^2 & \alpha_{K,b}^2 & \alpha_{K,c}^2 \end{bmatrix} \begin{bmatrix} W_a \\ W_b \\ W_c \end{bmatrix} \quad 3-5$$

The uncertainty will be examined for two extreme cases that will illustrate the desirability of obtaining good energy resolution in the detector. For these illustrations, the total number of counts from all sources will be $W_a + W_b + W_c = T$. We know that the sum of any row in the *inverted response matrix* α must be 1. For the first case, assume that all entries of α are 1/3, meaning that events from each of the decays are distributed equally amongst the three windows. From this, it follows that the expected values for each entry of W and C must be $T/3$ for this case. Then the uncertainties become equal to the measured values $\sigma = C$.

$$\begin{bmatrix} \sigma_{Th}^2 \\ \sigma_U^2 \\ \sigma_K^2 \end{bmatrix} = \begin{bmatrix} 1/9 & 1/9 & 1/9 \\ 1/9 & 1/9 & 1/9 \\ 1/9 & 1/9 & 1/9 \end{bmatrix} \begin{bmatrix} T/3 \\ T/3 \\ T/3 \end{bmatrix} \Rightarrow \begin{bmatrix} \sigma_{Th} \\ \sigma_U \\ \sigma_K \end{bmatrix} = \begin{bmatrix} T/3 \\ T/3 \\ T/3 \end{bmatrix} \quad 3-6$$

The opposite extreme case occurs when the signals from each element are completely separate and appear in exactly one window each. The inverted response matrix becomes a diagonal matrix of ones. Then the uncertainties are minimized to $\sigma = \sqrt{C}$.

$$\begin{bmatrix} \sigma_{Th}^2 \\ \sigma_U^2 \\ \sigma_K^2 \end{bmatrix} = \begin{bmatrix} 1 & 0 & 0 \\ 0 & 1 & 0 \\ 0 & 0 & 1 \end{bmatrix} \begin{bmatrix} W_a \\ W_b \\ W_c \end{bmatrix} \Rightarrow \begin{bmatrix} \sigma_{Th} \\ \sigma_U \\ \sigma_K \end{bmatrix} = \begin{bmatrix} \sqrt{W_a} \\ \sqrt{W_b} \\ \sqrt{W_c} \end{bmatrix} \quad 3-7$$

The first case is hopeless, and the second case is unachievable with a scintillator, but good energy resolution of the detector system and a high photofraction will assist in the effort to diagonalize the inverted response matrix and minimize the statistical uncertainty [49]. A compromise that has been used in the case of natural gamma ray spectroscopy is achieved by constructing the windows as shown in Figure 3-2(c) in such a manner that the upper window W_{up} consists of only thorium contributions (or nearly so), and the middle window W_{mid} is from thorium and uranium only. Then the inverted response matrix becomes triangular and is written with the negative signs to indicate that the values β are corrections to the intended main response of the windows.

$$\begin{bmatrix} C_{Th} \\ C_U \\ C_K \end{bmatrix} = \begin{bmatrix} 1 & 0 & 0 \\ -\beta_{Th,mid} & 1 & 0 \\ -\beta_{Th,low} & -\beta_{U,low} & 1 \end{bmatrix} \begin{bmatrix} W_{up} \\ W_{mid} \\ W_{low} \end{bmatrix} \quad 3-8$$

$$\begin{bmatrix} \sigma_{Th} \\ \sigma_U \\ \sigma_K \end{bmatrix} = \begin{bmatrix} \sqrt{W_{up}} \\ \sqrt{W_{up}\beta_{Th,mid}^2 + W_{mid}} \\ \sqrt{W_{up}\beta_{Th,low}^2 + W_{mid}\beta_{U,low}^2 + W_{low}} \end{bmatrix} \quad 3-9$$

The compromise is that decoupling of the signals requires narrowing of the energy windows, in other words enhancing the response function comes at the expense of statistics. The goal is to establish the proper compromise in the window placement that will optimize sensitivity.

3.1.2 Least-squares fitting

If the number of windows is greater than the number of unknown quantities, as in Figure 3-2(d), then the system is overdetermined, and the techniques of least-squares fitting may be used to determine the unknowns. Often, five windows are chosen, as in the following example, but there need not be any summation of the pulse height spectrum, as illustrated in Figure 3-2(e). The explanation of this process will begin with the *forward model* for the response of each window, shown in Equation 3-10, where the values ζ have been precisely determined, probably experimentally in a well-characterized formation or calibration facility.

$$\begin{bmatrix} W_1 \\ W_2 \\ W_3 \\ W_4 \\ W_5 \end{bmatrix} = \begin{bmatrix} \zeta_{1,Th} & \zeta_{1,U} & \zeta_{1,K} \\ \zeta_{2,Th} & \zeta_{2,U} & \zeta_{2,K} \\ \zeta_{3,Th} & \zeta_{3,U} & \zeta_{3,K} \\ \zeta_{4,Th} & \zeta_{4,U} & \zeta_{4,K} \\ \zeta_{5,Th} & \zeta_{5,U} & \zeta_{5,K} \end{bmatrix} \begin{bmatrix} C_{Th} \\ C_U \\ C_K \end{bmatrix} \quad 3-10$$

The assumption is made that the calibration was done well enough so that the uncertainties in both the elemental concentrations and the five window counting rates are so small that they can be disregarded. Then the response matrix ζ can be determined exactly. In this case the elemental concentrations have a perfect statistical representation in any three members of W . A subsequent measurement in the calibration facility or elsewhere, with less than perfect statistical representation, will result in several possible estimates of the elemental concentrations, depending on which sets of equations are used. The goal of least-squares fitting is to choose the solution that is statistically most likely to be the correct one.

Any solution that is chosen will predict values of W that are different from the measured values, the difference for any one member W_i being termed the residual r_i . The least-squares solution will minimize the quantity $\sum r_i^2$. However, some measured values of W are statistically more significant than others, and this is taken into consideration by performance of a *weighted* least squares solution, where each observation is assigned a weight equal to the reciprocal of its variance $\sigma^2 = W_i$. The quantity to be minimized is

$$r_{sum} = \sum_i \frac{r_i^2}{\sigma_i^2} = \sum_i \frac{r_i^2}{W_i} = \sum_i \frac{1}{W_i} \left(W_i - \begin{bmatrix} \zeta_{i,Th} & \zeta_{i,U} & \zeta_{i,K} \end{bmatrix} \begin{bmatrix} C_{Th} \\ C_U \\ C_K \end{bmatrix} \right)^2 \quad 3-11$$

Usually, the minimum is determined by simultaneous solutions for zeroes in the three derivatives of the residual.

$$\frac{\partial(r_{sum})}{\partial(C_{Th})} = \frac{\partial(r_{sum})}{\partial(C_U)} = \frac{\partial(r_{sum})}{\partial(C_K)} = 0 \quad 3-12$$

The introduction of overdetermined variables and subsequent least-squares fitting will generally serve to reduce the statistical uncertainty of the derived concentrations. This is illustrated by an example using the data of Figure 3-2. The pulse height spectrum was reproduced 300 times, adding noise

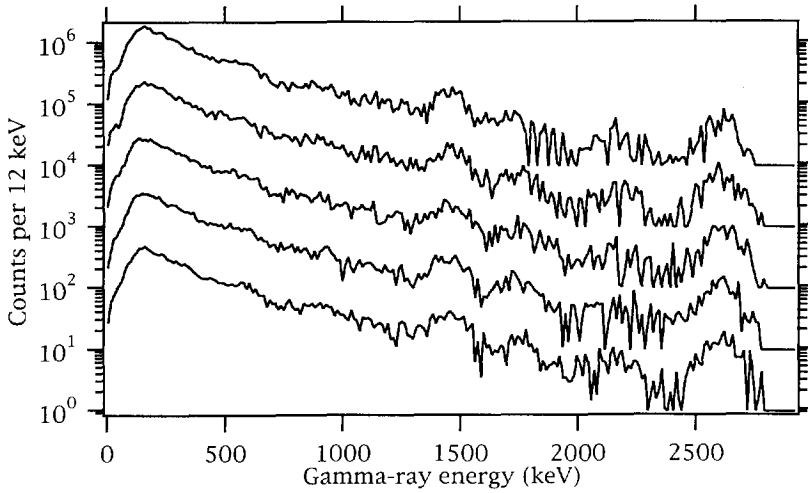


Figure 3-3 The noise associated with 10 seconds of sampling has been added to the spectrum of figure 3-2, to produce 300 noisy spectra. These five spectra were extracted randomly from the dataset. The vertical scale is correct for the bottom spectrum, and the others have been multiplied by factors of ten for display.

	Th	U	K
Average number of counts in each component (input and result of all methods)	6000	6000	2000
Method	σ_{Th}	σ_U	σ_K
Direct calculation	7.3%	11.8%	10.3%
Least squares	6.8%	10.0%	9.4%
Weighted least squares	2.9%	3.1%	4.5%
Ideal (for orthogonal stds.)	1.3%	1.3%	2.2%

Table 3-1 Uncertainties in elemental concentrations from a synthetic data set, using direct calculation and least-squares fitting. The row labeled "ideal" is the minimum uncertainty that would result from any method if the standards from the three elements were orthogonal.

associated with counting statistics to each channel in the distribution. Samples of the noisy spectra are shown in Figure 3-3. Each spectrum contains noise equivalent to ten seconds of data acquisition. The spectra were inverted individually to yield 300 estimates of elemental concentrations using both direct calculation and least-squares fitting.

The direct calculation was done using the three-window scheme depicted in Figure 3-2(c), resulting in standard deviations of the derived Th, U, and K shown in Table 3-1. Least squares fitting was done using 134 individual ADC channels across the span of the three windows. Both non-weighted and weighted least squares fits were made. This comparison shows that a least-squares approach to the data, in particular a weighted least-squares approach, results in a more stable estimate of the elemental concentrations.

3.2 Spectroscopy of γ -rays from inelastic neutron scattering

Widely known as carbon/oxygen (C/O) logging, this technology emerged in the mid-1970s as a method of hydrocarbon detection [7,8]. High energy neutrons from a pulsed 14 MeV neutron generator in the borehole instrument scatter inelastically from nuclei in the formation, causing prompt emission of gamma rays. The detected gamma rays are separated both in time and energy into components that enable the calculation of the carbon-to-oxygen ratio and other relative abundances.

Determination of oil saturation is one of the main goals of wireline logging in the oilfield. Most methods, whether based on resistivity or thermal neutron decay, require knowledge of formation water salinity. The ratio of carbon to oxygen is very diagnostic of the oil-to-water ratio and, to first order, does not depend on the formation water salinity. Thus a measurement of the ratio can provide an estimate of oil saturation independent of the traditional Archie approach. Periodic monitoring of production wells with a C/O logging sonde can provide evidence of changes in saturation in and around producing horizons, such as the diagnosis of breakthrough in waterfloods, coning, and gas expansion. The method is most sensitive in higher porosities, since there is more pore fluid to provide a signal, but has little sensitivity below about 15 percent porosity. The method also requires knowledge of the lithology, particularly about the presence of any carbonates.

The first generation versions of carbon/oxygen sondes required stationary measurements of a few minutes duration to acquire statistically significant data. Recently, versions of second generation sondes have been developed which permit continuous logging of C/O [71]. Gadolinium oxyorthosilicate (GSO) is a

relatively new scintillator material that is ideal for high count rate spectroscopy, and is utilized in the new sondes. It has a light output which decays faster than that of NaI, and it is more dense. Downhole electronic and signal processing capabilities have undergone remarkable improvements to enable the rapid analog-to-digital conversion that is required. The neutron generator is cyclically switched on and off to provide bursts of 14 MeV neutrons of a few tens of microseconds duration, as in Figure 3-4(a). Neutrons enter the formation and slow down by scattering. During each neutron burst cycle, only a few gamma rays, or none, may be detected. But, as the cycle is repeated at a rate of 10,000 times per second, the time structure of the detected gamma rays with respect to the pulsing quickly becomes apparent, and is depicted schematically in Figure 3-4(b). Parts (c) through (f) of the figure represent various components of the detected gamma rays, which constitute both signal and noise in the C/O measurement.

Cross sections for inelastic scattering are only appreciable above a few MeV, and all the neutrons will have slowed to beneath that threshold in considerably less than a microsecond, so the induced gamma-ray activity of interest in this type of logging occurs essentially during the neutron burst, as in Figure 3-4(c). During and after the burst, neutrons continue to slow down until they are eventually captured at epithermal or thermal energies, usually resulting in the emission of prompt gamma rays. The time structure of the capture gamma rays is depicted in Figures 3-4(d) for epithermal neutrons, and Figure 3-4(e) for thermal neutrons. Additionally, there will be activation from both fast and slow neutrons which will be seen as a constant background in addition to the natural gamma rays on this time scale as in Figure 3-4(f).

Gamma rays detected during the neutron burst, or *burst gate*, are digitized, placed in a histogram of pulse heights, and stored in one section of memory. After the burst, gamma rays detected during the *decay gate* are stored in another section of memory. Some devices use another gate, called the activation, or *background gate*, during which pulsing of the generator stops but detection of gamma rays continues so that the level of activation can be estimated. The fraction of time that a spectral acquisition gate is active is termed the *duty factor* δ . After an appropriate integration time, memory contents are read out and transmitted uphole while a new accumulation of data begins. An example of pulse height spectra in the three gates appears in Figure 3-5.

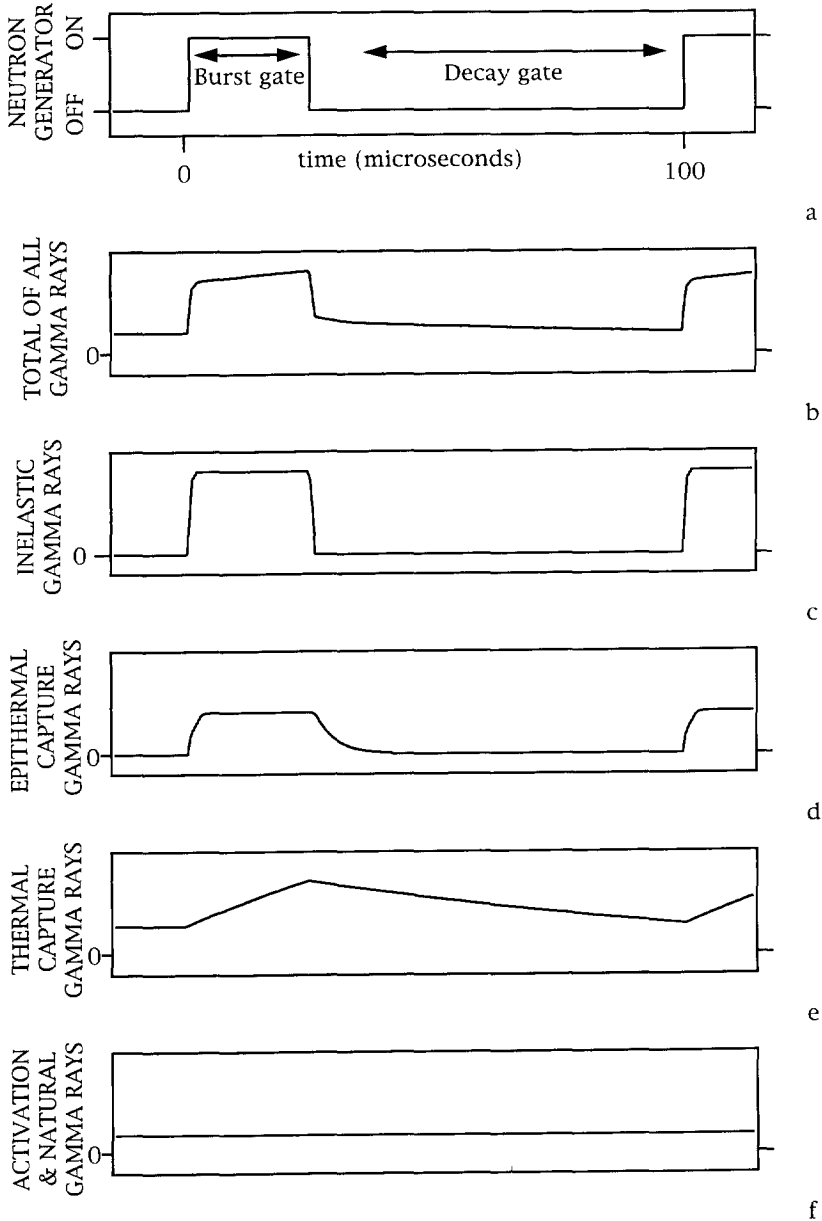


Figure 3-4 The time structures of various gamma-ray components seen by a carbon/oxygen logging tool are depicted schematically. Vertical axes are linear, but scale markings have been omitted. Part (b) is a sum of parts (c)-(f).

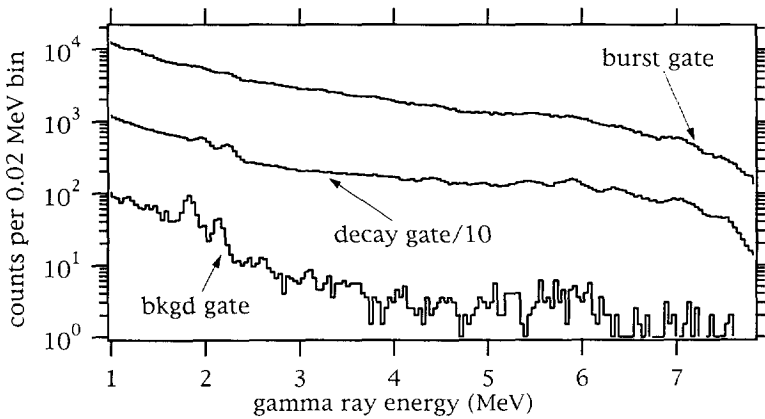


Figure 3-5 A set of spectra from a stationary carbon/oxygen type of measurement inside pipe in a limestone. The decay gate has been divided by ten for plotting. Peaks in the background gate are from iron activation. The decay gate spectrum is also dominated by iron.

Because capture, activation, and natural gamma rays will appear as unwanted contaminations during the burst gate, a method has been developed for their elimination from the pulse height spectrum. The contribution of *epithermal* capture is small, and is not subtracted explicitly. The contribution of natural gamma rays is small compared to the number of counts in the burst gate, as is the contribution of activation gamma rays from the formation, particularly for a continuous measurement. The background due to activation of the sonde is likely to be more substantial. However, the activation and natural backgrounds are treated as one and the same. First, a fraction of the background gate spectrum \mathbf{S}_{bkgd} is subtracted from the decay gate spectrum \mathbf{S}_{decay} to yield the capture spectrum \mathbf{S}_{cap} , assuming that the background rate is constant in all gates. The fraction (it may be more or less than 1) is equal to the ratio of duty factors of the two gates.

$$\mathbf{S}_{cap} = \mathbf{S}_{decay} - \left(\frac{\delta_{decay}}{\delta_{bkgd}} \right) \mathbf{S}_{bkgd} \quad 3-13$$

A similar correction is made to the burst spectrum \mathbf{S}_{burst} which leaves contributions from both inelastic and capture gamma rays in the spectrum $\mathbf{S}_{inel+cap}$.

$$\mathbf{S}_{inel+cap} = \mathbf{S}_{burst} - \left(\frac{\delta_{burst}}{\delta_{bkgd}} \right) \mathbf{S}_{bkgd} \quad 3-14$$

The final subtraction to be made, to yield the "pure" inelastic spectrum \mathbf{S}_{inel} is the removal of a fraction of \mathbf{S}_{cap} from $\mathbf{S}_{inel+cap}$. The fraction to be removed will vary according to the time structure of the capture contribution, a function of the intrinsic thermal decay time of the formation, the borehole, and sonde, and any instrumental effects. It will be slightly larger by a factor f than the ratio of the burst and decay gate duty factors. The apparent decay time τ can be calculated from the data in Figure 3-4(b) and used to estimate the shape of figure 3-4(e), providing an estimate of the factor f , which will also depend on the positions of the gates within the timing scheme.

$$\mathbf{S}_{inel} = \mathbf{S}_{inel+cap} - f\{\tau\} \left(\frac{\delta_{burst}}{\delta_{decay}} \right) \mathbf{S}_{cap} \quad 3-15$$

Equations 3-13, 3-14, and 3-15 may be combined to form the following expression for deriving the pure inelastic spectrum.

$$\mathbf{S}_{inel} = \mathbf{S}_{burst} - f\{\tau\} \left(\frac{\delta_{burst}}{\delta_{decay}} \right) \mathbf{S}_{decay} + (f\{\tau\} - 1) \left(\frac{\delta_{burst}}{\delta_{bkgd}} \right) \mathbf{S}_{bkgd} \quad 3-16$$

An alternative approach that has been used is based on the assumption that for long decay times τ , the function $f\{\tau\}$ approaches 1 and the last term of Equation 3-16 vanishes. Then the background gate is not needed to obtain the corrected spectrum, since background subtraction is done implicitly.

$$\mathbf{S}_{inel} = \mathbf{S}_{burst} - \left(\frac{\delta_{burst}}{\delta_{decay}} \right) \mathbf{S}_{decay} \quad 3-17$$

This simplifying assumption goes a long way toward improving the statistical precision of the corrected spectrum, since the background spectrum \mathbf{S}_{bkgd} and the factor $f\{\tau\}$ are not used. But, this comes at the expense of inaccuracies introduced by contamination of the inelastic spectrum with capture gamma rays. Inelastic and capture spectra derived from the data of Figure 3-5 using the "simple" method are displayed in Figure 3-6.

As with natural gamma-ray spectroscopy, there are a number of methods for decomposing the inelastic gamma-ray spectrum into its elemental components. A weighted least-squares method based on standard elemental responses, as shown in Figure 3-7, may be used, or the contributions may be

calculated directly using windows centered on the positions of peaks in the spectra. Spectra are usually resolved into carbon, oxygen, calcium, silicon, and iron components.

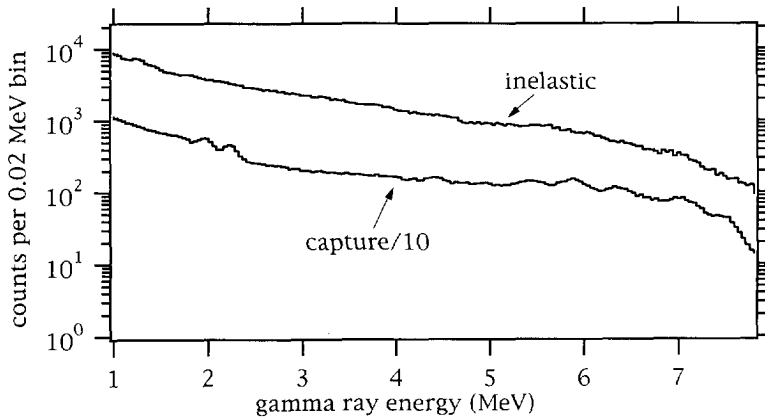


Figure 3-6 "Pure" inelastic and capture spectra of Figure 3-5 after removal of contaminations. The capture spectrum is divided by ten for plotting.

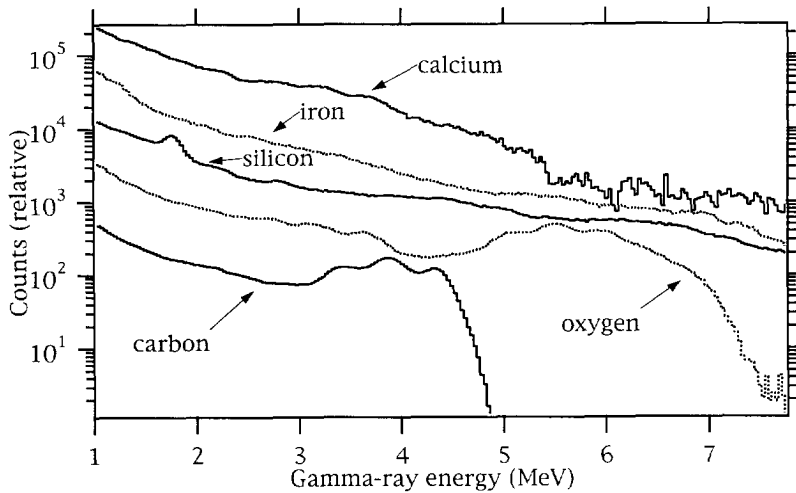


Figure 3-7 Elemental standards for an inelastic gamma-ray spectroscopy device.

3.3 Spectroscopy of gamma rays from thermal neutron capture

The capture gamma ray spectra obtained in pulsed neutron logging may also be used to obtain relative elemental concentrations. The timing scale of C/O logging may be used, or the time scale may be expanded by a factor of about ten to permit better determination of the thermal decay time of the formation. Weighted least-squares fitting to standard elemental responses is done in the same fashion as for C/O or natural gamma-ray logging. Resolvable contributions to capture spectra come from silicon, calcium, iron, sulfur, titanium, hydrogen, chlorine, and gadolinium [23].

A recently developed method based on newer detector materials uses a chemical neutron source to record spectra with a 100% duty factor. In this case, the capture and inelastic standards are used simultaneously to resolve spectral components. Inelastic contributions are small, however, because of the lower energy of the source neutrons. Contributions of carbon and oxygen to the spectra are too small and determined too imprecisely to be of value in estimation of their elemental concentrations.

There are many other minor and trace elements that emit characteristic capture gamma rays or inelastic scattering gamma rays. However, these gamma rays cannot be resolved from those of the major rock forming elements because of the peak broadening associated with scintillators.

3.4 Delayed activation gamma-ray spectroscopy

Fast neutron reactions such as (n,p) , (n,α) , and $(n,2n)$, and neutron capture reactions (n,γ) may generate delayed gamma-ray emission. This may be sensed by a detector, similar to a natural activity detector, that trails some distance behind the neutron source as the logging instrumentation is pulled toward the surface. The scintillator is displaced far enough from the neutron source that it does not see the prompt activity. In sedimentary strata, aluminum is the element most readily measured in this fashion.

Commercial implementations of aluminum logging systems utilize two identical sondes containing scintillators, either sodium iodide or BGO, and a neutron source [9,10]. One sonde precedes the chemical neutron source as the hole is logged, resulting in a log of the natural Th, U, and K activity. The other sonde trails the neutron source and thus records the sum of natural activity and any induced, delayed gamma ray activity. The induced signal is obtained by a subtraction of the two responses, and is converted to an absolute aluminum

concentration by use of the relations established in section 2.6 and a counts-to-concentration calibration of the sonde.

The only induced activity measurable by these systems, because of detector response factors, is the 1779 keV gamma ray emission resulting from the decay of ^{28}Al , which has a 2.246 minute half-life. The measurement of aluminum is complicated by one of the competing reactions listed in Table 1-2. The intermediate nuclide ^{28}Al can be produced by the thermal neutron reaction $^{27}\text{Al}(n,\gamma)$ and the fast neutron reaction $^{28}\text{Si}(n,p)$ which has a threshold of about 4 MeV. Thus, a measurement of the induced activity will contain contributions from both reactions, and a correction must be made by subtracting the silicon contamination in the signal, which may be obtained from a capture gamma-ray spectroscopy measurement.

The correction may be eliminated by use of a source that emits neutrons at energies below the threshold for the $^{28}\text{Si}(n,p)$ reaction. A D,D minitron emits neutrons at about 2.5 MeV, with exact energy dependent on the angle of emission. This is below the $^{28}\text{Si}(n,p)$ threshold, but the intensities reliably achievable in a borehole device are not sufficient to provide a statistically reasonable signal. A D,T accelerator can produce neutrons at a sufficient rate, but the emission energy of 14 MeV will maximize the silicon contribution. Chemical sources provide compromises, emitting neutrons across a broad range of energies, with intensities between those achievable by the two types of accelerators. ^{252}Cf emits a significant fraction of its neutrons below the threshold, and has been used as a neutron source for aluminum activation logging. It provides a smaller high-energy fraction than $^{241}\text{AmBe}$ and other (α,n) sources.

3.5 Combinations of borehole spectroscopy measurements

The measurement techniques described in preceding sections measure the content of one or a few elements, some in absolute concentration, but some only in relative abundance. Since the late 1980's, it has been possible to combine spectrometers for natural, capture, and delayed activity measurements, enabling the continuous measurement of absolute elemental concentrations for thorium, uranium, potassium, aluminum, and relative concentrations of silicon, calcium, sulfur, iron, titanium, and gadolinium in one logging pass [10]. The measurements are combined to estimate absolute concentrations of all ten elements based on an innovative approach. A model has been developed that relates the concentrations of unmeasured elements (primarily oxygen, and usually carbon) to the concentration of measured elements by assuming oxide

and carbonate forms (and one sulfide). Developed for sedimentary environments, this model has been shown to work well in crystalline rocks also, with minor modifications.

The largest direct use of elemental measurements is the estimation of mineralogy. A half-dozen element-to-mineral models have been developed to provide linear inversion of the data in most sedimentary environments, typically assumed to contain up to ten minerals. A variety of other geologic parameters may also be estimated from the elemental concentrations, such as cation exchange capacity, grain density, porosity, and others. When combined with additional geologic knowledge, the mineralogy and other parameters can often lead to inferences concerning the depositional environment, grain sizes, and even permeability [12-18, 40-48].

3.6 Limitations of gamma-ray spectrometers

A limitation in the downhole methods lies in the use of scintillators as gamma-ray detectors. Generally, the energy resolution of scintillators results in an inherent limit of about ten components which may be resolved from a spectrum. The exact number of quantifiable constituents is also dependent on the uniqueness of spectral shapes from each component and the signal amplitude from each component. For thermal neutron capture spectroscopy, ten spectral components are currently resolved in commercial borehole devices.

In the case of aluminum measurement by delayed activity, only the difference between two gross signals is used, as spectroscopic methods cannot be utilized. The 1779 keV gamma ray used as a measure of aluminum is too close to the natural ^{214}Bi (uranium series) gamma ray emission at 1764 keV to be resolved spectroscopically with a scintillator. All other delayed emissions are unresolvable because of their lesser amplitude and because of limitations in neutron source strength, detector resolution, and detector efficiency.

3.7 Discussion and implications

A sonde for delayed activation logging requires a neutron source and a gamma-ray spectrometer that are separated by about two meters to eliminate detection of prompt gamma-ray activity. The timing scheme, consisting of irradiation, delay, and acquisition times, are then a function of only the logging speed and the vertical averaging interval. At a logging speed of 200 meters per hour, for example, the delay time is 36 seconds. Because of the large separation and slow timing, spectral acquisition may be completely asynchronous to any pulsing of the neutron source, which generally has a period between several

tens of microseconds and one millisecond. Count rates in the spectrometer will not show the structure of the source pulsing, but will slowly vary with the encountered lithology. In these respects, delayed activation logging resembles logging of natural activity.

The review of direct calculation and least-squares techniques as applied to natural gamma-ray logging (section 3.1) confirms that a weighted least-squares solution is more statistically significant than the direct method. This occurs because the responses to each of the elements (thorium, uranium, and potassium) are not orthogonal (they have similarities). There will also be ambiguities in the activation responses to elements, as discussed in section 1.4 and again in section 2.6.3. For the elements discussed in these sections, sodium, magnesium, aluminum, and silicon, there are fourteen gamma-ray energies whose peak areas can be determined from a pulse height spectrum. Six of the gamma-ray energies are ambiguous: they can originate from two or more of the elements. A least-squares technique will be attempted to resolve the elemental contributions.

This chapter contains a description of the experimental facilities that were constructed for this research, including the requirements for the facilities and the design considerations. In the course of the research, a method was developed to extend the efficiency calibration of a germanium detector to higher gamma-ray energy. The method is also discussed in this chapter.

Verification of the activation cross section response integrals for four elements is one goal of the research project. Measurements will be made to determine the delayed gamma-ray activity from samples containing sodium, magnesium, aluminum, or silicon. Next, calculations of the activity will be performed, using a library of cross sections, an exact simulation of the experimental geometry and materials, and a Monte Carlo radiation transport modeling code. Comparison of the measured and modeled activities will provide verification of response integrals.

The experimental phase involves the use of a 14 MeV neutron generator in a moderating environment, so that the sample is exposed to a continuous range of neutron energies. Subsequently, the delayed activity will be counted with a large, high purity germanium (HPGe) detector.

Another goal of the research is to provide estimates of sonde sensitivity to concentrations of a few dozen elements. These estimates will be based on measurements of the delayed gamma-ray activity from samples containing the elements. The measurements will use the same experimental setup and procedures as the cross section verification measurements.

4.1 Considerations of the Experimental Design

There are two alternatives to the mechanics of an activation measurement. The sample can be transferred for counting as is done in thermal neutron activation analysis at reactor sites, or the neutron source can be replaced with a detector while the sample is left in place, similar to a borehole measurement. Past experience with neutron activation experiments has shown that it is difficult to obtain consistently repeatable data in the laboratory with a borehole geometry because of the difficulty in accurate placement of the source

and detector*. The sample transfer approach can be done more quickly and replicably, but requires a smaller sample and precludes an exact borehole geometry. A strict adherence to borehole geometry is not necessary to satisfy the goal of cross section verification, so the sample transfer method is chosen. Thus, separate irradiation and counting facilities must be designed and implemented.

4.1.1 Irradiation facility

Several functions must be fulfilled by the irradiation facility. It must provide for replicable positioning of the neutron source and the sample container within a moderating medium so that repeatable and consistent results may be obtained in successive experiments. Because the output of a neutron generator varies with time, a system to monitor the neutron output should be established to measure the yield throughout a sample irradiation. The sample itself may have a noticeable effect on the neutron flux, and measurements of the neutron output should be independent of this effect. The system should permit quick retrieval and transfer of a sample after irradiation so that reasonable counting statistics may be obtained for rapidly decaying nuclides. The absolute times of irradiation and retrieval must be recorded, and the irradiation process should be automated as much as possible for consistency. Control of the neutron generator and monitoring apparatus must be performed remotely for safe operation. Finally, the facility must contain the neutron population and secondary gamma rays so that levels of activity outside the facility are as low as reasonably achievable.

4.1.1.1 Moderating medium

One essential design aspect is that the neutron spectrum $\phi(E, V)$ in the experiment should bear some resemblance to that seen in a borehole environment for the response verification to have any validity or applicability, because the response integral is a function of flux as well as the cross sections $\sigma(E)$, as shown

$$Y = N \int_V \int_E \phi(E, V) \sigma(E) dE dV \quad 4-1$$

* Experience has shown that it is easier to obtain good, repeatable data in field conditions with a true downhole sonde than with a mockup in the laboratory.

A tank of water was chosen as the medium in which to irradiate the samples, because its moderation properties will provide a reasonable approximation of the flux in a borehole geometry.

Calculations of the neutron energy spectrum in water and several types of sedimentary rocks have been carried out by a Monte Carlo modeling process (see chapter 7) for several distances from a 14 MeV point source in an infinite medium. Results are presented in Appendix B, and excerpted in Figure 4-1. Comparison of the spectra in water, 5% porosity (5 pu) dolomite, and 30 pu sandstone reveal the same general shape, with several differences. The water spectra are flatter across the epithermal region, smoother in the MeV region, and possess a larger thermal component, particularly when compared to the 5 pu dolomite. The data of Figure 4-1 are the average fluxes for the region from 5 to 10 cm away from the source, similar to the expected depth of investigation of a borehole measurement. The same types of differences are apparent in the other data of Appendix B, but diminish with increasing porosity of the rocks.

Comparisons of neutron spectra from a 14 MeV source in water and zero porosity rocks have been made elsewhere [50] from measurements and infinite media calculations, also revealing slightly flatter neutron spectra in water in the same energy region.

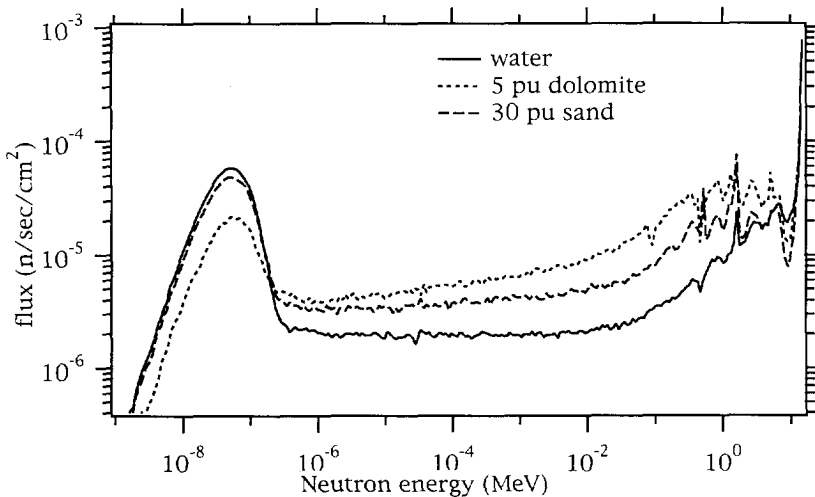


Figure 4-1 Neutron spectra in water, 5 pu dolomite, and 30 pu sand have been calculated using a Monte Carlo program, assuming a 14 MeV point source and an infinite medium. These data are the average fluxes in the region from 5 to 10 cm from the source, using logarithmically equal energy binning.

4.1.1.2 Structural aspects

Acrylic tubes are used to hold the 14 MeV neutron source, the sample, and three neutron monitors in place near the center of the water tank (Figure 4-2), which is constructed from 4 mm thick stainless steel. Acrylic is used for the tubes because it is rigid and has a density and hydrogen content reasonably close to that of water, making its neutron moderating properties similar.

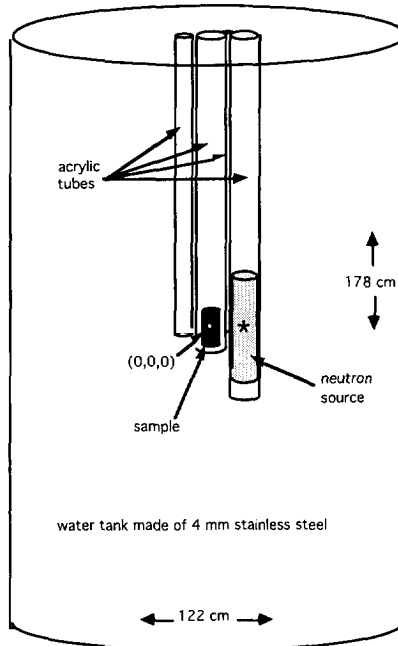


Figure 4-2 The irradiation facility contains two 9 cm outer diameter acrylic tubes to hold the accelerator and sample, and two smaller tubes, one for a detector used to monitor neutron intensity, and one spare. Center of source and detector are separated by a distance of 9.6 cm.

4.1.1.3 Sample considerations

A sample size of 150 to 500 grams in a 240 ml polyethylene bottle is chosen to provide convenience in weighing, mixing, handling during transfer, and a detector counting rate not burdened by excessive dead time or pulse pileup. Because the miniaturized (D-T) neutron generator provides a maximum *total* output of about 10^9 neutrons per second, compared to typical reactor thermal neutron fluxes of 10^{13} neutrons per second *per square centimeter*, a considerably larger sample than for TNAA is required to obtain statistically significant results. Calculations and a few preliminary measurements reveal

that for the elements under consideration, the required quantity is a few tens or hundreds of grams. A compound containing the target element was used by itself or was thoroughly mixed with a filler of calcium carbonate. In either case, the sample bottle was entirely filled to maintain a geometrical consistency of target material throughout the series of measurements. The filler itself is of little importance, unless it happens to supply a competing reaction or a conflicting gamma ray to the target element.

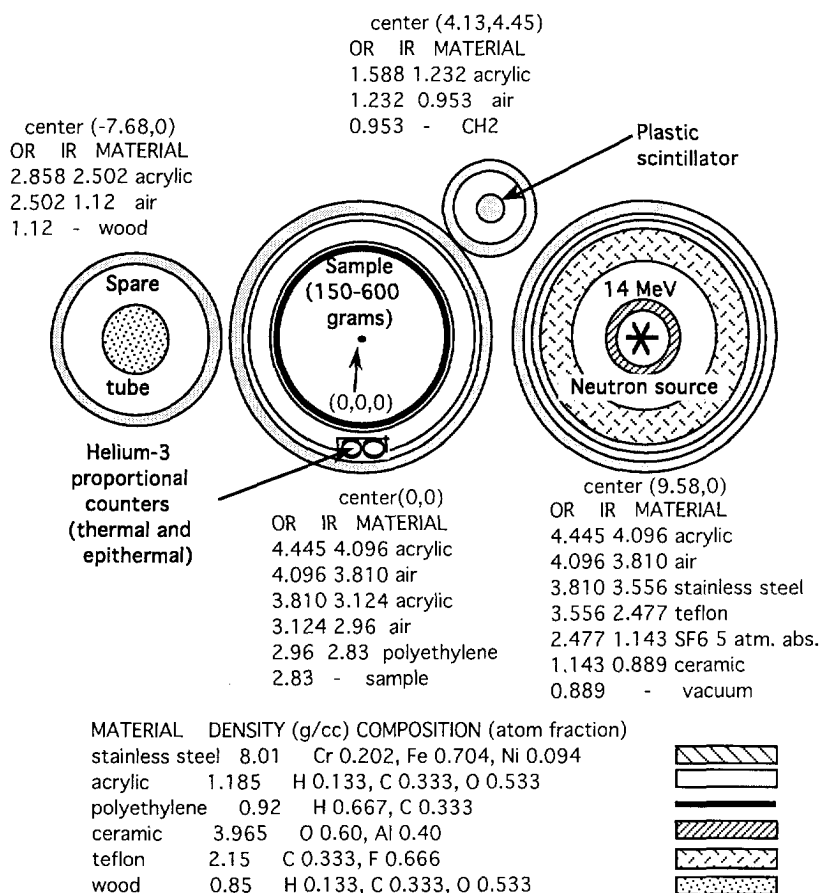
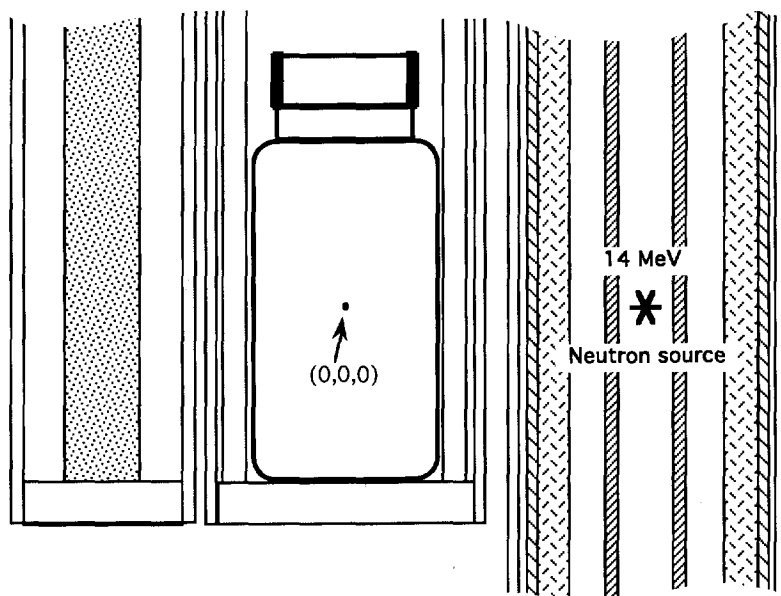


Figure 4-3 A plan view of the tube arrangement at the center of the sample shows the location of three neutron monitors. The proportional counters are 6 X 25 mm, 10 atm. ³He tubes; one is clad with 0.6 mm of cadmium. The plastic scintillator for monitoring the hard flux is 10 X 10 mm. OR and IR are abbreviations for outer radius and inner radius, which are expressed in centimeters.



MATERIAL	DENSITY (g/cc)	COMPOSITION (atom fraction)
stainless steel	8.01	Cr 0.202, Fe 0.704, Ni 0.094
acrylic	1.185	H 0.133, C 0.333, O 0.533
polyethylene	0.92	H 0.667, C 0.333
ceramic	3.965	O 0.60, Al 0.40
teflon	2.15	C 0.333, F 0.666
wood	0.85	H 0.133, C 0.333, O 0.533



Figure 4-4 An expanded cross section through the center of the sample and accelerator. The sample fits snugly into the tube, so no additional centering devices are necessary. The accelerator can be removed for service and replaced in exactly the same position. The tube at left was not used in this series of experiments.

To obtain a higher count rate and make replicable measurements, the sample bottle is oriented so that the side of the sample facing the neutron source will later on be the same side that faces the gamma ray detector. A mark on one side of the sample bottle neck is lined up with a similar mark on the sample tube, facing the neutron source. A long piece of string is used to lower the bottle into the acrylic tube and permits quick retrieval at transfer time.

4.1.1.4 Neutron monitors

The output of the neutron generator varies slowly as its temperature changes, as it ages, and when it is turned off and on. Three neutron detectors, with positions shown in Figure 4-3, are used to monitor the neutron flux in different regions of the energy spectrum. A bare proportional counter of dimensions 6 X 25 mm, with 10 atmospheres ^3He gas pressure is used to record the thermal flux. A similar detector, clad with 0.6 mm cadmium, is sensitive to the flux somewhat above 0.5 eV. The third detector is a 10 X 10 mm plastic scintillator coupled to a 13 mm photomultiplier for measurement of the 14 MeV flux. Details of the neutron monitor electronics are presented in Appendix D.

A multichannel scaler records a history of the detector responses over the irradiation time by binning events in user specified intervals known as *dwell times*, which are set to an appropriate interval for the irradiation time, typically five seconds. For each neutron monitor, this device has a counter whose contents are dumped into an addressable memory location at the end of each dwell period, enabling estimation of the effective source intensity during post-processing. A fourth multichannel scaler channel is used to record the output from a fixed rate pulser that is used later, in the spectral acquisition phase.

The neutron monitors were tested to demonstrate their lack of response to the sample material and density. First, the lightest sample (132 grams of chemically pure MgO) and next, the heaviest sample (588 grams of alumina blasting sand) were inserted in the sample tube without turning the accelerator off or altering the controls, and the monitor rates were recorded. The epithermal detector showed the most response, increasing by 1.026 ± 0.002 when the dense sample replaced the light sample. The thermal detector decreased by 1.022 ± 0.0004 for the same circumstances, and the plastic scintillator showed an increase of only 1.001 ± 0.002 . Thus, there is good confidence that the neutron monitors are not sensitive to the sample.

A calibration of the neutron monitor response was performed in terms of absolute output of the neutron generator. In this calibration procedure [51], the neutron generator is centered within a copper sleeve of specific dimensions and purity. The copper sleeve is activated with the neutron generator under controlled conditions, and its subsequent delayed activity counted with a calibrated detector. A calibration had previously been established that relates the detected copper activity to absolute output of the neutron generator. At operating setpoints used for the experiments, the output of the generator was found to be $1.35 \times 10^8 \pm 15\% n/s$. When divided into count rates obtained from the neutron monitors, this figure reveals that each recorded count in the plastic

scintillator corresponds to about 106000 generated neutrons. For the epithermal detector, the ratio is 1 count per 47300 neutrons, and for the thermal detector, 1 count per 5450 neutrons.

4.1.1.5 Safety aspects

The irradiation tank is surrounded by a 30 cm thick wall of paraffin wax over the entire height, resulting in a level of activity within the radiation transport laboratory of 1 mrem per hour at the outer surface of the paraffin when the neutron generator is turned to its maximum output. The highest level observed in the control room is less than 0.1 mrem per hour, and a monitor placed at the operator's console shows no perceptible increase when the neutron generator is switched on.

4.1.2 Counting facility

A number of functions must be fulfilled by the counting facility. It must quickly and easily accept the transferred sample. Both the sample and detector must be capable of being removed and replaced in exactly the same position to ensure replicable results. The pulse height spectrum should contain as much signal and as little noise as possible. Pulse pileup and system dead time should be minimized as much as is reasonable, and provision must be made for their measurement. The acquisition should initiate and proceed automatically in conjunction with the control of the irradiation, to reduce mistakes and improve consistency.

4.1.2.1 Germanium detector

Attempts have been made in the past to use germanium detectors in all types of borehole gamma-ray spectroscopy measurements. In these trials, which have used detectors with efficiencies in the range of, at most, $\epsilon_{3X3} = 15 - 20\%$, counting statistics rather than detector resolution have been the limitation on successful implementation. In low flux intensity measurements such as natural and activation gamma-ray spectrometry, the small outline of these detectors, perhaps 4 cm diameter X 4 cm. length, presents a small solid angle for detection. When coupled with a poor photofraction, this results in too few counts in the photopeaks and too high a continuum under the peaks. In high flux intensities, these same problems occur, but are compounded by pileup and dead time. To maintain good energy resolution, substantial shaping times are required during amplification, resulting in significant pulse

pileup, particularly during the neutron burst when the gamma-ray flux is highest.

Larger high-purity germanium spectrometers, such as the 7.6 cm diameter X 8.8 cm. length detector used in this study, offer significantly greater potential for surmounting these problems because of their much larger photofraction. When assessing the photofraction, efficiency values \mathcal{E}_{3X3} are based on the response of a germanium detectors to a 1333 keV gamma ray, relative to the response of a 3" X 3" sodium iodide crystal. Detectors with efficiencies $\mathcal{E}_{3X3} > 100\%$ are available. The ratio of efficiencies can then be used as a crude comparison of large and small germanium detectors. However, the photofraction for higher energy gamma rays will increase much more in a large detector than is estimated by the ratio of \mathcal{E}_{3X3} values. A series of measurements was made with large ($\mathcal{E}_{3X3} = 99\%$) and smaller ($\mathcal{E}_{3X3} = 33\%$) germanium detectors using gamma ray sources of several energies from 0.5 MeV to 3 MeV. The ratios of peak areas from these measurements are presented in Figure 4-5 and reveal a factor of improvement of 5 to 10 for higher energy gamma rays.

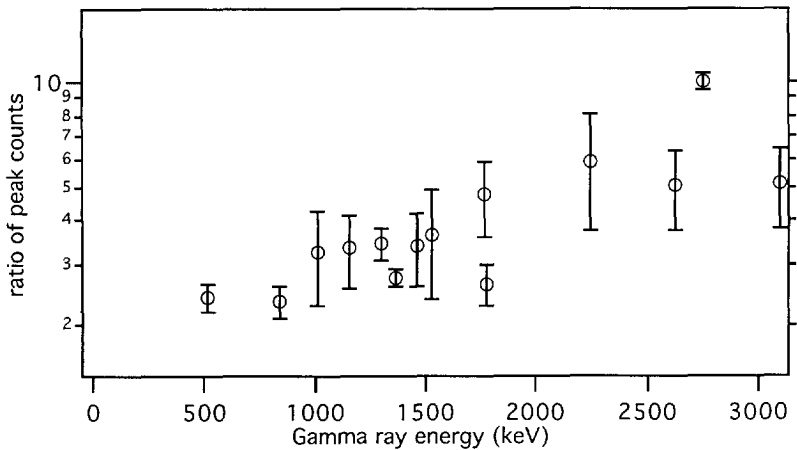


Figure 4-5 A series of recordings of gamma-ray activity were made with a large HPGe ($\mathcal{E}_{3X3} = 99\%$) and a smaller HPGe ($\mathcal{E}_{3X3} = 33\%$). The ratio of measured photopeak areas from the two detectors (large detector / small detector) reveals that the photopeak efficiency increases substantially for energies above 1333 keV, where the ratio has been normalized to 3.0.

Counting of decay gamma rays in the experiments is done with a large Ortec high-purity germanium detector in a shallow-hole probe configuration, depicted schematically in Figure 2-7, and in greater detail in Appendix C. The shallow-hole probe design is a convenient package for these types of experiments, since it has a small reservoir for liquid nitrogen and can be operated when removed from its main source of liquid nitrogen. Holding time of the Dewar/cryostat assembly when starting with a full liquid nitrogen reservoir is in excess of 24 hours. At the top of the nitrogen reservoir is a threaded fitting (not shown in the figure), which can be used to support the entire assembly. The germanium crystal is a coaxial, close-ended, bulletized design, and has an efficiency rating of $\epsilon=99\%$ for the 1.333 MeV gamma ray from the decay of ^{60}Co , relative to a 3 X 3 inch sodium iodide crystal. The crystal is mildly n-type and is designed to be operated with a negative bias of 4000 volts applied to the center electrode.

The first preamplification stage of the detector signal is directly adjacent to the crystal within the cold section to keep noise low and reduce capacitance in the cabling. Subsequent sections of the preamplifier are outside the cryostat along with a high voltage conditioner circuit, in a coaxial geometry around the cold finger.

4.1.2.2 Counting cave

The detector is suspended from a bridge that is damped to reduce its transmission of vibrations. Rope and chain are used to support the detector to further minimize any microphonic pickup. The detector is suspended in a cave made of low gamma-ray emission lead bricks shown in Figure 4-6. The lead cave is 10 cm thick on the bottom and all sides, but is open at the top. A piece of 2 cm thick stiff polystyrene foam is attached to the floor of the cave. It has cutouts to snugly accept the lower ends of both the detector assembly and a sample bottle, to ensure repeatable positioning. A mark on the outside of the sample bottle (which was facing the neutron source in the irradiation phase) must be positioned facing the detector, to ensure consistency in the experiments. This is accomplished by aligning the mark on the bottle with a similar mark on the foam. The detector assembly and its cutout in the foam are also marked for consistent alignment.

Seven acquisition gates are used for acquiring the germanium spectra, with a dead period of about 3 seconds between each, and ten millisecond resolution on starting and stopping times. Details of the signal electronics and the analog-to-digital conversion are included in Appendix C.

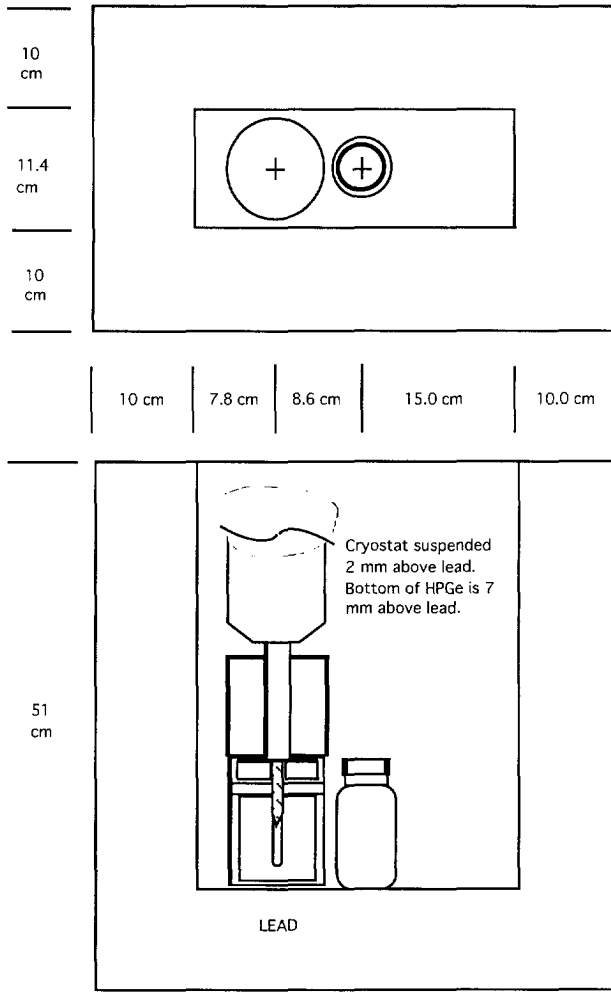


Figure 4-6 Plan and cross section views of the counting facility. The detector assembly is suspended by a rope to minimize any microphonic pickup. A 2 cm thick piece of stiff polystyrene foam (not shown), with cutouts for the detector and sample bottle, lies on the floor of the lead cave, permitting good repeatability of detector and sample placement.

4.1.2.3 Data acquisition computer

Data acquisition is controlled from a VMS-based VAXStation loaded with Canberra/Nuclear Data Corp. acquisition software. The computer is host, via ethernet, to a pair of acquisition interface modules whose functions are the routing of data from A-to-D converters and multichannel scalers to the host. The system is designed so that system-level commands can control configurations and acquisition.

4.2 Energy efficiency of the germanium detector

The energies and relative intensities of 17 gamma rays emitted by radium in equilibrium with its daughters have been tabulated [52-55, 28]. The energies span a large range, from 186 keV to 2448 keV, and are often and conveniently used for determining the change in detector efficiency with energy.

Another 15 gamma rays in known relative intensity, with energies from 368 keV to 3661 keV, are provided by ^{44}K , which decays with a 22 minute half life. It is considerably less convenient than radium, since it must be prepared by placing calcium in a hard neutron flux. An (n,p) reaction on ^{44}Ca , with isotopic abundance of only about 2 percent, results in the production of ^{44}K , and several other nuclides. However, the peak areas are easily measurable, so this source may be used to extend the energy efficiency curve to higher energies than can be obtained by simply using radium.

Both gamma-ray sources were used to establish the full-energy peak efficiency of the large germanium detector. A sample bottle containing 150 grams of calcite was irradiated in the water tank for about thirty minutes. Spectra were acquired separately with the two sources, which were placed 5 cm distant from the side of the detector package. Peak areas obtained from the two runs are divided by the precisely known relative intensities and plotted against

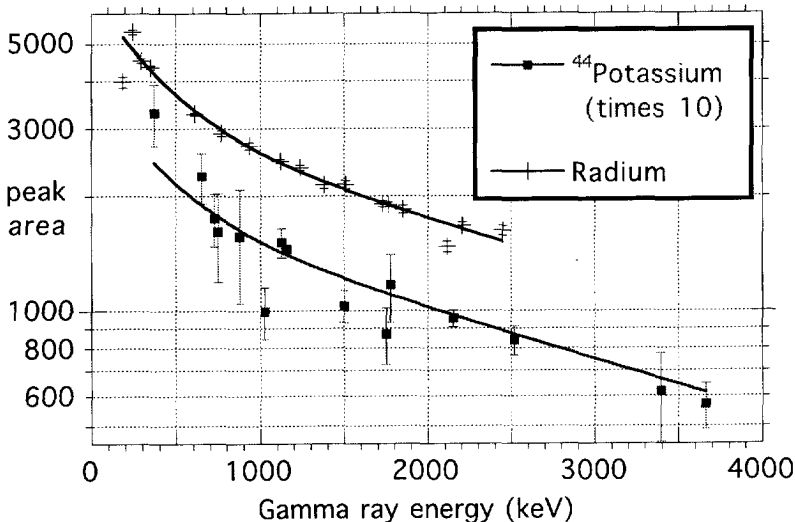


Figure 4-7 Measured peak areas are divided by known relative intensities and plotted for each of two gamma-ray sources. A simultaneous fit to both sets of data in this plot results in the efficiency relation shown in equation 4-1.

the gamma ray energies in Figure 4-7. A two-exponential curve [28,56,57] was fitted to both sets of points simultaneously, using a normalization factor for the two sets of data as an additional parameter, with the following result.

$$\text{Efficiency} \propto e^{-0.00269 E\gamma} + 0.875 e^{-0.000304 E\gamma} \quad 4-1$$

Results of fitting the two sets of data separately and together are presented in Table 4-1. All three fits were done using the uncertainties as weights, so it is not surprising that the composite fit lies closer to the radium fit. The fit to composite data, in combination with the uncertainties represented by error bars in Figure 4-7, explains 97% of the variation in the data.

Table 4-1 $\text{Efficiency} \propto e^{-aE\gamma} + b e^{-cE\gamma}$				
	a	b	c	R ²
Radium	0.0026	0.830	0.00029	0.98
⁴⁴ K	0.0037	0.364	0.00035	0.94
Together	0.0027	0.875	0.00030	0.97

This technique can be useful in extending an assessment of energy efficiency up to 3.7 MeV. The technique can easily be improved by irradiating a larger mass of calcium, by irradiating it longer until the activity approaches saturation, or by increasing the neutron generator output so that more events and better precision may be obtained.

4.3 Summary

The irradiation facility will provide samples with exposure to a neutron flux with a continuous energy distribution, similar to what would pertain in a borehole environment. Evaluation of the activation cross section response integrals in the facility will thus have significance in establishing the response of a sonde.

Neutron detectors contained in the facility have been shown to be insensitive to the sample, and are used to monitor thermal, epithermal, and MeV regions of the flux. They are configured to acquire a history of the flux throughout the irradiation, to monitor the slowly changing output of the neutron generator. The absolute output rate of the neutron generator has been calibrated to the count rates of the neutron monitors.

Comparison of peak areas detected with large ($\epsilon_{3X3} = 99\%$) and small ($\epsilon_{3X3} = 33\%$) HPGc detectors shows that the gains in photopeak efficiency from

using a large detector are more substantial than the ratio of 1333 keV efficiencies alone predicts. The gains are especially significant for gamma rays with higher energies.

A method has been developed to extend the efficiency calibration of a germanium spectrometer to higher energies than may be obtained with a radium source. A fast neutron source is used to take advantage of the reaction $^{44}\text{Ca}(n,p)^{44}\text{K}$ which results in the production of 15 gamma rays with known branching ratios and a 22 minute half life. The decaying ^{44}K may be used to obtain an efficiency calibration extending to 3.7 MeV.

This chapter describes the specific procedures used in performing the experiments and analyzing the data. Examples of the data obtained in both the irradiation and counting portions of the experiments are presented.

5.1 Calculation of the effective source strength

Procedures for this set of experiments differ from normal thermal neutron activation analysis, with respect to the monitoring of the neutron flux. Detectors that enable the flux intensity to be recorded at regular periodic intervals throughout the irradiation time are used rather than activation foils. This is necessary because the source strength can vary substantially during the irradiation time.

For eventual comparison to modeling results, the neutron monitors are used to calculate an effective source strength S_0 at time t_0 , the instant the accelerator is switched off at the end of irradiation. The effective source strength is dependent on the decay constant τ and the instantaneous source strength s which varies with time. It may be considered as the effective number of neutrons, all dispensed at t_0 , that has the same effect as the total irradiation history.

$$S_0 = \int_{t=0}^{t_0} s \left[e^{-(t-t_0)/\tau} \right] dt \quad 5-1$$

Typical histories as seen by the three neutron monitors are shown in Figure 5-1. It is always arranged so that irradiation begins part way through the first time bin of the recorded monitor responses, and t_0 occurs part way through the final time bin. The position of this instant in time t_0 is determined by taking the ratio of thermal detector events in the final time bin to the average of the previous few bins, and assuming that the neutron output is constant over this interval. The *statistical* error in this process is small, amounting to a few milliseconds uncertainty in the position of t_0 . Rapid fluctuations in the accelerator output would have a deleterious systematic effect upon the derived t_0 , but are unlikely. Where C is the number of recorded events in a bin, the bin width w of the last bin z can be calculated, as follows.

$$w_z = \frac{nC_z}{\sum_{i=z-n}^{z-1} C_i} \quad 5-2$$

Estimates of the effective source strength are made from each of the three recorded monitor histories. The half life (or decay constant = τ) of the nuclide in question must be considered when calculating the effective source strength, because monitor reading C for some bin i at earlier time t has diminished exponentially, leaving a reduced contribution at t_0 .

$$C_{i(\text{eff})} = C_i e^{-t_{i(\text{eff})}/\tau} \quad 5-3$$

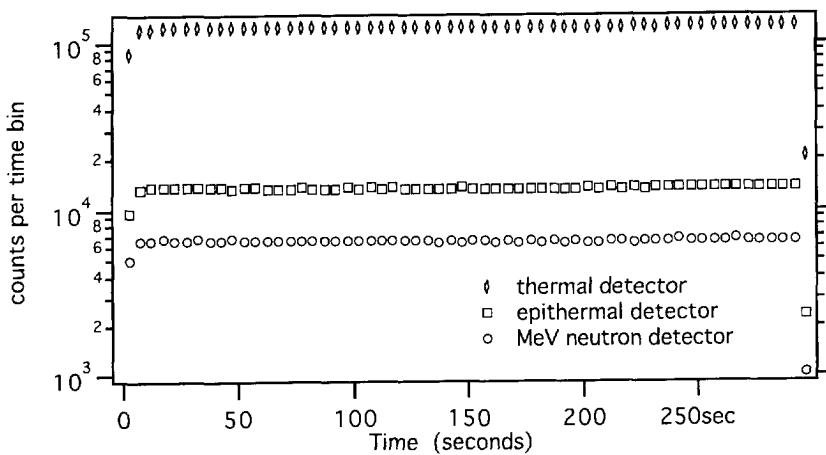


Figure 5-1 The detector history for a five minute irradiation, using five second binning, shows that the accelerator was turned on near the beginning of the first five second bin, turned off near the beginning of the final five second bin, and that there were only minor fluctuations in the neutron output rate.

Also, the position of t for each bin i is the *effective* centroid of the bin for the particular τ of concern, most conveniently calculated from the beginning of the bin.

$$t_{i(\text{eff})} = t_{i(\text{begin})} - \tau \ln \left[\left(e^{-w_i/\tau} + 1 \right) / 2 \right] \quad 5-4$$

A plot of the effective bin contributions for one of the experimental runs is presented in Figure 5-2, incorporating the shifting of t_0 , the calculation of

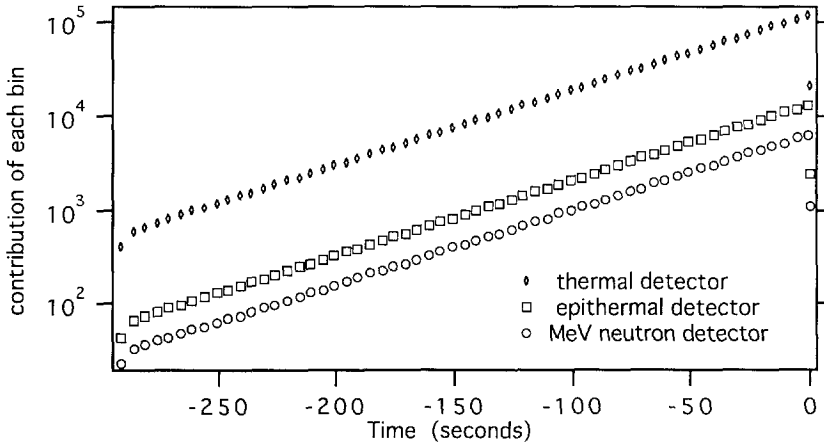


Figure 5-2 The contribution of each bin's measure of neutron flux toward an effective instantaneous burst of neutrons at time t_0 is displayed. This plot is for the data in Figure 5-1, for a 60 second half-life nuclide. The summation of each curve is the effective source strength, in monitor units.

effective bin positions from the centroids, and the decay. At this point, the effective source strength S_0 at t_0 for each of the monitors is calculated by summing the bin contributions $C_{i(eff)}$, which are the source strengths for each bin that have been reduced by the exponential decay.

$$S_0 = \sum C_{i(eff)} \quad 5-5$$

Next, the calibration factor obtained previously for the neutron monitor is incorporated so that the effective source strength is stated in number of neutrons rather than monitor counts.

5.2 The sample transfer procedure

The duration of the irradiation phase data acquisition is fixed and monitored by the host computer, as is the delay time during sample transfer, and the opening and closing of the various gates for recording of the decay spectra. Currently, however, there is no capability of the host computer to control the accelerator, so this must be done manually. The acquisition and control program in the computer announces that time is getting short and then informs the experimenter that the final time bin for data acquisition has been entered and it is time to shut off the accelerator. The operator must anticipate this event

and accomplish the shutdown before the time bin expires, usually a matter of five seconds, otherwise the actual position of t_0 cannot be calculated.

After the expiration of the final time bin, the computer waits a fixed period and begins spectral acquisition with the germanium detector. To obtain meaningful data in the first spectral acquisition gate, the sample must be in place before the computer beeps to inform the operator that acquisition has begun. Two different fixed periods were used. A 10 second period was used when an assistant was available to perform one of the transfer functions. A 20 second period was used when experiments were done in the middle of the night, and the experimenter was not only tired, but had to turn off the accelerator *and* retrieve the sample because it was past the bedtime of the ten-years-old lab assistant.

An override can be placed on the fixed delay period if required by the experimenter for nuclides with short half-lives so that a single keystroke will begin acquisition. Times for transfer and onset of spectral acquisition just under six seconds after accelerator shutdown have been accomplished using this method.

5.3 Analysis of germanium spectra

Steps in analysis of the spectra are listed below. The discussion following the list describes how each of the steps is accomplished.

- 1 Find peak areas and centroids as acquisition ends
- 2 Inspect raw data and fitted peaks
- 3 Handle special peak-fitting cases, if any
- 4 Identify peaks (decaying nuclide and gamma ray energy)
- 5 Refine energy calibration
- 6 Apply dead time correction to peak areas
- 7 Apply pileup correction to peak areas

For each peak energy and inferred decay time constant:

- 8 Calculate effective center of acquisition gates
- 9 Fit a decay curve to the peak areas
- 10 Evaluate the data quality
- 11 Find the total area under the decay curve
- 12 Compare to modeling results

An example of the pulse height spectra from an experiment is presented in Figure 5-3. The spectra in this example are fairly simple, and their analysis is straightforward. First, a computer code scans each spectrum, searches for peaks, and calculates their areas, centroids, and resolutions, while attempting to impose a Gaussian fit upon the peaks. If the fit is poor, the code may propose that there are two or more peaks partially superimposed, and attempt to resolve them by fitting multiple Gaussian shapes.

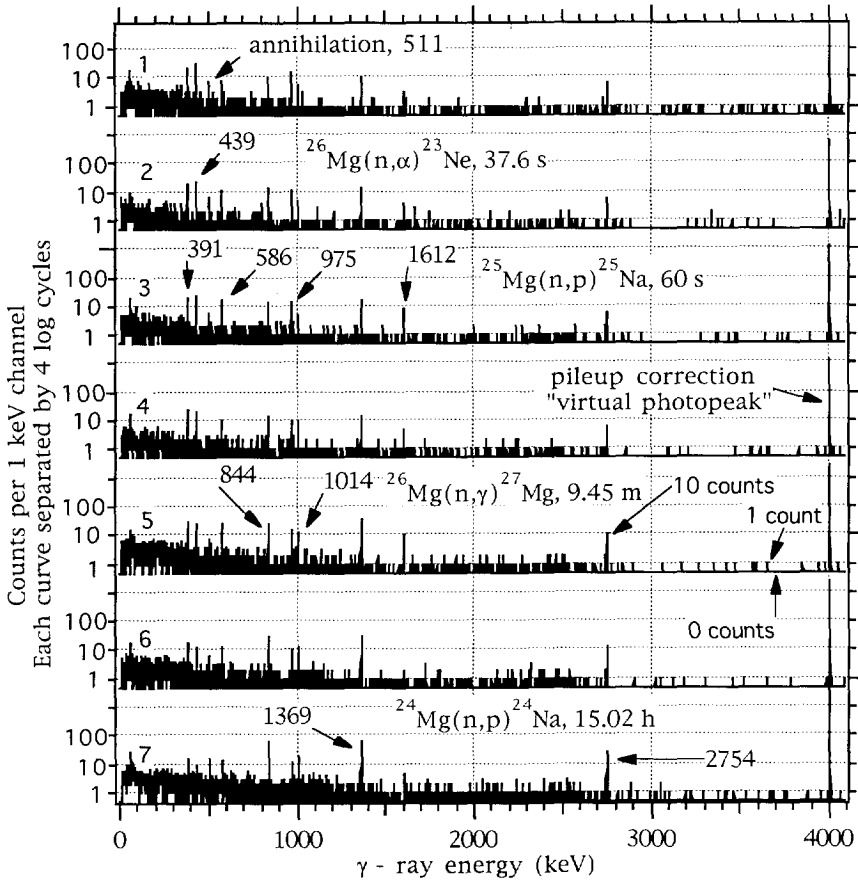


Figure 5-3 An example of the measured pulse height spectra from a sample of 132 grams of magnesium oxide powder, after 5 minutes irradiation at approximately 1.35×10^8 neutrons per second. Spectra 1 through 7 are acquired during consecutive counting periods of 10, 10, 20, 20, 40, 40, and 80 seconds duration. Identified peaks are labeled in groups corresponding to their source nuclide.

Three different computer codes for peak area determination are used at times, though for the series of data shown in the Figure a sophisticated program is not required because of the low continuum level and lack of overlapping peaks. The PEAK routines [74] on the data acquisition computer are used for initial processing of all the spectra, and are sufficient in most cases. After running PEAK, all data from an experiment is shipped to another computer for subsequent analysis, and to free the acquisition computer for further accumulations. The spectra are then plotted for visual inspection of the identified peaks, which may identify overlapping peaks missed by the code, or poorly shaped peaks. If so, a modified version of the PEAKFIND [72] code can be used to resolve them. The GANYMEDE [73] code can also handle overlapping peaks, and is useful for peaks that may not be strictly Gaussian in shape.

An expanded view of the pulse height spectra from Figure 5-3 is contained in Figure 5-4, centered around the 439 keV photopeak resulting from the $^{26}\text{Mg}(n,\alpha)^{23}\text{Ne}$ reaction and subsequent decay with 37.6 second half-life. Peak areas as determined by the PEAK routine are indicated on the figure.

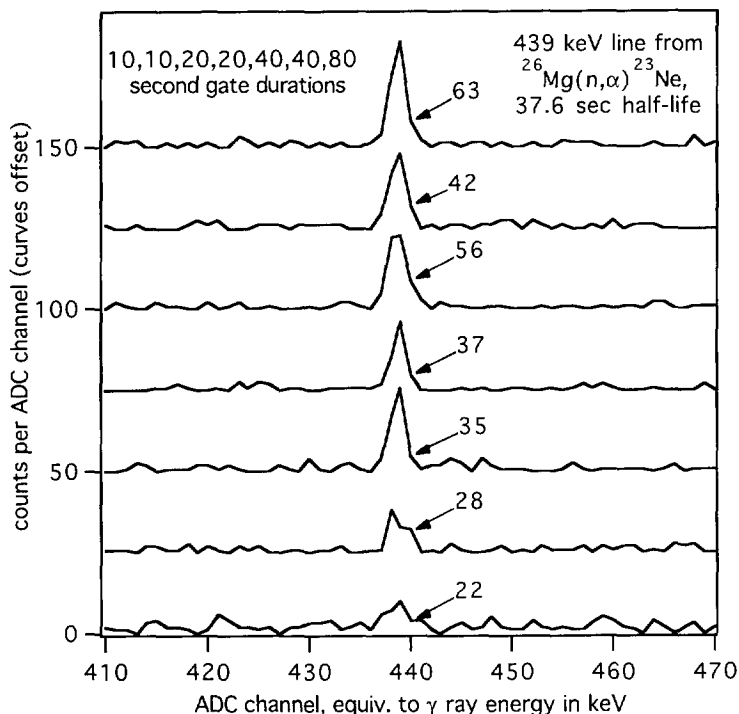


Figure 5-4. Numbers adjacent to the peaks are areas in this expanded view of data from Figure 5-3.

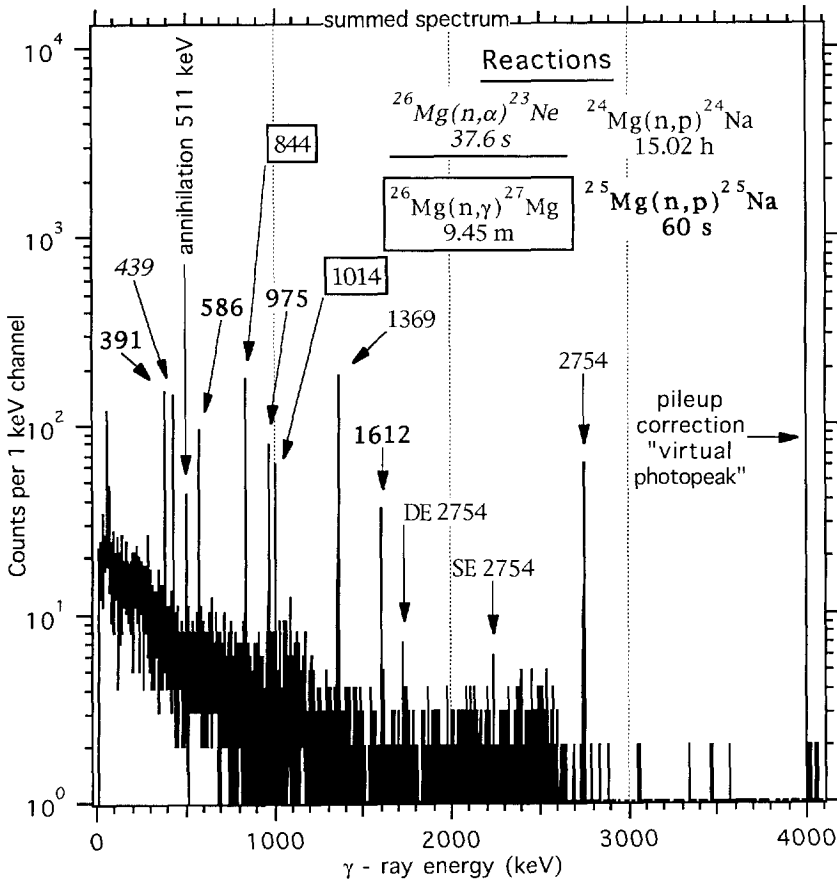


Figure 5-5 Some features of the pulse height spectra become more prominent when the spectra are summed, particularly small peaks atop a continuum, such as the escape "peaks" from the 2754 keV gamma ray. Generally, summing will enhance the peaks and improve precision when the decay time constant is long compared to the gate widths. Faster decay constants will suffer from summing because only noise will be added from later gates.

The next step in analysis is identification of the peaks in terms of their energy and the decaying nuclides. A fairly accurate first approximation to the energy calibration (1 keV per ADC channel) is used in recording the data, making this step less difficult. A list of expected nuclides and their associated gamma ray energies is compared to energies estimated for the peaks in the data, and a refined energy calibration is performed, using gain, offset, and nonlinear term if required.

The single and double escape peaks from the 2754 keV gamma ray in Figure 5-3 are not readily apparent in the individual plots. When the seven spectra are summed, as in Figure 5-5, these features are enhanced, and can be identified.

Dead time corrections to the peak areas are performed using the ratio of real time to live time provided in the data acquisition program. Dead times are small, less than 5%, except in the first acquisition gates of a few measurements. The corrections are performed as if the dead time is constant across the gate, which is a reasonable approximation except in cases where the decay time constant is small compared to the gate width. Pulse pileup, which is also less than 5% in all cases, is measured by injecting pulses at a constant known rate (100 Hz) into the preamplifier and comparing this rate with the rate that they appear in a "virtual photopeak" in the pulse height spectrum. The amplitude of the pulses is set so that they appear in channel 4000 of the pulse height spectrum. A periodic pulser is used so that the number of injected pulses in an acquisition gate is known to ± 1 pulse. Then, the fractional precision for measuring 5% pileup in a 10-second gate is $1/\sqrt{5\% \times 10 \times 100}$ or about one part in seven, an acceptable level of precision for this small correction. The pileup correction factor for this case would be 1.053 ± 0.007 .

For each decaying gamma ray of interest in an acquisition gate over which counts are integrated, the effective time position of the gate will depend on the time constant τ in the manner described by Equation 5-4. Vectors representing the effective centroids of the gates are constructed and the photopeak count rates are plotted against these times, as in Figure 5-6. Then a weighted fit of a simple exponential decay with fixed τ is imposed on the data to determine the total area under the curve. Quality of the data is checked by including the value of τ as a fitting parameter and looking for gross departures in the derived value for area. If the time constant is permitted to be a fitting parameter in this example, the decay constant only changes by +3.1% while χ^2 of the fit improves by less than 2%. Area under the curve changes by 0.6%. Thus there is good confidence that the data are not contaminated by an interfering gamma ray or other systematic error. The ability to verify the validity of data by a half-life analysis is an advantage of acquiring several spectral gates. The advantage is offset somewhat by an accompanying loss in statistical precision. In the example of Figure 5-6, summing the gates before determining the peak area results in an estimate of $468.3 \pm 6.5\%$ for the area under the decay, a slight improvement in precision. The improvement from summing will be greater when the continuum under a peak is larger.

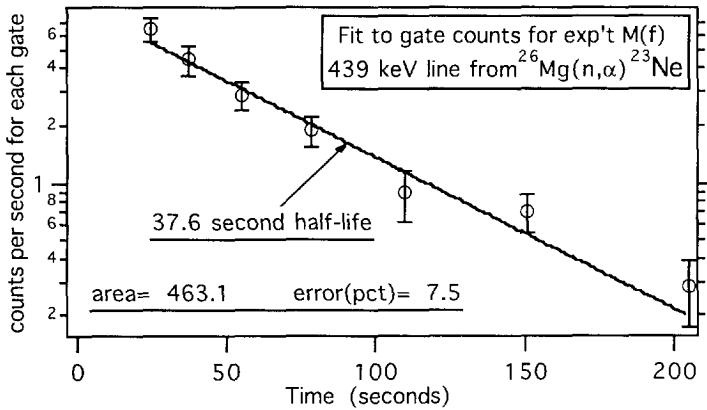


Figure 5-6 Results of the fit are stated in total counts from shutdown t_0 to $t = \infty$. The half-life was not a fitting parameter for this fit.

The area under the curve represents the total signal resulting from an instantaneous blast of S_0 neutrons at t_0 . For comparison to modeling results, the area per source neutron will be used.

$$Response = area/S_0$$

5-6

5.4 Summary

Methods have been developed to determine the position of the source shutdown relative to the data acquisition timing sequence. This permits the determination of an effective source strength at shutdown, for any half life desired, using the neutron monitor histories.

The data reduction sequence for gamma-ray spectra has been configured to use summed spectra or combinations of individual spectra. Experimental results are stated in terms of total detected activity from the time of source shutdown until infinite time. The total detected activity is normalized by the effective source strength at shutdown.

Chapter 6 Experimental Results for Mg, Na, Al, and Si

There are two purposes for this series of measurements. First, the establishment of responses to the elements will provide a basis for comparison to the modeling results, resulting in an assessment of the accuracy of cross section response integrals, for the reactions listed in Table 1-2. Also, the sensitivities established here will provide a *forward response matrix* for the reactions to be used as a basis for assessing a least-squares approach to activation analysis. In the discussion of different data reduction techniques for gamma-ray spectroscopy in chapter 2, it was illustrated that a weighted least-squares approach in an overdetermined system can have significant statistical advantages over direct solutions. Earlier approaches to borehole activation analysis using scintillators have not taken advantage of these methods because the poor energy resolution has not permitted it. Small ($\epsilon < 20\%$) germanium spectrometers have not been able to utilize this approach either because of low counting rates and poor photofactors.

Several sets of experiments related to magnesium, sodium, aluminum, and silicon were performed using two different timing schemes, listed in table 6-1.

Series name	Nominal irradiation time (seconds)	Bin width of neutron monitor (seconds)	Durations of spectral acquisition gates (seconds)
A, B, C, D	3600	15	200,200,400,400,800,800,1600
E, F, G, H	300	5	10,10,20,20,40,40,80

Table 6-1 Two timing schemes used for the experiments. Transfer times are about twenty seconds and dead times between gates are approximately three seconds.

Results are stated as C_{exp} for each full-energy photopeak observable in the experiments, as follows.

$$C_{\text{exp.}} = \frac{\text{photopeak area from time } t_0 \text{ to } t_{\infty}}{\left(\text{gram of element} \right) \left(\text{effective source neutron at } t_0 \right)} \quad 6-1$$

The assumption is made in the calculation of C_{exp} that the isotopic content of the materials is not substantially different than the average values in the literature. Any degree of isotopic fractionation which is found in the sample materials or is caused by the manufacturing process will be significantly below the level observable by the measurements [58].

Results of the experiments are listed in tables 6-2 through 6-8 and tables 6-10 through 6-15. Entries in the table are followed by their uncertainties, expressed in percent. The uncertainties listed for individual measurements are based only on the counting statistics from both the irradiation and decay parts of the experiments. Uncertainties given for average values are due to the quadrature combination of counting statistics and the scatter observed between different measurements. For repeated measurements with substantial scatter, uncertainty of the average value may be greater than that of the individual value.

6.1 Magnesium, Sample M (132 g magnesium oxide)

An example of raw spectral data from this sample appears in figure 6-1. A week was allowed to elapse between runs to accommodate the 15 hour half life of ^{24}Na , except for runs E and F, which were run on consecutive days. The subtraction of remnant run E activity from the run F peak areas is reflected in the larger uncertainties reported for run F for this nuclide. Results are presented in Tables 6-2 through 6-5.

For the timing scheme used, the largest magnesium signal is from the decay of ^{27}Mg , made by the thermal reaction on ^{26}Mg . In a logging measurement, the four gamma rays resulting from the $^{25}\text{Mg}(n,p)^{25}\text{Na}$ reaction are likely to become more prominent because of their convenient half-life and the lack of a competing reaction. Surprisingly, all four gamma rays do not have likely competitors for their position on the pulse height spectrum. On a gram-for-gram basis, magnesium will obtain a slightly larger signal than aluminum from reactions leading to the intermediate nuclide ^{24}Na , but only about 40% of the signal obtained by sodium.

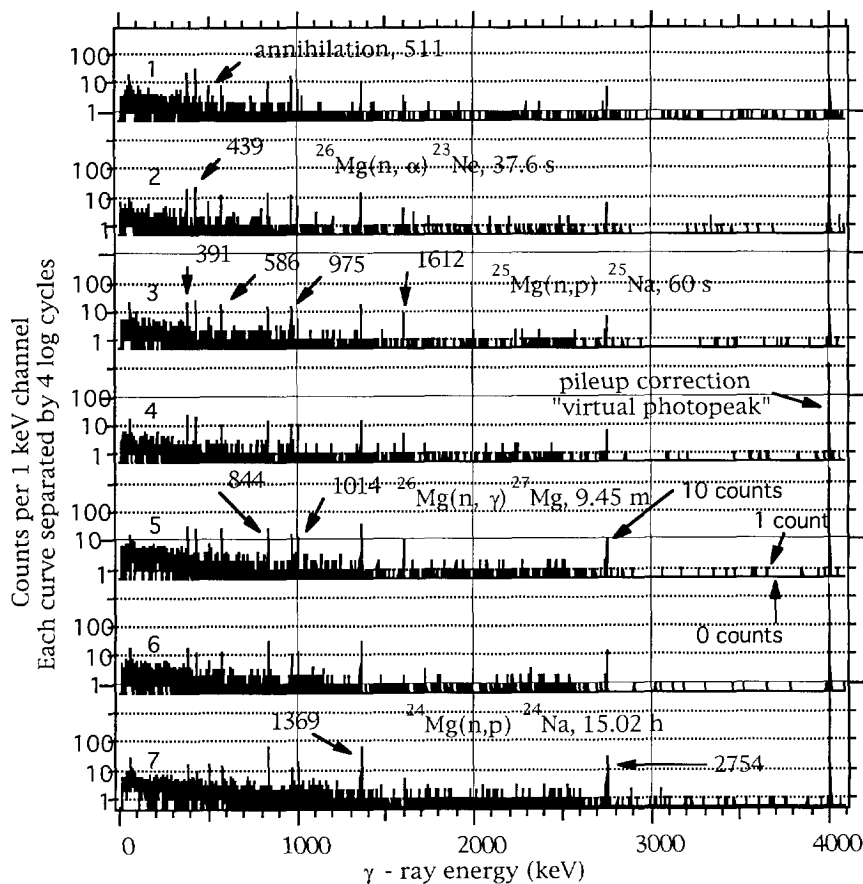


Figure 6-1 (identical to figure 5-3) An example of the measured pulse height spectra from a sample of 132 grams of magnesium oxide powder, after 5 minutes irradiation at approximately 1.35×10^8 neutrons per second. Spectra 1 through 7 are acquired during consecutive counting periods of 10, 10, 20, 20, 40, 40, and 80 seconds duration. Identified peaks are labeled in groups corresponding to their source nuclide.

Table 6-2 $C_{\text{exp}} (\times 10^9)$ for reaction $^{26}\text{Mg}(n, \gamma)^{27}\text{Mg}$, $t_{1/2} = 9.45\text{m}$		
Exp.	$C_{\text{exp}} (\times 10^9)$ for 843.8 keV	$C_{\text{exp}} (\times 10^9)$ for 1014.4 keV
E	0.718 6%	0.292 8%
F	0.694 5%	0.260 10%
G	0.727 5%	0.264 9%
H	0.671 5%	0.258 9%
AVG	0.702 4%	0.269 8%

Exp.	$C_{\text{exp}}(\times 10^9)$ for 390.7 keV	$C_{\text{exp}}(\times 10^9)$ for 585.9 keV	$C_{\text{exp}}(\times 10^9)$ for 975.2 keV	$C_{\text{exp}}(\times 10^9)$ for 1611.9 keV
E	0.442 8%	0.307 10%	0.286 9%	0.159 13%
F	0.467 8%	0.307 10%	0.337 8%	0.168 13%
G	0.428 7%	0.316 9%	0.294 9%	0.158 14%
H	0.452 7%	0.314 8%	0.285 8%	0.146 11%
AVG	0.447 5%	0.311 5%	0.301 9%	0.158 9%

Exp.	$C_{\text{exp}}(\times 10^9)$ for 1368.6 keV	$C_{\text{exp}}(\times 10^9)$ for 2754.1 keV
E	30.6 7%	24.1 8%
F	34.8 9%	18.6 10%
G	28.8 8%	21.2 8%
H	31.4 6%	20.0 7%
AVG	31.4 9%	21.0 12%

Exp.	$C_{\text{exp}}(\times 10^9)$ for 439 keV
E	0.739 8%
F	0.782 8%
G	0.969 5%
H	0.861 6%
AVG	0.838 13%

6.2 Sodium, Sample L (332 g sodium carbonate)

Raw results for sodium are presented in Tables 6-6 through 6-8. The 1633 and 439 keV gamma rays provide signals suited to the irradiation and collection times used in the experiments and to those anticipated in a borehole measurement (figure 6-2). The only reaction leading to the 1633 keV gamma ray is $^{23}\text{Na}(n,\alpha)^{20}\text{F}$, except for the insignificant $^{19}\text{F}(n,\gamma)^{20}\text{F}$ reaction, and there are no other gamma rays likely to cause spectral interference. The 439 keV gamma ray line is eight times more intense for sodium than it is for magnesium, on a gram-for-gram basis. The potential for spectral interference exists if the germanium crystal itself becomes activated. Sodium also has the largest effective cross section for the production of ^{24}Na .

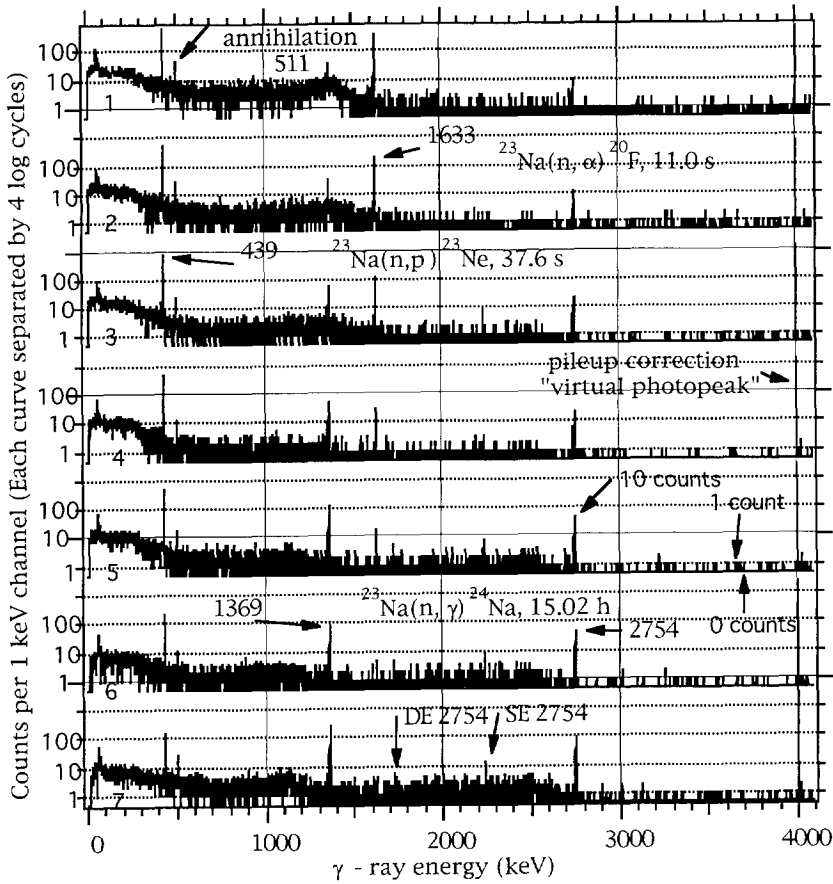


Figure 6-2 An example of the data from five minute irradiation of a sodium carbonate sample. Spectra are for 10, 10, 20, 20, 40, 40, and 80 seconds of acquisition.

Table 6-6 $C_{exp} (\times 10^9)$ for reaction $^{23}\text{Na}(n,\gamma)^{24}\text{Na}$, $t_{1/2} = 15.02\text{h}$				
Exp.	$C_{exp} (\times 10^9)$ for 1368.6 keV		$C_{exp} (\times 10^9)$ for 2754.1 keV	
E	82.5	3%	45.4	4%
F	76.4	4%	48.5	5%
G	76.8	3%	45.0	4%
H	79.2	3%	43.6	4%
AVG	78.7	4%	45.6	5%

Exp.	$C_{exp}(\times 10^9)$ for 1633.1 keV	
E	22.2	3%
F	22.5	3%
G	22.2	3%
H	21.4	3%
AVG	22.1	3%

Exp.	$C_{exp}(\times 10^9)$ for 439 keV	
E	7.36	2%
F	7.29	2%
G	7.04	2%
H	6.97	2%
AVG	7.16	3%

6.3 Aluminum, Sample I (349 g aluminum oxide)

A sample of data is presented in Figure 6-3, and results of the measurements on aluminum samples are reported in Tables 6-10 through 6-12. For the five minute irradiations and counting during the first four minutes of decay the best indicator of aluminum is the thermal reaction leading to the intermediate nuclide ^{28}Al . However, the signal from silicon is 40% larger on a gram-for-gram basis. There are no unique gamma rays from activation of aluminum, however the effective cross section in this mixed flux for production of ^{27}Mg from aluminum is 20 times higher than for magnesium, and 45 times higher than for silicon, on a per-gram basis. The expected relative sizes of signals from rocks containing aluminum and silicon have been calculated, and are shown in Table 6-9. The 1778 keV peak is dominated by silicon regardless of the aluminum content. The 844 and 1014 keV peaks are dominated by aluminum unless the aluminum content is extremely low.

	Al/Si concentrations	Al/Si 1778 keV signal from ^{28}Al	Al/Si 844 & 1014 keV signal from ^{27}Mg
Herron shale	0.34	0.13	8.1
Arkosic sandstone	0.18	0.24	15
Shaly sand	0.12	0.09	5.4

Table 6-9 Expected relative sizes of gamma ray photopeak counts from aluminum and silicon. Compositions of the rocks were provided by Susan Herron, and are listed in Appendix B

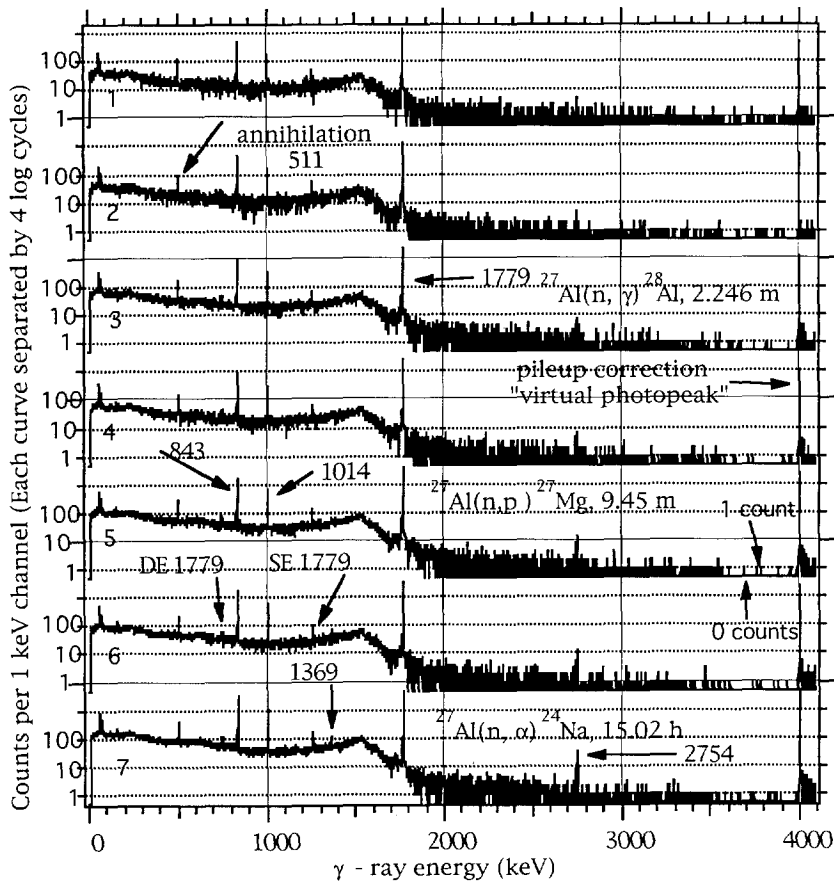


Figure 6-3 An example of the data from five minute irradiation of an aluminum oxide sample. Spectra are for 10, 10, 20, 20, 40, 40, and 80 seconds of acquisition.

Table 6-10 $C_{\text{exp}} (\times 10^9)$ for reaction $^{27}\text{Al}(n, \alpha)^{24}\text{Na}$, $t_{1/2} = 15.02\text{h}$

Exp.	$C_{\text{exp}} (\times 10^9)$ for 1368.6 keV	$C_{\text{exp}} (\times 10^9)$ for 2754.1 keV
D	24.8 0.4%	14.7 0.5%
G	22.7 5%	13.3 6%
H	22.5 5%	12.3 6%
AVG	23.3 6%	13.4 9%

Table 6-11 $C_{\text{exp}} (\times 10^9)$ for reaction $^{27}\text{Al}(n, p)^{27}\text{Mg}$, $t_{1/2} = 9.45\text{m}$

Exp.	$C_{\text{exp}} (\times 10^9)$ for 843.8 keV	$C_{\text{exp}} (\times 10^9)$ for 1014.4 keV
D	14.7 0.3%	5.15 0.5%
G	14.3 1%	4.88 2%
H	14.2 1%	5.05 2%
AVG	14.4 2%	5.03 3%

Table 6-12 $C_{exp}(\times 10^9)$ for reaction $^{27}\text{Al}(n,\gamma)^{28}\text{Al}$, $t_{1/2} = 2.246m$		
Exp.	$C_{exp}(\times 10^9)$ for 1778.8 keV	
D	23.3	0.6%
G	25.8	0.8%
H	26.2	0.8%
AVG	25.1	6%

6.4 Silicon, Sample G (407 g silicon dioxide)

The best indicator of silicon in these timing schemes, or in any likely borehole scheme, is the 1779 keV gamma ray from the decay of ^{28}Al (see figure 6-4). The 1273 keV gamma ray from the $^{29}\text{Si}(n,p)^{29}\text{Al}$ reaction is unique to silicon, but will suffer statistically because of its partially coincident position with the single escape peak from the prominent 1779 keV gamma ray (see figure 6-5). The higher energy gamma rays from this same decaying nuclide are useless for further consideration because of their small branching ratios. Results for silicon measurements are presented in Tables 6-13 through 6-15.

Table 6-13 $C_{exp}(\times 10^9)$ for reaction $^{28}\text{Si}(n,p)^{28}\text{Al}$, $t_{1/2} = 2.246m$		
Exp.	Gamma ray energies (keV) & branching ratios (%)	
	1778.8(100)	
B	31.9	0.5%
C	34.0	0.5%
D	32.9	0.5%
G	37.7	0.8%
H	38.6	0.8%
AVG	35.0	8%

Table 6-14 $C_{exp}(\times 10^9)$ for reaction $^{30}\text{Si}(n,\alpha)^{27}\text{Mg}$, $t_{1/2} = 9.45m$			
Exp.	Gamma ray energies (keV) & branching ratios (%)		
	843.8(72)		1014.4(28)
B	0.290	2%	0.101 4%
C	0.329	2%	0.109 4%
D	0.330	2%	0.119 4%
G	0.387	15%	
H	0.311	15%	
AVG	0.329	12%	0.110 9%

Exp.	Gamma ray energies (keV) & branching ratios (%)		
	1273(91)	2028(3.4)	2426(5.5)
B	0.911 1%	0.033 7%	0.039 6%
C	1.040 1%	0.028 9%	0.044 6%
D	0.984 1%	0.032 8%	0.042 6%
G	1.036 6%		
H	0.958 6%		
AVG	0.986 6%	0.031 10%	0.042 7%

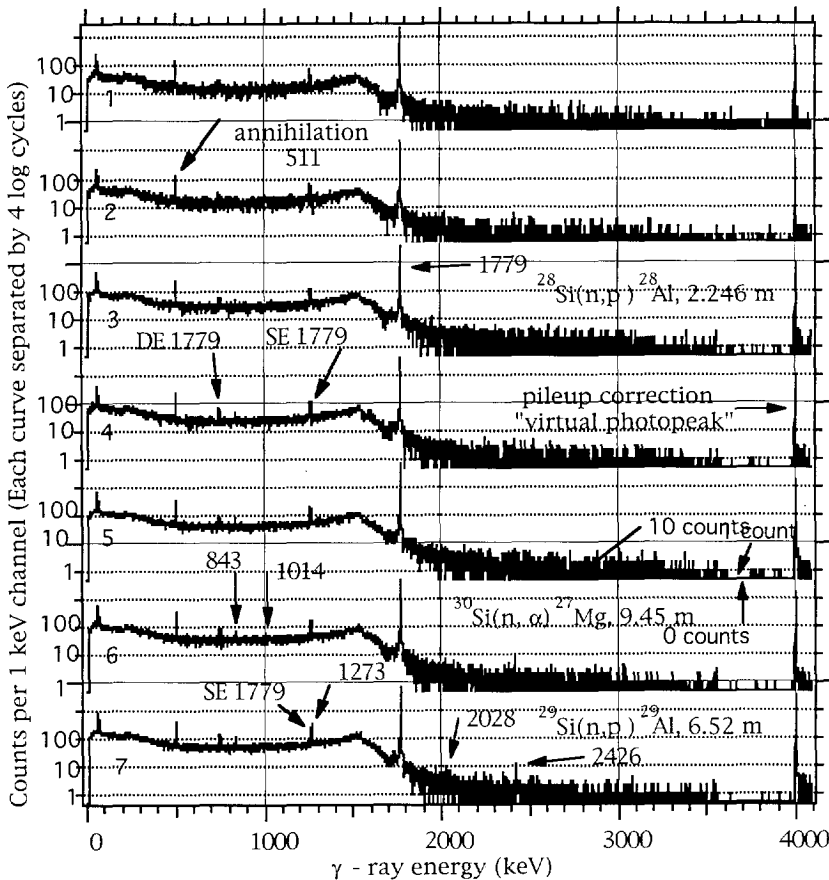


Figure 6-4 An example of the data from five minute irradiation of a silica sample. Spectra are for 10, 10, 20, 20, 40, 40, and 80 seconds of acquisition. The 1779 keV peak is the largest signal in the spectra, by far.

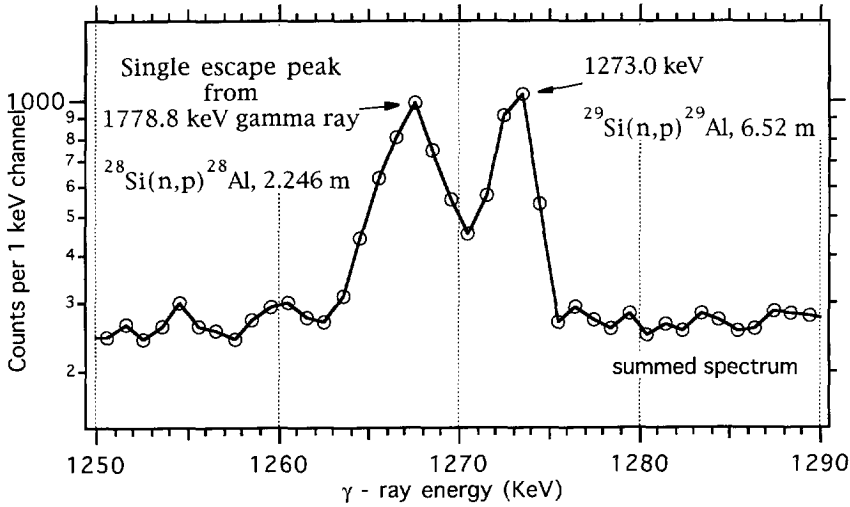


Figure 6-5 Interfering peaks seen in the previous figure are expanded in this figure. The spectra are summed before attempting to resolve this pair.

6.5 Response matrix

A response matrix may now be constructed from the average values for sensitivity compiled in the previous sections (Tables 6-2 through 6-8 and Tables 6-10 through 6-15), ignoring any differences between the samples with regard to neutron and gamma-ray sample effects. The signals from the 2028 keV and 2426 keV gamma rays from the $^{29}\text{Si}(n,p)^{29}\text{Al}$ and subsequent decay are too weak to be of any value and are left out of the matrix. The response matrix will then be a sparse 12 X 4 matrix relating mass of the elements in grams M to the photopeak counts C per effective source neutron, as in equation 6-2. Bold typeface in the equation indicates a thermal neutron activation response.

$$\begin{bmatrix} C_{1369} \\ C_{2754} \\ C_{844} \\ C_{1014} \\ C_{439} \\ C_{391} \\ C_{586} \\ C_{975} \\ C_{1611} \\ C_{1633} \\ C_{1779} \\ C_{1273} \end{bmatrix} = \begin{bmatrix} 31.4 & \mathbf{78.7} & 23.3 & 0 \\ 21.0 & \mathbf{45.6} & 13.4 & 0 \\ \mathbf{0.702} & 0 & 14.4 & 0.329 \\ \mathbf{0.269} & 0 & 5.03 & 0.110 \\ 0.838 & 7.16 & 0 & 0 \\ 0.447 & 0 & 0 & 0 \\ 0.311 & 0 & 0 & 0 \\ 0.301 & 0 & 0 & 0 \\ 0.158 & 0 & 0 & 0 \\ 0 & 22.1 & 0 & 0 \\ 0 & 0 & \mathbf{25.1} & 35.0 \\ 0 & 0 & 0 & 0.986 \end{bmatrix} \times 10^{-9} \begin{bmatrix} M_{Mg} \\ M_{Na} \\ M_{Al} \\ M_{Si} \end{bmatrix} \quad 6-2$$

Chapter 7 Monte Carlo Modeling of the Experiment

Computer simulations of radiation transport and absorption have played an important part in the research and development of nuclear borehole logging methods, including feasibility studies, optimization of design, and characterization of response. In this study, modeling is used for two distinct purposes; one is a representation of the experiments described in the preceding three chapters, and the other is a model of a borehole sonde for neutron activation analysis.

This chapter includes a general description of the Monte Carlo modeling process, followed by a discussion of the model developed to simulate the experimental program. Finally, the results of the modeling are presented.

7.1 Description of Monte Carlo nuclear modeling

A discussion of basic radiation transport principles applicable to in situ neutron activation analysis was presented in Chapter 2. One outcome of that discussion is that the reaction rate Y for a neutron reaction in a homogeneous medium with N nuclei is an integral over space V and energy E of the energy-dependent cross section σ and the spatially-dependent and energy-dependent neutron flux ϕ .

$$Y = N \int_V \int_E \phi(E,V) \sigma(E) dE dV \quad 7-1$$

Expressions such as Equation 7-1 generally cannot be analytically solved without making simplifying assumptions that compromise their applicability to practical problems. Two broad methods have evolved for estimating solutions to these types of equations. Finite element methods are based on deterministic models to solve for the average properties of the particle population. Monte Carlo methods [34,35] simulate the behavior of many individual particles to estimate the average properties.

There are essentially three parts to a radiation transport Monte Carlo model. First, there are *libraries* of energy-dependent cross sections for scattering and absorption reactions. The library contains compilations of neutron, gamma-ray, or charged particle cross sections obtained from the measurements and calculations of many people over the last half-century.

Generally, neutron cross sections are tabulated for specific isotopes, while photon and charged particle cross sections pertain to all isotopes of an element. Cross section libraries are continuously re-assessed and updated as new data become available.

The second part of the model is the *engine*, which simulates transport, scattering, and absorption of individual particles, governed by software representations of the physical principles involved. Probabilities for interactions are prescribed by the cross section libraries, and the occurrence of individual interactions according to the probabilities is determined by a mechanized roll of the dice - a random number generator. Other aspects of particle behavior which are described by probabilities, such as scattering angle, source emission angle, and source particle energy distribution are also evaluated by the random numbers.

The third part of the model is the *input*, a representation of the geometry and materials to be modeled, including radiation sources and detectors, shielding, and surrounding materials. The geometry is represented using simple geometric shapes such as cylinders, cones, and half-spaces. The simple shapes may be combined by union or intersection to form the more complex shapes required. The input also contains instructions on how the results from particle history simulations should be tallied. For example, the energy binning structure of a pulse height spectrum, analogous to pulse height channels of an ADC, is specified in the input file.

Instructions for the use of *variance reduction* techniques are also placed in the input file. To attain a statistically significant answer, many particle histories must be generated. In the simulation as in the real process, however, most particles head off to remote regions of space that are less important to the problem, and where the particles have a lessened probability of contributing to the detector tally. A preliminary calculation is performed to assess the *importances* of regions in the geometry. A region in space (or time or particle energy) is assigned a greater importance than its neighbor if it will contribute more to a detector tally. A map of importances, in all the desired dimensions of the problem, is then used as a basis to bias the particle tracking procedure so that more computer time may be devoted to tracking particles that constitute the major portion of the detector signal. The use of sample biasing is compensated by assigning weights to particles according to the reciprocal of their bias level, in the following manners.

Particles emitted from a source are assigned a weight W . If a particle enters a less important region, it may be dropped from further consideration.

The probability that the particle will not be dropped is equal to the ratio p of importances of the two regions involved, and a random number is then generated to determine the fate of the particle. If the particle is not dropped, then its weight will be increased so that

$$W_{new} = \frac{W_{old}}{p} \quad 7-1$$

In the opposite sense, a particle entering a more important region may be split into two particles. There are several schemes to accomplish this, one of which permits particle splitting only when the cumulative effect of importance changes exceeds 2. Each particle carries a parameter q that is initialized at the importance level of the cell in which the particle originates, and is adjusted by the importance ratio p each time the particle crosses into another region. At a crossing, if $q \geq 2$, the particle will split, each particle is assigned half the weight W and half of q . If the new value of q is still greater than 2, there will be another split, and so on. If a particle ultimately scores in a detector, it will count as W scoring events.

7.2 Modeling of neutron activation experiments

Material descriptions and detailed three-dimensional geometry of the irradiation facility and gamma ray counting facility were entered in MCBEND [35], a Monte Carlo based radiation transport code which utilizes UKNDL* and JEF** compilations of cross sections. In a coupled neutron/gamma case such as neutron activation, the calculated neutron flux throughout the geometry is folded with the reaction cross sections of interest, as in Equation 7-1, leading to estimates of the activation in each user-defined volume element (voxel) of the geometry. Then, in a separate calculation, the level of activation calculated for each voxel becomes a gamma ray source intensity parameter. Gamma ray transport and detector response are then simulated leading to estimates of photopeak intensity in the detector. There is no timing in the model; source intensities are configured such that, effectively, all neutrons are generated at " t_0 " and nuclides "decay" instantaneously. The units are carried through both Monte Carlo calculations consistently so that results are stated in photopeak counts per source neutron. This is equivalent to the form in which experimental results are stated in the previous chapter.

* UKNDL - United Kingdom Nuclear Data Library

** JEF - Joint European File

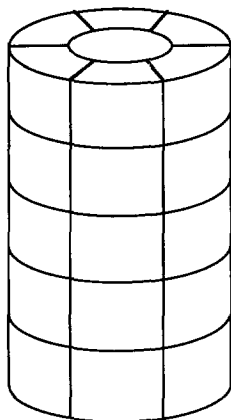


Figure 7-1 Segmentation of the sample into 35 voxels. All are of equal volume.

A voxel must be small enough that the assumed constancy of activation across its volume will not create a bias in the calculation. Preliminary runs of the model were performed with successively smaller voxels in the sample until, with 35 voxels (see Figure 7-1), no change was discernible in energy deposition in the germanium detector.

For the irradiation simulation, one run of the code which used importance mapping for variance reduction was made for calculation of the thermal neutron flux in the sample, and a separate run without importance mapping was made for calculating the hard neutron flux applicable to the threshold reactions (see Figure 7-2). Threshold reaction calculations were found to be more efficient without attempting any variance reduction, presumably because each neutron need only be tracked for a few scatters before its energy falls below the threshold. The calculations were allowed to progress until statistical uncertainty of the activation in each voxel was less than one percent. Examples of the activation calculated for each voxel are shown in Figure 7-3. There is a larger variation in fast activation intensity, a factor of 2.75 from weakest to strongest, which is related primarily to the distance from the neutron source. Thermal neutron activation shows less spatial variation, a factor of 1.16 from weakest to strongest, and is not related solely to the distance from the neutron source. There is acrylic and water all around the sample bottle, except for a column of air directly atop it, so that fewer neutrons are scattered back toward the sample from above.

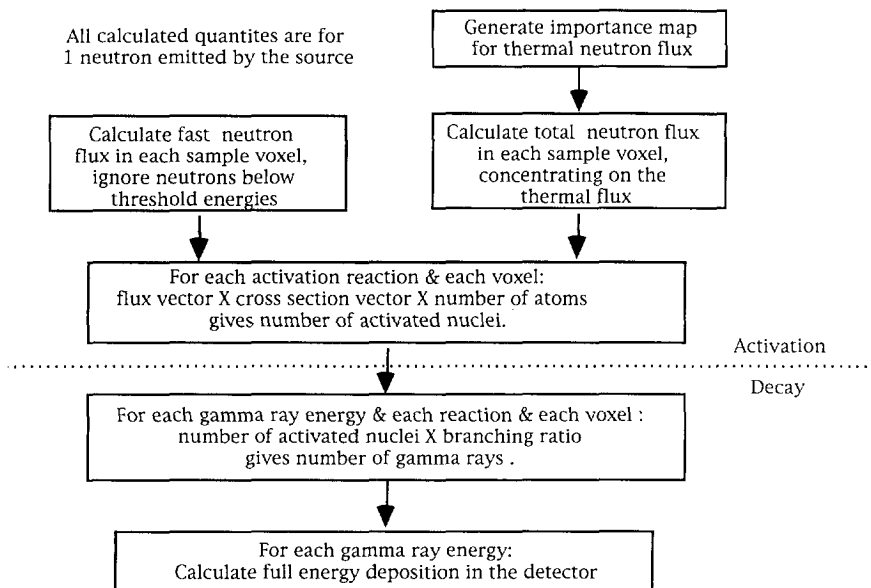


Figure 7-2 Flow chart for modeling of the experiments.

Separate gamma-ray simulation runs were made for each intermediate nuclide, with resulting full energy deposition values statistically valid to better than one percent in nearly all cases. An example of the energy deposition is presented graphically in Figure 7-4 as a pulse height spectrum. Energy bin widths have been set narrow near the peaks and wide elsewhere, so that all the salient features of a real pulse height spectrum are reproduced. Photopeak areas may then be determined in the same fashion as for "real" spectra.

Processor times of about eight hours for each hard neutron run and twelve hours for each thermal neutron run were required to obtain better than 1% precision of the activation maps, using a Sun Sparc-10. The gamma ray runs required from eight to sixteen hours of processor time each. Slightly better statistics were obtained in the later runs by splitting up cases where gamma rays are produced with widely different branching ratios, such as the 1014 and 844 keV gamma rays from the decay of ^{27}Mg , which have branching ratios of 28% and 72%, respectively. When running them together, the total processor time required to obtain a specific level of precision for each gamma ray is about twice as long.

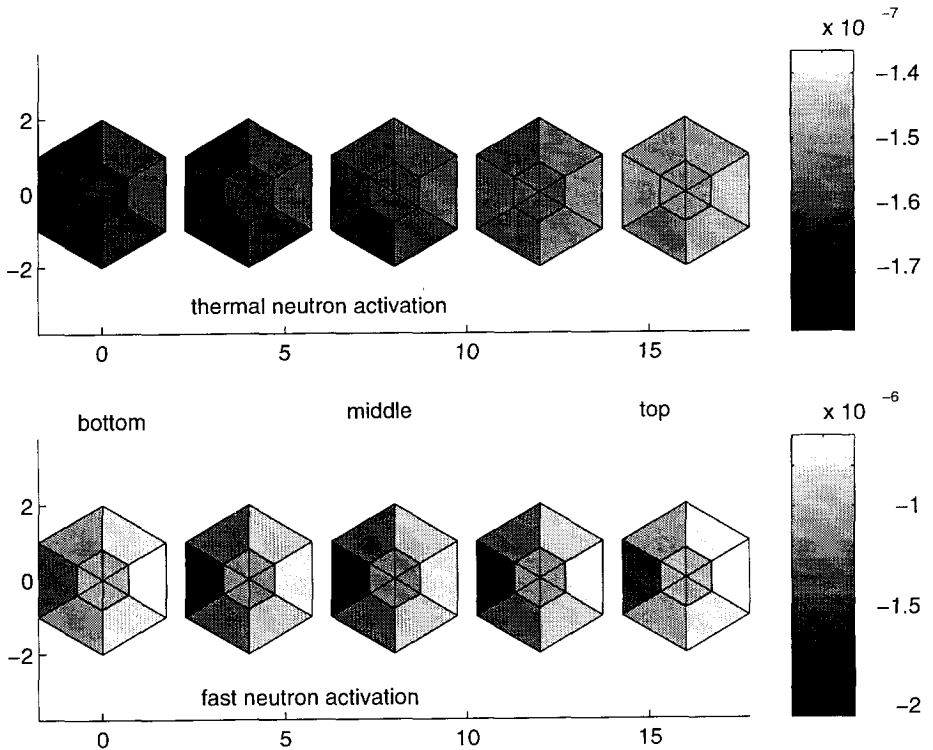


Figure 7-3 Grayscale representations of the activation intensity in each voxel throughout a sample of magnesium oxide. (a) Thermal neutron reaction $^{26}\text{Mg}(n,\gamma)^{27}\text{Mg}$. (b) Fast neutron reaction $^{24}\text{Mg}(n,p)^{24}\text{Na}$. The neutron source is to the left. There are seven voxels in each slice, as depicted in Figure 7-1. Grid lines through the center voxel in each slice through the sample are an artifact of the plotting routine. The grayscale is in activations per cm^3 per source neutron. Abscissa and ordinate scales in the figure are meaningless.

7.3 Raw modeling results

Tables 7-1 through 7-4 list the results of calculations made for the same samples that were discussed in section 6.1. The values listed are:

$$C_{\text{mod}} = \frac{\text{photopeak area}}{\left(\text{gram of element} \right) \left(\text{source neutron} \right)}. \quad 7-2$$

The units of C_{mod} are the same as the units of C_{exp} presented in the previous chapter, and also included in Tables 7-1 through 7-4. The term *gram of element* refers to the sum of all the isotopes. The commonly accepted values from the literature for isotopic abundance were used (see Appendix F).

Modeling and experimental results will be reconciled in the next chapter.

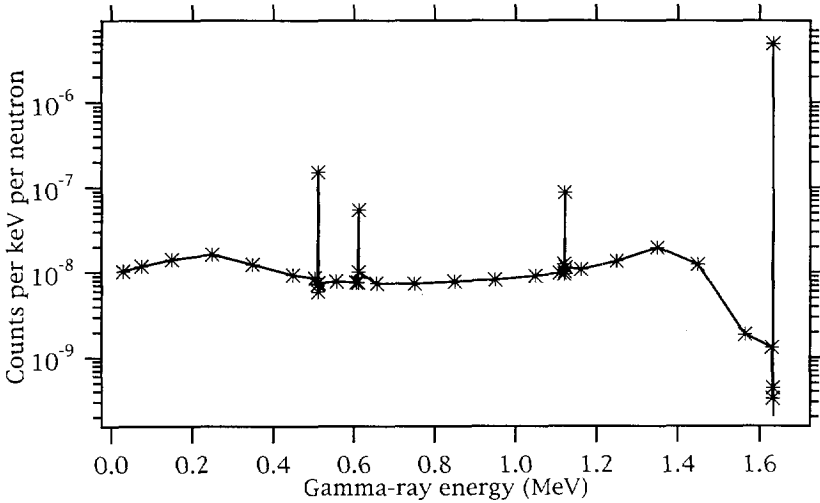


Figure 7-4 A synthetic pulse height spectrum from 1633 keV gamma rays. Energy bins are of variable width, but their contents are scaled to represent 1 keV bins. The 511 keV peak is from pair production outside the germanium crystal. The feature near 1400 keV is the Compton edge from the 1633 keV gamma ray.

Table 7-1 $C_{\text{mod}} (\times 10^9)$ and $C_{\text{exp}} (\times 10^9)$ for Magnesium reactions					
Reaction	Gamma-ray energy (keV) and branching ratio	$C_{\text{mod}} (\times 10^9)$		$C_{\text{exp}} (\times 10^9)$ (averages)	
$^{24}\text{Mg}(n,p)^{24}\text{Na}$	1368.6(100)	46.9	0.7%	31.4	9%
	2754.1(100)	30.9	0.8%	21.0	12%
$^{25}\text{Mg}(n,p)^{25}\text{Na}$	390.7(12.8)	0.410	0.9%	0.447	5%
	585.9(13)	0.331	0.9%	0.311	5%
	975.2(12.8)	0.245	1.0%	0.301	9%
	1611.9(8.8)	0.123	1.2%	0.158	9%
$^{26}\text{Mg}(n,\alpha)^{23}\text{Ne}$	439 (33)	1.79	0.4%	0.838	13%
$^{26}\text{Mg}(n,\gamma)^{27}\text{Mg}$	843.8(72)	0.854	0.6%	0.702	4%
	1014.4(28)	0.302	0.9%	0.269	8%

Table 7-2 $C_{\text{mod}}(\times 10^9)$ and $C_{\text{exp}}(\times 10^9)$ for Sodium reactions				
Reaction	Gamma-ray energy (keV) and branching ratio	$C_{\text{mod}}(\times 10^9)$		$C_{\text{exp}}(\times 10^9)$ (averages)
$^{23}\text{Na}(n,\gamma)^{24}\text{Na}$	1368.6(100)	98.1	1.1%	78.7 4%
	2754.1(100)	68.6	1.2%	45.6 5%
$^{23}\text{Na}(n,p)^{23}\text{Ne}$	439 (33)	8.29	0.3%	7.16 3%
$^{23}\text{Na}(n,\alpha)^{20}\text{F}$	1633.1(100)	34.1	0.8%	22.1 3%

Table 7-3 $C_{\text{mod}}(\times 10^9)$ and $C_{\text{exp}}(\times 10^9)$ for Aluminum reactions				
Reaction	Gamma-ray energy (keV) and branching ratio	$C_{\text{mod}}(\times 10^9)$		$C_{\text{exp}}(\times 10^9)$ (averages)
$^{27}\text{Al}(n,\alpha)^{24}\text{Na}$	1368.6(100)	29.3	0.5%	23.3 6%
	2754.1(100)	19.9	0.6%	13.4 9%
$^{27}\text{Al}(n,p)^{27}\text{Mg}$	843.8(72)	18.7	0.4%	14.4 2%
	1014.4(28)	6.59	0.7%	5.03 3%
$^{27}\text{Al}(n,\gamma)^{28}\text{Al}$	1778.8(100)	33.8	0.8%	25.1 6%

Table 7-4 $C_{\text{mod}}(\times 10^9)$ and $C_{\text{exp}}(\times 10^9)$ for Silicon reactions				
Reaction	Gamma ray energy (keV) and branching ratio	$C_{\text{mod}}(\times 10^9)$		$C_{\text{exp}}(\times 10^9)$ (averages)
$^{30}\text{Si}(n,\alpha)^{27}\text{Mg}$	843.8(72)	0.412	0.6%	0.329 12%
	1014.4(28)	0.145	1.0%	0.110 9%
$^{28}\text{Si}(n,p)^{28}\text{Al}$	1778.8(100)	46.26	0.6%	35.0 8%
$^{29}\text{Si}(n,p)^{29}\text{Al}$	1273(91)	1.069	0.9%	0.986 6%
	2028(3.4)	0.031	5.3%	0.031 10%
	2426(5.5)	0.047	4.0%	0.042 7%

Chapter 8 Comparison of Modeling and Experiments

The purpose of this section of the investigation is to evaluate the validity of energy-dependent cross section compilations for activation reactions in the mixed-energy neutron flux in a water tank. This is accomplished by comparisons of modeled and measured activation responses of Na, Mg, Al, and Si samples. The photopeaks from decay gamma rays are related to the cross sections by Equation 2-35, repeated here.

$$photopeak = g(t, \tau) \epsilon b N \int_V \int_E \phi(E, V) \sigma(E) \Omega(V) dE dV \quad 8-1$$

The Monte Carlo modeling is just a simulation of the entire process described by this equation, with the exception of the function g , which is equal to 1 since no timing aspects of the problem were included in the model. Also, in the Monte Carlo modeling, the neutron flux $\phi(E)$ represents the flux *per neutron emitted from the source*. Experimental results were reported with the effects of g and the source intensity S_0 removed, so that the values of C_{exp} reflect the total counts per neutron emitted at time t_0 . These features are inherent in the modeling calculations, with values of 1 for both source intensity and the timing function. Both results were reported per unit mass m , so that the ratio of results is

$$\frac{C_{exp}}{C_{mod_adj}} = \frac{\left(\frac{photopeak}{m S_0 g(t, \tau)} \right)_{exp}}{\left(\frac{photopeak}{m} \right)_{mod}} = \frac{\left(\frac{\epsilon b N}{m S_0} \int_V \int_E \phi(E, V) \sigma(E) \Omega(V) dE dV \right)_{exp}}{\left(\frac{\epsilon b N}{m} \int_V \int_E \phi(E, V) \sigma(E) \Omega(V) dE dV \right)_{mod}} \quad 8-2$$

8.1 Sources of inaccuracy in the comparison

The desired quantity to be compared is a direct ratio of the cross section vectors $\phi(E)_{exp}/\phi(E)_{mod}$ which lie hopelessly buried within the integrals in Equation 8-2. The best that can be achieved in the experiments is to observe the total response integral including both neutron and gamma-ray transport. Then if the assumption is made that the modeling is a close replication of the

experiments in all aspects with the possible exception of the cross section compilations, a basis is formed for using the ratios in Equation 8-2 as an evaluation of the cross section libraries. The components of the equation will be scrutinized for potential inaccuracies in the following sections.

8.1.1 Gamma-ray transport efficiency

The geometry of the counting setup is simple, with no intervening scattering medium between sample and detector. Also, with only full energy detection under consideration, geometry external to the sample and detector becomes less important, because a gamma ray that scatters once outside the detector is no longer of concern. The largest factor affecting $\Omega(V)$ is the spacing of the sample from the detector, which is only 8.6 cm center-to-center, or a gap of slightly less than 2 cm between the two. The effective solid angle that the detector presents to the sample changes rapidly with distance at this spacing. The dimensions of the sample and detector also affect the solid angle. An additional consideration is the accuracy with which the intervening material is represented in the model, both geometrically and by composition, including the sample bottle, detector housing, and the sample itself. These will be small effects, since the mean free path of the gamma radiation is considerably longer than the dimensions involved. Finally, the accuracy of the gamma-ray cross section library and implementation of the code engine come into play.

8.1.2 Gamma-ray detection efficiency

Differences in efficiency between real and modeled detectors may be caused by improper representation of the detector geometry and composition, and library and engine inaccuracies. These are the same factors that affect $\Omega(V)$ in the model, since the estimation of energy deposition in a detector is simply a bookkeeping account of gamma-ray and electron interactions.

Observation of gamma-ray pairs of constant and known relative intensity, such as the 2.754 and 1.369 MeV pair from the decay of ^{24}Na , may be used as a crude check on the detector performance in the model. The ratio of photopeak areas N_{Low}/N_{High} of the low- and high-energy gamma rays should be the same in both model and experiment. The "ratio of ratios", as follows, is listed in Table 8-1 for several gamma-ray pairs.

$$R = \frac{\left(N_{Low}/N_{High}\right)_{EXP'T}}{\left(N_{Low}/N_{High}\right)_{MODEL}} \quad 8-3$$

Nuclide	γ ray pair (keV)	R	uncertainty (%)
^{24}Na	1369 / 2754	1.13	13
^{29}Al	1273 / 2426	1.03	10
	1273 / 2028	0.93	12
	2028 / 2426	1.10	14
^{25}Na	391 / 1612	0.85	10
	585 / 1612	0.73	10
	975 / 1612	0.96	13
	391 / 975	0.89	10
	585 / 975	0.77	11
	391 / 585	1.16	7.4
^{27}Mg	844 / 1014	1.00	8.9

Table 8-1 The observed ratio between experiment and model for pairs of gamma rays of constant relative intensity is used as a check on model performance.

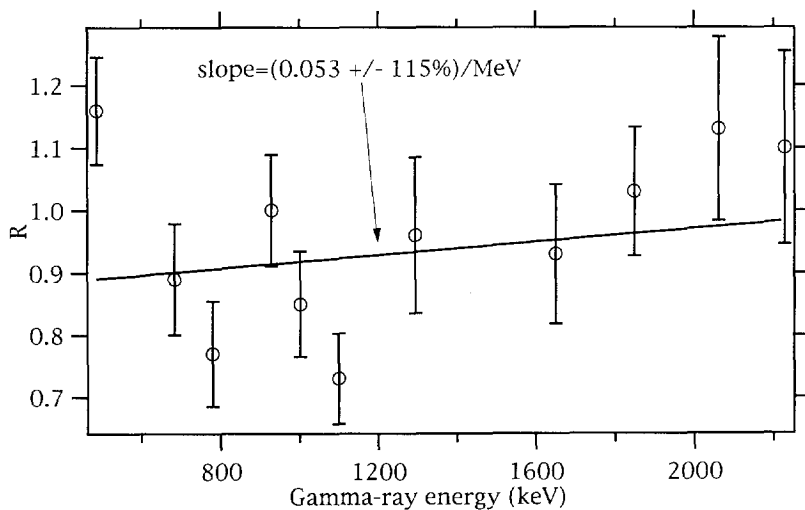


Figure 8-1 The ratio R from Table 8-1 is plotted against the midpoint of the gamma-ray pair. The line is a fit to the data using the reciprocal of uncertainty as the weight. The slope has an uncertainty greater than its value, and the fit as drawn only explains 11% of the variation in the data

A weighted fit of the ratio to the midpoint of the gamma ray energies, shown in Figure 8-1 reveals that less than 11% of the variation in the ratio may be attributed to a linear dependence on energy. The derived ratio has poor

precision and cannot be used as a basis for any energy-dependent correction of the modeled response. It is only used as an indicator of performance, to the extent that it does not illuminate any problems with the model.

8.1.3 Photopeaks and the pulse height spectrum

The synthetic pulse height spectrum from Monte Carlo does not suffer from any charge collection, pileup, dead time, noise, or peak broadening effects that are seen in the real detector. Thus instrumental problems such as these that are not compensated properly, or are not recognized, may have an impact on the accuracy of any comparisons between measurements and modeling. Peak broadening simply introduces larger statistical fluctuations unless it is not recognized, when it may cause gross inaccuracies. Pileup and dead time are monitored in the experiments, reaching as much as 8% each in the silicon and aluminum runs, and corrections to the calculated peak areas are performed.

8.1.4 Neutron flux in the sample

Modeling of the neutron flux is a considerably more complex task than the gamma-ray problem. However, the same geometrical and compositional considerations of the gamma-ray transport problem are important when assessing the accuracy of the neutron flux calculations. The center-to-center spacing of the sample and neutron source is 9.58 cm, only twice the diameter of the sample bottle, making it important that all dimensions are represented accurately. The intervening and surrounding geometry is much more complex than for the gamma-ray problem, consisting mostly of water and acrylic, which are good neutron moderators. A potential source of inaccuracy in a modeling representation of the experiment comes from the presence of air gaps and channels in the region of the source and sample.

Many neutron scattering and absorption cross sections, in addition to the reaction cross sections under evaluation, are used to calculate the neutron flux in the sample. Thus, remarks about the libraries and engine that were applicable to gamma-ray transport in the model are also pertinent here.

8.1.5 Timing aspects of gamma-ray counting

The generalized function $g(t, \tau)$ in Equation 8-2 represents the time-related efficiency of counting decay gamma rays. The decay time constants τ of elements are known well enough that they are not a concern in assessing the accuracy of measurements. The most critical quantity in $g(t, \tau)$ is the elapsed time between shutdown t_0 and the onset of counting t_1 in the first acquisition gate. This is calculated as a difference between two absolute times, thus if it is a

short time compared to the accuracy and precision of the two absolute time measurements, there could be substantial error or uncertainty. Precisions attained in the measurements are about thirty milliseconds for t_0 and less than 1 millisecond for t_1 , thus the precision of the difference is never more than 0.3% of either the transfer times (10 to 20 seconds) or the shortest nuclide half-life of concern (11 seconds).

8.1.6 Effective neutron source strength

The source intensity is always defined to be one neutron per second in the model, and it is always emitted at time t_0 . In the experiments, the output of the neutron generator fluctuates relative to its nominal value, which was determined experimentally with a copper activation procedure to be $1.35 \times 10^8 \pm 15\%$ n/s, as discussed in chapter 4. At the same operating conditions of the accelerator, recordings of the countrates in three neutron monitors were made, to provide a gross absolute calibration for the experiments. Countrates in the monitors are high enough that there is excellent precision for each 1 second period of data acquisition (14 MeV monitor 2.5%, epithermal monitor 1.9%, thermal monitor 0.6%). Additionally it was shown in chapter 4 that there is very little sample effect upon the monitor readings. Thus, relative calibration of source intensity between runs is adequate, despite the large uncertainty in the absolute calibration. Accuracy of the derived effective source intensity S_0 depends on the stability of the monitors over time, and the linearity of their response to neutron flux.

8.1.7 Mass and number of atoms, and branching ratios

Masses of the samples, typically several hundred grams, were determined with a calibrated balance having 0.001 gram precision, and purity of the chemicals used exceeded 99.99% as certified by the manufacturer, so that the elemental masses m are determined very precisely. The number of atoms N in Equation 8-2 refers to the specific isotope, and is calculated using the generally accepted numbers for isotopic abundances. The accuracy depends on lack of isotopic fractionation in the chemical product. Any fractionation will be considerably less than the ability to sense it with these methods. Branching ratios are known to well within the precision needed.

8.2 Normalization of experiments and model

A summary of experimental and modeling results for sodium, magnesium, aluminum, and silicon in terms of the ratio $C_{\text{exp}}/C_{\text{mod}}$ is presented in Table 8-2. There is one more step that must be taken in the comparison, an overall

normalization of the modeling to the experiments. The normalization will compensate for the large uncertainty of the absolute neutron output of the experiments, and for any other effects discussed in the preceding sections that are constant throughout all experiments.

The normalization is based on the thermal neutron responses because of the confidence that has been established over the years in the knowledge of thermal neutron cross sections. The average of the thermal neutron reaction ratios $C_{\text{exp}}/C_{\text{mod}}$ is $0.785 \pm 11.1\%$, which will be used as the normalization constant. Results of the normalization are plotted in Figure 8-2, and are listed in Table 8-3.

$C_{\text{exp}}/C_{\text{mod}}$ for Mg, Na, Al, Si					
Intermediate nuclide	Gamma ray energy (keV)	Mg	Na	Al	Si
^{24}Na	1368.6	0.669 9%	<u>0.803</u> 4%	0.797 6%	
	2754.1	0.679 12%	<u>0.665</u> 5%	0.673 9%	
^{25}Na	390.7	1.089 5%			
	585.9	0.940 5%			
	975.2	1.229 9%			
	1611.9	1.282 9%			
^{23}Ne	439	0.469 13%	0.864 3%		
^{27}Mg	843.8	<u>0.822</u> 4%		0.770 2%	0.798 12%
	1014.4	<u>0.891</u> 8%		0.763 3%	0.758 9%
^{20}F	1633.1		0.649 3%		
^{28}Al	1778.8			<u>0.744</u> 6%	0.757 8%
^{29}Al	1273				0.922 6%
	2028				0.989 11%
	2426				0.899 8%

Table 8-2 The ratio $C_{\text{exp}}/C_{\text{mod}}$ is the non-normalized comparison of experiments and simulation. The uncertainties reported are propagated from both sources, but are dominated by the experimental uncertainties. Underlined figures in the table are the results for thermal neutron interactions that will be used for normalization.

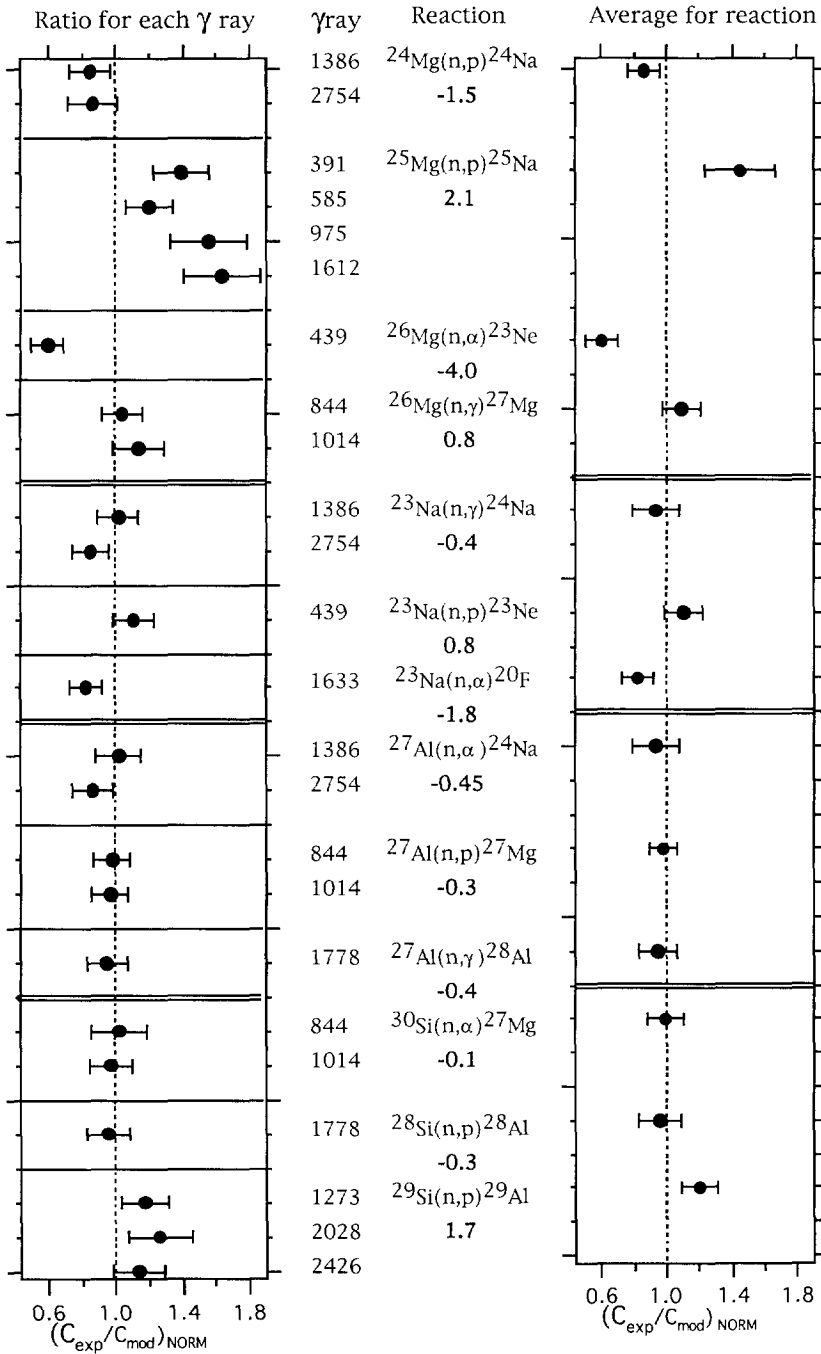


Figure 8-2 The caption for this figure is on the next page.

Figure 8-2 (previous page) The normalized ratios and their uncertainties are plotted for each gamma ray observed (left). The average is plotted for each reaction (right). Beneath each reaction name is the number of standard deviations away from unity for the right-hand plot. Two of the averaged values have significant differences from unity. Most notably, the calculated response for the fast neutron reaction $^{26}\text{Mg}(n,\alpha)^{23}\text{Ne}$ differs greatly and significantly from the measured response. The fast neutron reaction $^{25}\text{Mg}(n,p)^{25}\text{Na}$ also exhibits a large and statistically significant difference.

$(C_{\text{exp}}/C_{\text{mod}})_{\text{NORM}}$ for Mg, Na, Al, Si				
Intermediate nuclide	Mg	Na	Al	Si
^{24}Na	0.859 ± 0.093	<u>0.935 ± 0.147</u>	0.936 ± 0.143	
^{25}Na	1.446 ± 0.218			
^{23}Ne	0.597 ± 0.100	1.100 ± 0.125		
^{27}Mg	<u>1.091 ± 0.116</u>		0.976 ± 0.079	0.991 ± 0.113
^{20}F		0.826 ± 0.094		
^{28}Al			<u>0.947 ± 0.121</u>	0.964 ± 0.134
^{29}Al				1.193 ± 0.113

Table 8-3 Values from Figure 8-3 after normalization and averaging. Underlined values are for thermal neutron reactions.

8.3 Conclusions

It has been shown that integral measurements on small samples in the laboratory can be performed to assess the validity of calculated high energy neutron activation response integrals, and this has been done for four elements. The measured activations of sodium, magnesium, aluminum, and silicon samples were compared to calculated values predicted by compilations of the reaction cross sections, for the purposes of assessing the validity of response integral estimates. This was accomplished through response integral experiments similar to what would pertain in a borehole measurement. Activation was done with a miniaturized D-T neutron generator in a water tank. The tank, source, and sample holder geometries were designed to expose the sample to the full energy distribution of neutrons from the source emission energy of 14 MeV down to thermal energy, exciting delayed gamma ray activity from (n,p), (n, α), (n,2n), (n, γ), and other reactions. Counting of the decay gamma rays was done with a coaxial high-purity germanium spectrometer with volume of 400 cm³.

Calculations of the neutron activation and gamma-ray counting were performed using the Monte Carlo radiation transport program MCBEND, its associated cross section libraries, and an exact representation of the experimental conditions.

The assumption was made that all aspects of the model replicated the experiment so well that any discrepancies must be due to an inaccurate representation of the cross sections in the model. This assumption was confirmed through the accurate model characterization of the thermal neutron reaction (n,γ) results, where the cross sections have been well determined. After normalization of modeling and experimental results, it was observed that two of the thirteen reaction rates studied for sodium, magnesium, aluminum, and silicon displayed large and statistically significant discrepancies between measured and predicted responses. Both discrepancies relate to the fast neutron activation of magnesium. Rates predicted for the reaction $^{26}\text{Mg}(n,\alpha)^{23}\text{Ne}$ are too optimistic and must be corrected by a factor of 0.60 ± 0.10 when used in the conditions of this study. Similarly, the response calculated from $^{25}\text{Mg}(n,p)^{25}\text{Na}$ cross sections must be boosted to agree with experiments. The average shortfall in the response integral for the family of four peaks from this decay is a factor of 1.44 ± 0.22 .

The threshold for this reaction is steep and the cross sections are important over only a narrow energy region when a 14 MeV source is used, perhaps down to 9 or 10 MeV, so it is not too surprising that this discrepancy is observed. It must be pointed out that comparisons of this sort are based on the total activation response for a reaction over all neutron energies, and cannot be used to assess the reaction cross section at any one energy. Also, strictly speaking, the results are valid only for a region in which the spatial and energy distribution of the neutron flux is identical to that of the studied sample.

A few other differences in the data between experiments and modeling are statistically significant despite being only half as large, with discrepancies approaching 2 standard deviations.

Another feature of the normalized data serves to reinforce confidence in the conclusions of this comparison. The reaction $^{23}\text{Na}(n,p)^{23}\text{Ne}$ which competes with $^{26}\text{Mg}(n,\alpha)^{23}\text{Ne}$ is represented adequately by modeling, so that any consistent systematic error in the gamma ray transport and detection in either experiment or modeling is eliminated from consideration.

Observations of pairs of gamma rays with known relative intensities may be used as an evaluation of the detector performance in a model.

Representations of an earth formation, a borehole, and a possible downhole activation sonde were entered into the MCBEND [35] modeling code for the purpose of assessing sonde response to the rock-forming elements sodium, magnesium, aluminum, and silicon. An additional purpose is the development of a formalism to relate the results of laboratory measurements on small samples to what would be obtained in a borehole measurement. A shaly, feldspathic sand and a series of dolomites containing typical elemental concentrations were simulated. The sonde model consisted of a miniature 14 MeV neutron source and a germanium spectrometer. Calculations were performed with no timing aspects included, so that post-processing could calculate responses at any logging speed, source-to-detector spacing, or neutron source intensity.

Modeling calculations of the sonde response were performed for seven instances of varying borehole conditions, including hole size, standoff and centering, and mud weight. Formation conditions were held constant for these calculations. The sensitivity to magnesium in a carbonate formation was used as a basis for assessing these environmental effects. Magnesium has both fast and thermal neutron activation reactions resulting in a wide range of gamma-ray energies. The effects of changing conditions on the response to magnesium will be very similar to the effect on activation of other elements.

Five instances of varying formation conditions were simulated, including density and hydrogen index changes, and the presence of saltwater and other thermal neutron absorbers. The sensitivity to magnesium was calculated to assess the effect of these conditions.

9.1 Setup of the model

The Monte Carlo modeling of neutron activation is a two-step process. The first half is the calculation of the neutron flux as a function of energy and position throughout the model geometry, and also the folding of the flux with the neutron activation reaction cross sections to create a map of activation sites. An isotropic 14.0 MeV neutron source was used for the simulation. This is a close approximation of the output from a D-T accelerator operating at 100 kV. A section of the 9.2 cm diameter sonde used for the irradiation part of the model is shown schematically in Figure 9-1.

Beyond the 20 cm diameter borehole, the modeled formation is split into small enough regions that the calculation will not be biased by assuming constant activation across their volumes. The sizes of the regions were determined by some preliminary runs of the model in which the formation volume was divided into successively smaller and smaller pieces until no statistically significant change could be seen in the results. Generally, regions near the sonde are defined with smaller volumes than regions far away because most of the signal for this type of measurement comes from the nearby volume. A mesh for the formation regions was defined using cylindrical coordinates (r,θ,z) , with the z -direction defined to be along the borehole axis. Coordinates representing the distance in centimeters from the center of the model, for purposes of recording the activation, are listed below.

$$r=[10, 11, 12, 14, 16, 18, 20, 24, 28, 34, 40, 48, 56, 66, 100],$$

$$z=[0, 2.5, 5, 7.5, 10, 15, 20, 25, 30, 40, 50, 65, 100].$$

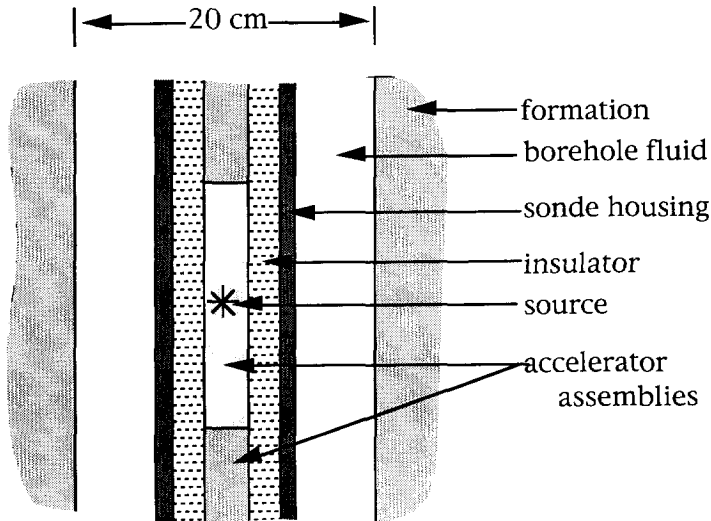


Figure 9-1. Schematic of the accelerator region in the irradiation geometry for a centered 9.2 cm diameter sonde in a 20 cm borehole. The entire model is 200 cm in diameter and also 200 cm from top to bottom.

The neutron source is always placed at $z=0$ so that the model is symmetric in the z -direction. Activation is only recorded for the upper half ($z > 0$) and then doubled, however the lower half retains its scattering and absorption capabilities. Azimuthally, the formation is cut into eight equal wedges in such

a way that the sonde is on the azimuthal center of one of the pieces (see Figure 9-2). In this configuration, there are five unique wedges, making a total of 840 unique regions in which activation is recorded. With the eccentered sonde at 0 radians, the azimuthal boundaries are as follows.

$$\theta = \left[\frac{\pi}{8} \quad 3\frac{\pi}{8} \quad 5\frac{\pi}{8} \quad 7\frac{\pi}{8} \quad 9\frac{\pi}{8} \quad 11\frac{\pi}{8} \quad 13\frac{\pi}{8} \quad 15\frac{\pi}{8} \right]$$

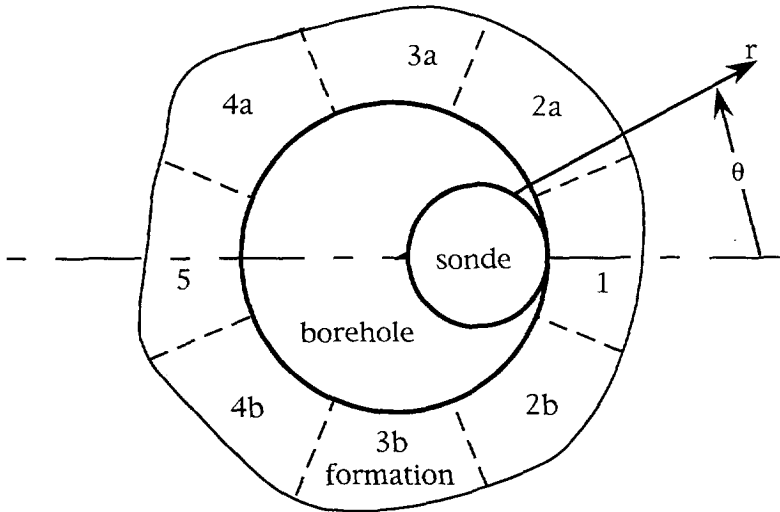


Figure 9-2 This view of the model geometry along the borehole axis shows the position of the sonde with respect to the eight azimuthal formation segments. There are five unique segments. The formation extends to a total radius of 100 cm. The origin of the coordinate system is at the center of the borehole.

An importance map was generated, and a single irradiation run made for all thermal and fast neutron reactions of interest. The neutron flux was calculated in each volume element, or *voxel*, to the desired precision as determined internally by the MCBEND program. For the centered sonde, calculations were allowed to progress until neutron flux precisions of 0.5% were achieved in the voxels closest to the source. For the eccentered case, with many more and smaller voxels, the runs were stopped when precision of the calculated flux in several of the nearest voxels reached 2%. The methods described in Chapter 7 (Figure 7-2) were followed from this point on. The number of activated nuclei were counted for each reaction of interest, and the resulting activation map was multiplied by appropriate branching ratios to make a map of gamma-ray source intensities. Examples of activation maps are presented in Figures 9-3 and 9-4. As expected, the maps show intense localized activation

from fast neutrons adjacent to the source. Thermal neutron activation is less intense but is spread out over a larger volume. There is a larger azimuthal variation of the fast neutron activation.

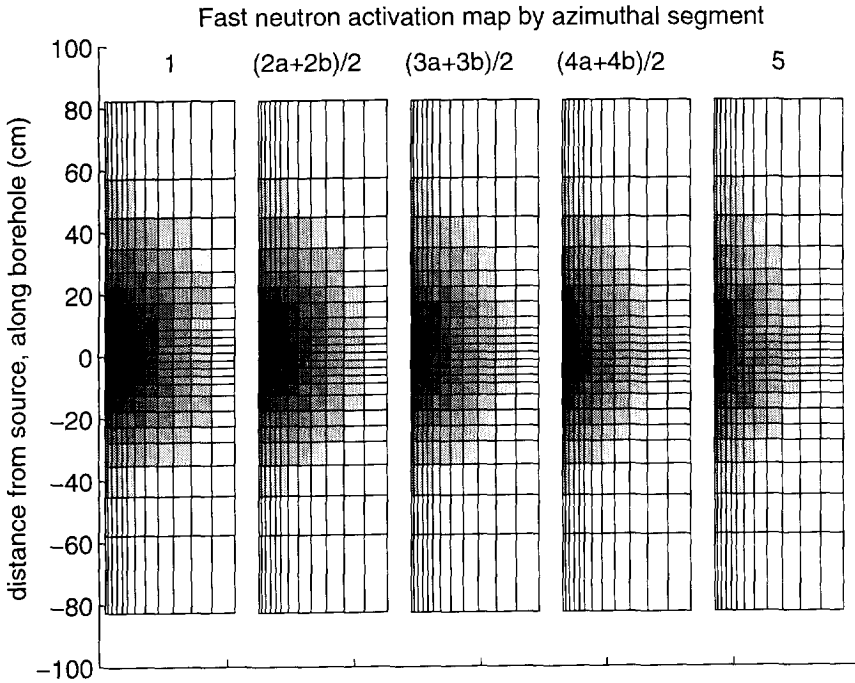


Figure 9-3 Calculated activation map for the threshold reaction $^{24}\text{Mg}(n,p)^{24}\text{Na}$ in a 15 pu dolomite, using an ecentered sonde. There are five unique azimuthal regions, or "wedges" of angle $\pi/4$ defined in the model. The numbers at the top of each image indicate which of the regions from Figure 9-1 is represented. The darker shading represents a higher probability that any one ^{24}Mg atom in the region will be activated. Each of the five images extends from the edge of the borehole to a radial distance of 83 cm into the formation.

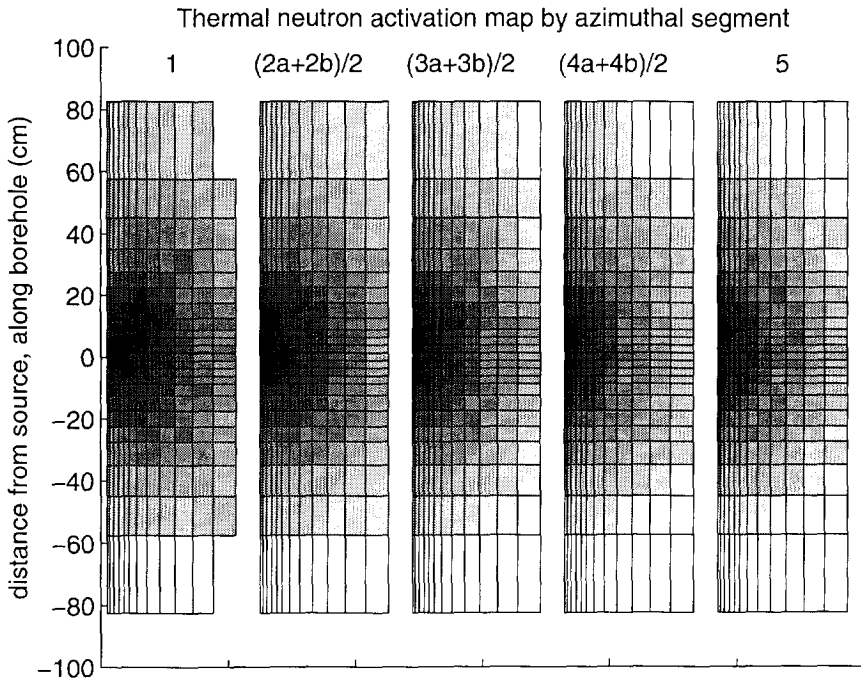


Figure 9-4 Calculated activation map for the thermal reaction $^{26}\text{Mg}(n,\gamma)^{27}\text{Mg}$ in a 15 pu dolomite, using an eccentered sonde. The shading represents the probability that any one ^{26}Mg atom will be activated. See the caption for Figure 9-3.

Geometries of the gamma ray counting model and the irradiation model are the same, except for the sonde. The formation gridding scheme remains the same to accommodate the gamma ray source intensity map. The sonde geometry is shown schematically in Figure 9-5.

9.2 Elemental sensitivities in a shaly sand

A typical shaly sand [59,60] was used to determine the sensitivities of the sonde to sodium, magnesium, silicon, and aluminum. The composition of this formation is listed in Table 9-1. Total density of the formation is 2.344 g/cm^3 . The sonde was eccentered in a 20 cm borehole, containing mud of specific gravity 1.42. Volume fractions of the mud constituents are: kaolinite, 10%; hematite, 6%; water, 84%. Neutron cross sections for barium were not available at the time this problem was run, so hematite weighting of the mud was used.

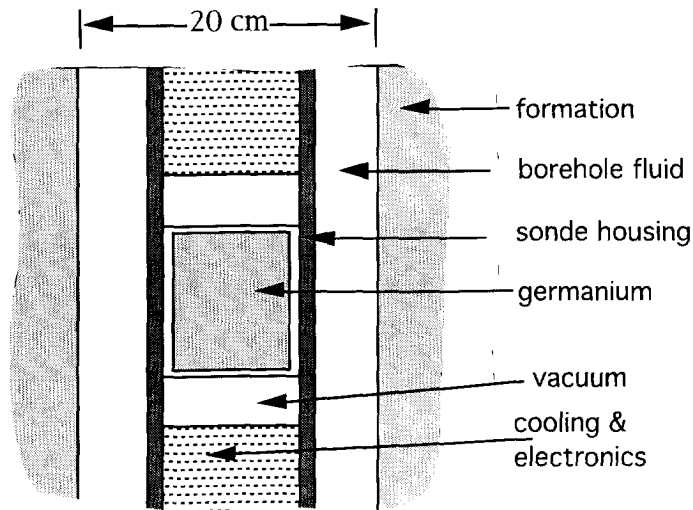


Figure 9-5. Schematic of the detector region in the gamma ray counting geometry for a centered 11 cm diameter sonde in a 20 cm borehole. The germanium crystal is 7.6 cm in diameter and 8.8 cm in length.

Element	Mass concentration
O	54.3
Si	32.2
Al	5.18
K	1.789
Fe	1.76
Na	1.62
Ca	0.65
Mg	0.58
H	1.15
Ti	0.29
C	0.29
S	0.17
P	0.047
Mn	0.037
B	49 ppm
Gd	4.5 ppm

9.2.1 Raw modeling results

Results of the modeling are stated as the number of photopeak counts from time $t_0 \rightarrow t_\infty$ for each reaction, per source neutron emitted at time t_0 . This is the same convention that was used for the experimental and modeling results in Chapters 6 and 7. Modeling results from the reactions $^{25}\text{Mg}(n,p)^{25}\text{Na}$ and $^{26}\text{Mg}(n,\alpha)^{23}\text{Ne}$ have been adjusted by the response integral correction factors determined in Chapter 8 for the neutron flux in a water tank. The adjusted results are reported in Tables 9-2 through 9-5 as $C_{\text{mod}_{ss}}$. Calculations were allowed to proceed until the precision of peak areas in the derived gamma-ray spectrum was 1%, as calculated by the MCBEND program.

To determine the elemental sensitivity from the modeling results, assumptions must be made about the logging speed, depth integration interval, neutron source intensity, and spacing between the source and detector. A logging speed v of 180 meters per hour (1/6 feet per second) will be used. Other elemental logging equipment is often used at this speed. Attempts to log slower than this very often meet with problems of sonde stick-and-slip. The usual practice for nuclear logs is the recording of logged values for fixed intervals j of cable movement, typically every 15.24 cm (6 inches). Subsequent averaging of the recorded values over d vertical intervals may be performed. An absolute neutron generator output S of 1×10^9 neutrons per second will be assumed.

A large decay gamma-ray signal can be obtained by reducing the distance l between source and detector. If the distance is reduced too much, prompt gamma ray activity will be detected. Measurements performed with a neutron generator and large scintillator [61] show that relatively insignificant prompt gamma-ray detection is achieved when the spacing l is 1.8 meters (6 feet) or greater.

The photopeak counts $C_{\text{log}_{ss}}$ attainable while logging are estimated by equation 9-1. The exponential term in brackets is the efficiency of the counting time interval, and the other exponential term represents the loss due to decay while irradiation is still taking place. The exponential decay time constant is τ .

$$C_{\text{log}_{ss}} = C_{\text{mod}_{ss}} S \tau \left(1 - e^{-dj/v\tau}\right) \left[e^{-l/v\tau} - e^{(l/v\tau - dj/v\tau)} \right] \quad 9-1$$

Reaction	Gamma-ray energy (keV)	$C_{\text{mod}_{ss}} (\times 10^9)$	$\frac{C_{\text{mod}_{ss}} (\times 10^9)}{\text{mg/cm}^3}$	$\frac{C_{\text{log}_{ss}}}{\text{mg/cm}^3}$
$^{24}\text{Mg}(n,p)^{24}\text{Na}$	1368.6	721	53.0	0.550
	2754.1	623	45.8	0.475
$^{25}\text{Mg}(n,p)^{25}\text{Na}$	390.7	4.75	0.349	1.95
	585.9	4.77	0.351	1.95
	975.2	4.62	0.340	1.89
	1611.9	2.89	0.213	1.18
$^{26}\text{Mg}(n,\alpha)^{23}\text{Ne}$	439	8.85	0.651	4.25
$^{26}\text{Mg}(n,\gamma)^{27}\text{Mg}$	843.8	14.2	1.044	0.98
	1014.4	5.70	0.419	0.39

Table 9-2 Results of sonde response model calculations for magnesium in a shaly sand. The third column, $C_{\text{mod}_{ss}} (\times 10^9)$, contains the photopeak counts, collected over all time, per neutron emitted at time t_0 . The fourth column contains the photopeak counts divided by the density (mg/cm^3) of magnesium in the rock. The final column contains the number of counts that would be attained, per magnesium density of 1 mg/cm^3 , if logging proceeded using the conditions described in the preceding paragraphs.

Reaction	Gamma-ray energy (keV)	$C_{\text{mod}_{ss}} (\times 10^9)$	$\frac{C_{\text{mod}_{ss}} (\times 10^9)}{\text{mg/cm}^3}$	$\frac{C_{\text{log}_{ss}}}{\text{mg/cm}^3}$
$^{23}\text{Na}(n,\gamma)^{24}\text{Na}$	1368.6	7580	199.6	2.072
	2754.1	7368	194.0	2.014
$^{23}\text{Na}(n,p)^{23}\text{Ne}$	439	237	6.250	40.80
$^{23}\text{Na}(n,\alpha)^{20}\text{F}$	1633.1	1863	49.07	150.9

Table 9-3 Results of sonde response model calculations for sodium in a shaly sand. The final column is the estimated number of counts per sodium density of 1 mg/cm^3 for these logging conditions.

Reaction	Gamma-ray energy (keV)	$C_{\text{mod}_{ss}} (\times 10^9)$	$\frac{C_{\text{mod}_{ss}} (\times 10^9)}{\text{mg/cm}^3}$	$\frac{C_{\text{log}_{ss}}}{\text{mg/cm}^3}$
$^{27}\text{Al}(n,\alpha)^{24}\text{Na}$	1368.6	4691	38.64	0.401
	2754.1	4079	33.60	0.349
$^{27}\text{Al}(n,p)^{27}\text{Mg}$	843.8	2515	20.72	19.42
	1014.4	968	7.974	7.473
$^{27}\text{Al}(n,\gamma)^{28}\text{Al}$	1778.8	8316	68.50	226.5

Table 9-4 Results of sonde response model calculations for aluminum in a shaly sand. The final column is the estimated number of counts per aluminum density of 1 mg/cm^3 for these logging conditions.

Reaction	Gamma-ray energy (keV)	$C_{\text{mod}_{ss}} (\times 10^9)$	$\frac{C_{\text{mod}_{ss}} (\times 10^9)}{\text{mg/cm}^3}$	$\frac{C_{\text{log}_{ss}}}{\text{mg/cm}^3}$
$^{28}\text{Si}(n,p)^{28}\text{Al}$	1778.8	54158	71.751	237.211
$^{29}\text{Si}(n,p)^{29}\text{Al}$	1273	1121	1.485	1.968
	2028	33.5	0.0444	0.0588
	2426	59.6	0.0790	0.105
$^{30}\text{Si}(n,\alpha)^{27}\text{Mg}$	843.8	344	0.456	0.427
	1014.4	133	0.176	0.165

Table 9-5 Results of sonde response model calculations for silicon in a shaly sand. The final column is the estimated number of counts per sodium density of 1 mg/cm^3 for these logging conditions.

9.2.2 Response matrix and synthetic data set

A response matrix may be constructed using the sensitivities determined in the previous section. It is a sparse 14×4 matrix (equation 9-2) that relates partial elemental density ρ in g/cm^3 to the photopeak counts C for the specific logging conditions. Entries in the matrix are simply the values from the final columns of the preceding Tables 9-2 through 9-5, which have been multiplied by 1000 because of the change in units from mg/cm^3 to g/cm^3 . Thermal neutron responses entered in the matrix are printed in bold, italicized characters.

$$\begin{matrix} C_{1369} \\ C_{2754} \\ C_{844} \\ C_{1014} \\ C_{439} \\ C_{391} \\ C_{586} \\ C_{975} \\ C_{1611} \\ C_{1633} \\ C_{1779} \\ C_{1273} \\ C_{2028} \\ C_{2426} \end{matrix} = \begin{bmatrix} 550 & 2072 & 401 & 0 \\ 475 & 2014 & 349 & 0 \\ 979 & 0 & 19416 & 427 \\ 393 & 0 & 7473 & 165 \\ 4249 & 40804 & 0 & 0 \\ 1945 & 0 & 0 & 0 \\ 1953 & 0 & 0 & 0 \\ 1892 & 0 & 0 & 0 \\ 1183 & 0 & 0 & 0 \\ 0 & 150943 & 0 & 0 \\ 0 & 0 & 226465 & 237211 \\ 0 & 0 & 0 & 1968 \\ 0 & 0 & 0 & 58.8 \\ 0 & 0 & 0 & 105 \end{bmatrix} \times 10^{-9} \begin{bmatrix} \rho_{Mg} \\ \rho_{Na} \\ \rho_{Al} \\ \rho_{Si} \end{bmatrix} \quad 9-2$$

Using this response matrix, synthetic data sets containing the noise associated with counting statistics have been generated for the shaly sand. The level of noise entered into the data assumes an insignificant uncertainty in the Compton continuum. One thousand synthetic data points were generated, using a 183 cm source-to-detector spacing, 183 m/hr logging speed, 15.24 cm (six inch) depth intervals with three-level averaging, and two different neutron generator output intensities. Weighted least squares solutions of the 1000 data points, performed in the same manner as in section 3.1.2, result in precisions that are listed in Table 9-6.

	Mg	Na	Al	Si
Partial density mg/cm ³	13.6	380	121	755
Relative error (%), 1 X 10 ⁹ neutrons/second	19.3 %	1.9 %	3.0 %	0.6 %
Relative error (%), 1 X 10 ¹⁰ neutrons/second	5.2 %	0.6 %	0.9 %	0.2 %

Table 9-6 A synthetic data set was used to examine the statistical precision attainable with a sonde, using the response matrix of equation 9-2 and a weighted least squares approach. Downhole generators today are capable of 1 X 10⁹ neutrons per second.

Reaction	Gamma-ray energy (keV)	$C_{\text{mod_dol}} (\times 10^9)$	$\frac{C_{\text{mod_dol}} (\times 10^9)}{\rho_{\text{Mg}}}$	$\frac{C_{\text{log_dol}}}{\rho_{\text{Mg}}}$
$^{24}\text{Mg}(n,p)^{24}\text{Na}$	1368.6	16959	50.18	0.521
	2754.1	14518	42.95	0.446
$^{25}\text{Mg}(n,p)^{25}\text{Na}$	390.7	105.1	0.311	1.732
	585.9	118.1	0.349	1.946
	975.2	111.1	0.329	1.831
	1611.9	71.4	0.211	1.176
$^{26}\text{Mg}(n,\alpha)^{23}\text{Ne}$	439	214.3	0.634	4.140
$^{26}\text{Mg}(n,\gamma)^{27}\text{Mg}$	843.8	514.3	1.522	1.426
	1014.4	197.0	0.583	0.546

Table 9-2 Results of sonde response model calculations for magnesium in a dolomite. The third column, $C_{\text{mod_ss}} (\times 10^9)$, contains the photopeak counts, collected over all time, per neutron emitted at time t_0 . The fourth column contains the photopeak counts divided by the density (mg/cm^3) of magnesium in the rock. The final column contains the number of counts that would be attained, per magnesium density of $1 \text{ mg}/\text{cm}^3$, if logging proceeded using the conditions described earlier.

9.3 Magnesium detection in a carbonate

A series of modeling runs was performed for a 15 pu dolomite with the sonde eccentric in a 20 cm diameter wellbore. Fresh water was used in the pore space and the wellbore. The modeled number of counts in the photopeak per source neutron for each of the magnesium reactions, $C_{\text{mod_dolo}} (\times 10^9)$, is included in Table 9-7. These numbers are adjusted by the factors found in chapter 8 to be the amount that the calculated response integrals differed from measurements in the water tank. The adjusted count rates are used to estimate the count rates $C_{\text{log_dolo}}$ that can actually be achieved in a continuous log. A synthetic data set was also generated for the dolomite to determine the attainable precision, which is listed in Table 9-8.

	Mg
Partial density mg/cm ³	338
Relative error (%), 1 X 10 ⁹ neutrons/second	2.4 %
Relative error (%), 1 X 10 ¹⁰ neutrons/second	0.7 %

Table 9-8 A synthetic data set was used to examine the statistical precision attainable with a sonde for two neutron generator output intensities.

9.4 Environmental effects

Several modeling runs were performed to assess the scope of borehole and formation environmental effects on the neutron activation measurement. Only the response to magnesium was studied, but responses to other elements should have very similar effects.

9.4.1 Borehole conditions

For the borehole group of environmental conditions, a 15 pu dolomite, (Ca,Mg)CO₃, with fresh water in the pore space and bulk density of 2.590 g/cm³ was used for all cases. The borehole conditions and tool position were changed, as listed in Table 9-9. This set of calculations is not comprehensive enough to provide a characterization of the tool response to the borehole environment, but does provide useful information about the overall size of the effects.

hole diameter (cm)	borehole fluid	sonde position.
20	fresh water	eccentered
20	fresh water	centered
20	1.50 g/cm ³ mud	eccentered
20	1.50 g/cm ³ mud	centered
25	fresh water	eccentered
25	fresh water	2.5 cm standoff
25	fresh water	centered

Table 9-9 The set of models that were run to assess borehole environmental effects.

The series of plots which follows shows the results of the environmental effects calculations for each of the nine useful gamma-ray energies from magnesium activation. Along the horizontal axis of each plot, gamma-ray energies are listed, clustered according to the decaying intermediate nuclide. On each plot, the order of gamma-rays is the same. The two gamma-rays listed at the left of each plot, 1014 and 844 keV, are from the thermal neutron reaction on ^{26}Mg and have noticeably different responses than the others in most cases. All other gamma-rays derive from fast neutron reactions.

Each plot shows the change in response relative to the first condition listed in the legend. The vertical scale is the same for all graphs. Error bars have been omitted from the plots, but the relative statistical precision of each calculation was about 1%.

Figure 9-6 shows the loss in response of approximately 15% for each gamma-ray photopeak when hole diameter increases from 20 cm to 25 cm. The change does not correlate with gamma ray energy, and there is not a significant difference between gamma-rays from the thermal neutron reaction and fast reactions.

Figure 9-7 shows the small loss in gamma-ray signal when mud of density 1.5 g/cm^3 replaces water in a 20 cm borehole. The mud is weighted with hematite and kaolinite. There is a slightly larger effect on the response from the thermal neutron reaction than the fast neutron reaction.

Tool position has a very large effect on responses, in particular for the fast neutron reactions. Figure 9-8(a) shows a 50% to 60% loss of gamma-ray signal when the sonde is centered rather than eccentric in a 20 cm borehole. Centering represents a 5.4 cm standoff for the part of the sonde containing the neutron source, and a 4.5 cm standoff for the detector portion of the sonde. The loss of response is even more severe, 55% to 70%, for fast neutron reactions when the sonde is centered in a 25 cm hole, as seen in Figure 9-8(b). Standoff of 2.5 cm also has a sizable degrading effect on the response. The thermal neutron activation response is affected substantially, but only about half as much as the fast neutron response.

Figure 9-8(c) illustrates the effect of sonde centering in a 20 cm borehole containing hematite-weighted mud. There is a noticeable trend of greater signal loss with decreasing gamma ray energy, which is consistent with the spatial effect expected from centering. Gamma-rays must traverse greater distances when the sonde is centered, and the lower energy gamma-rays are attenuated more than higher energy gamma-rays. Clearly the sonde should be used eccentric.

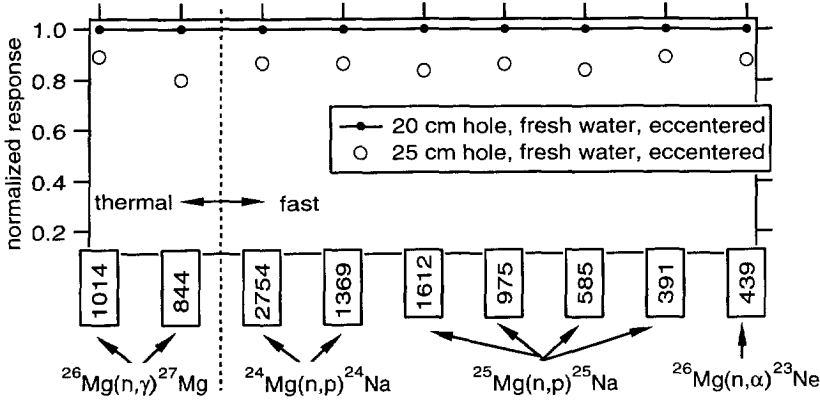


Figure 9-6 Approximately 15% of the response is lost when hole size changes from 20 cm to 25 cm.

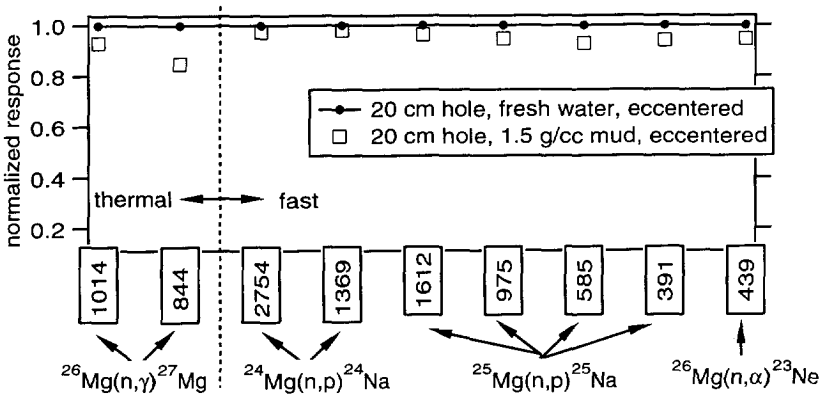


Figure 9-7 There is only a small loss of response when hematite-weighted mud replaces fresh water as the borehole fluid.

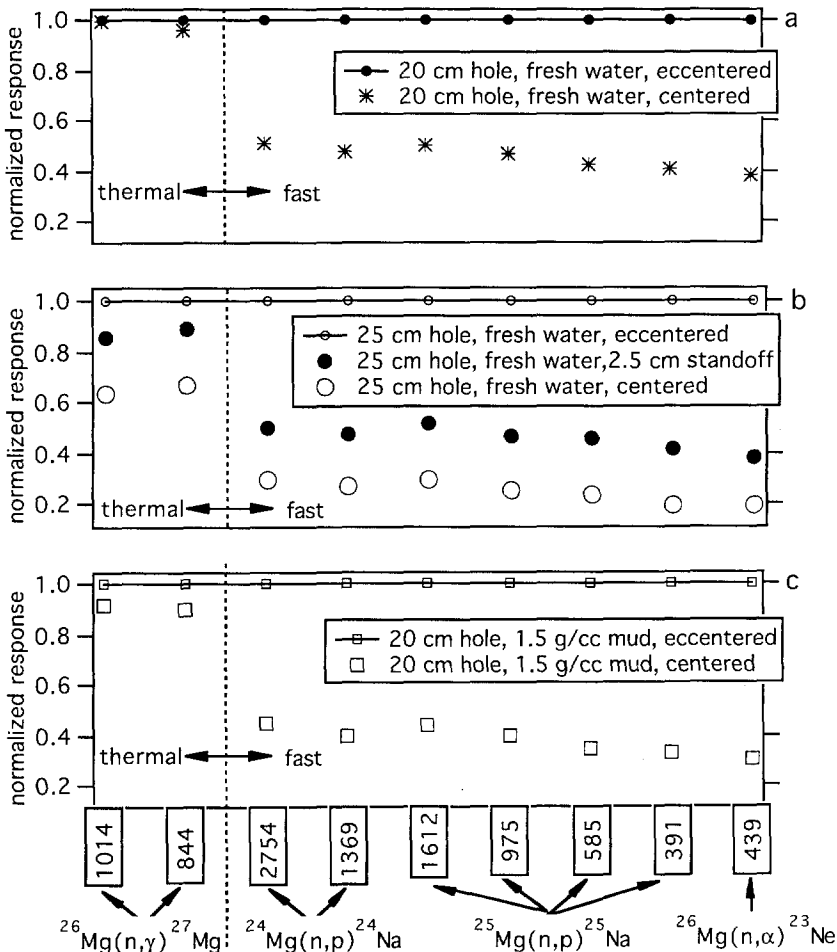


Figure 9-8 Sonde standoff and centering have a huge degrading effect on the activation response, particularly for the fast neutron reactions. The effect of centering in a 20 cm borehole filled with fresh water is shown in part (a). The effects of centering and 2.5 cm standoff in a 25 cm borehole filled with fresh water are shown in part (b). The effect of centering in a 20 cm borehole filled with hematite-weighted mud is shown in part (c).

9.4.2 Formation parameters

A series of calculations was performed to assess the effect of formation conditions on the detected magnesium signal. The conditions tested are listed in Table 9-10. Borehole conditions were held constant, at 20 cm diameter, with the sonde eccentered. Fresh water was used in the borehole, with one exception. For the case with 100 kppm salt water in the formation, saltwater was used in the borehole also.

porosity (pu)	pore water	matrix	bulk density (g/cm ³)	Mg density (g/cm ³)
15	fresh	(Ca,Mg)CO ₃	2.590	0.338
25	fresh	(Ca _{1.773} ,Mg _{0.227})CO ₃	2.310	0.0675
5	fresh	(Ca,Mg)CO ₃	2.777	0.377
15	100 kppm NaCl	(Ca,Mg)CO ₃	2.600	0.338
16	fresh	shaly sand	2.344	0.0135

Table 9-10 The set of models that were run to assess formation environmental effects.

In the following pair of graphs, the same conventions for the axes that were used in the previous section are maintained here. The responses are normalized by the partial density of magnesium in the formation, and also by using the 15 pu dolomite fresh water case as a baseline. The effect of a change in formation density and hydrogen index is illustrated in Figure 9-9. The effects on the fast neutron activation response are very small, but consistent. The 25 pu partially dolomitic limestone provides a slightly increased response per magnesium density unit, and the 5 pu dolomite has a slightly decreased response. The thermal neutron activation response is affected considerably more, in the same directions.

The effect of salt water in the pore space and borehole upon the fast neutron activation response is small (Figure 9-10), but it is severely degrading to the thermal neutron activation response. Chlorine has a large thermal neutron absorption cross section that removes many neutrons before they can be captured by magnesium or any other constituent of the formation. A similar effect is seen in the shaly sand, which contains thermal neutron absorbers gadolinium at 4.5 ppm and boron at 49 ppm. For the shaly sand, the absorber effect is partially offset by a density effect.

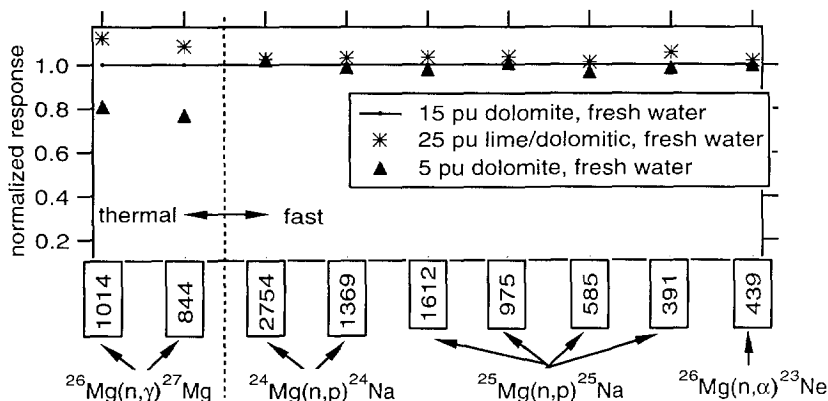


Figure 9-9 The effect of formation density and hydrogen index changes on fast neutron activation responses are small in the range tested by these calculations.

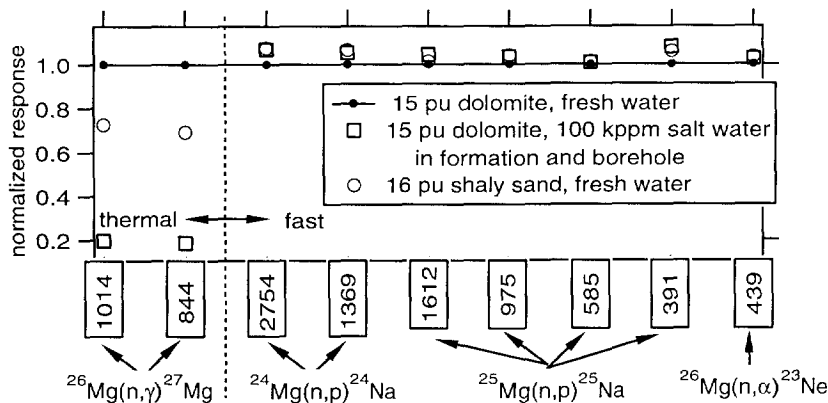


Figure 9-10 The effect of absorbers on the thermal neutron activation response is large.

9.5 Summary and conclusions

The sensitivities of a neutron activation measurement to magnesium, sodium, aluminum, and silicon in a borehole geometry have been investigated by simulating the response of a possible sonde with the Monte Carlo radiation transport code MCBEND. First, the model was used to estimate responses to mass concentrations in a typical shaly sand containing all four of the elements. Next, the sensitivity to magnesium in a carbonate was calculated. Finally, several environmental conditions were simulated to determine the scope of their effect upon an activation measurement.

9.5.1 Downhole measurement of sodium, magnesium, aluminum, and silicon in a shaly sand

The model was used to calculate photopeak intensities at fourteen gamma-ray energies resulting from the decay of seven intermediate nuclides. Several *competing reactions* are included, where the same intermediate nuclide and decay gamma-ray energies result from activations of different elements. Four of the intermediate nuclides result from competing reactions on sodium, magnesium, aluminum, and silicon atoms.

The problem of developing a technique to deal with competing reactions populating the same gamma ray peaks has been addressed in a manner to obtain the optimum precision for the resulting elemental concentrations. This may be accomplished by constructing a response matrix containing the partial photopeak contributions of each element. A measurement of photopeak intensities may then be inverted by a weighted least-squares technique to solve for elemental concentrations. The response matrix was used to generate sets of synthetic photopeak intensities, with a noise component corresponding to an assumed set of logging conditions in the shaly sand. Each set of photopeak intensities was inverted through the response matrix to obtain estimates of the elemental concentrations in the shaly sand. The spread of the inverted data is a measure of the precision attainable for the specific conditions.

Precisions attainable by a Monte Carlo model sonde in the shaly sand are acceptable for the assumed logging conditions of 600 feet per hour, six-inch sampling, three-level averaging, and a neutron output of 10^{10} neutrons per second. Magnesium density of 14 mg/cm^3 (0.58 weight percent) in the shaly sand can be determined with a relative precision of 5%. Sodium density of 38 mg/cm^3 (1.64 weight percent) and aluminum density of 121 mg/cm^3 (5.18 weight percent) can be measured with relative precisions less than 1%. Silicon density of 755 mg/cm^3 (32.2 weight percent) can be measured with a relative precision of 0.2%.

The determinations of precision contain the optimistic assumption that there is no Compton continuum beneath the photopeaks, because the model contains an idealized representation of the detector response. While initial work has characterized the basic properties of such a large volume detector, further studies should be performed to establish the complete set of actual detector properties, such as peak-to-Compton ratios. These properties could be used to establish the precision attainable with a real detector.

9.5.2 Downhole measurement of magnesium in a carbonate

The response of a possible activation sonde to magnesium in a 15 percent porosity dolomite was calculated, in a very similar manner to the preceding discussion of the shaly sand. The sonde was eccentered in a 20 cm borehole, and formation and borehole both contained fresh water. For the set of logging conditions discussed above, and using the *a priori* assumption that there is no sodium, aluminum, or silicon present, magnesium density of 338 mg/cm^3 (13.0 weight percent) can be measured with a relative precision of 0.7%.

9.5.3 Borehole environmental effects on an activation measurement

Borehole environmental effects on the activation measurements are large, and are generally larger for the fast neutron reactions than for thermal neutron reactions. This difference can be observed in Figure 9-7, where the number of 844 and 1014 keV gamma-rays, from the thermal neutron reaction $^{26}\text{Mg}(n,\gamma)^{27}\text{Mg}$, deviate from the baseline much less than the other gamma-rays. It can also be inferred from the activation maps, where the fast neutron activation exhibits a larger azimuthal variation in intensity than the slow neutron activation. The fast neutron standoff effect is large enough to degrade the statistical significance of a measurement, as well as introducing a bias into the result. Logging should therefore be performed with an eccentered sonde. The effect of standoff or centering on the thermal neutron reactions is small. Mud weight and hole size effects are not large and can be corrected.

The large standoff effect for fast neutron activation is due to scattering of fast neutrons in the borehole. Neutrons emitted into the borehole rather than the formation need to scatter perhaps only once from a hydrogen atom in the borehole to slow down below the $^{26}\text{Mg}(n,\alpha)^{23}\text{Ne}$ or other fast reaction thresholds, before even reaching the formation.

The set of calculations that was performed is by no means complete, but provides an assessment of the overall size of borehole effects on the activation measurements. If a sonde is eccentered properly and hole rugosity is low, the borehole effects should be entirely manageable. Additional calculations should be performed to determine the effect of salty mud on the measurement.

9.5.4 Formation effects on an activation measurement

Formation density, hydrogen index, salinity, and the presence of thermal neutron absorbers, as modeled in this study, have only a small effect on the signal from fast neutron activation.

The absorbers, particularly chlorine, have a large effect on thermal neutron activation. Formation water salinity has a very large degrading effect

on the number of thermal neutron reactions in the rock, because chlorine possesses a large thermal neutron absorption cross section. Similarly, the presence of other thermal neutron absorbers, such as gadolinium, samarium, and boron, reduces the number of activation gamma rays generated from other rock constituents. Concentrations of a few parts per million of these elements will have noticeable effects. A neutron decay log or other measurement of the formation capture cross section could be used to correct the response of an activation measurement for these effects. Chlorine concentration is measurable, either by prompt capture or by delayed activation through the thermal neutron reaction $^{37}\text{Cl}(n,\gamma)^{38}\text{Cl}$, and this can be used as a basis for correction of other thermal neutron measurements.

The presence of chlorine may also cause thermal neutron activation measurements to suffer statistically, as can be inferred from Figure 9-9 where the detected gamma-ray signal has fallen off by 80 percent in the presence of salt. Salt will also pose an interference with rock sodium detection, which can possibly be dealt with by use of a chlorine measurement and subsequent division of the sodium signal into salt and rock components.

In the case of magnesium, the response matrix of Equation 9-2 does not place a large reliance on the thermal reaction but there is some crosstalk of the signal to aluminum and silicon. Measurement of aluminum does rely heavily on a thermal neutron reaction, but the signal is large enough that statistical degradation can be tolerated.

Generally, the precisions attainable for the conditions of this study are very good. Systematic uncertainties due to environmental effects are of greater magnitude and concern than statistical uncertainties. These are summarized in Table 9-10.

	borehole			formation			
	Standoff	hole size	mud weight	salt	hydrogen index	density	other thermal absorbers
Thermal neutron activation	medium	medium	medium	very large	medium	small	large
Fast neutron activation	very large	medium	medium	small	small	small	small

Table 9-10 Overview of size of environmental effects on fast and thermal activation measurements.

A method has been developed to estimate the sonde responses to *any* element using the results of a brief activation experiment, bypassing the lengthy Monte Carlo calculations. The responses of a downhole activation spectrometry measurement to concentrations of twenty-four elements have been estimated using this method. A calibration factor was established by comparison of experimental results from Chapter 6 with sonde modeling results from Chapter 9 for sodium, magnesium, aluminum, and silicon. The calibration allows downhole response to be estimated for any element, using the results of an activation experiment on a mixture containing the element.

Several mixtures containing a total of 28 elements were activated in the experimental facility. The elements studied were:

F S Cl K Ca Ti V Cr Mn Fe Co Ni Cu Ga Se Br
Sr Zr Mo Ag Sn Te I Ba La Hf W Au.

These elements were chosen for study because they are geologically interesting and possess one or more favorable nuclear characteristics, such as cross section, half-life of the activated state, and branching ratio.

10.1 Method

Samples containing one or more of the 28 elements were irradiated and counted in an identical manner to the rock-forming elements as described in Chapters 4 and 5, with results reported in Chapter 6. Samples consisted of chemically pure compounds containing the elements, which were thoroughly mixed in a filler of pure calcium carbonate. The amount of compound used varied from 0.1 gram to 20 grams, depending on an estimate of what was needed to provide a reasonable gamma-ray signal. An extensive listing of the sample contents, including trace element analysis, is provided in Appendix E. Irradiations and counting intervals of several durations were used. Only short irradiations of five minute duration and subsequent counting intervals of four minutes will be reported here.

The experimental data were processed in exactly the same manner as for the experiments of Chapter 6, and a subsequent calibration factor was applied to

predict the approximate sensitivity of a borehole measurement to the element. The calibration factor is based on a comparison of experimental results and borehole modeling for sodium, magnesium, aluminum, and silicon. Experimental results from Chapter 6 were stated in terms of photopeak counts per gram of element in a fixed sample volume, and borehole modeling results from Chapter 9 were expressed as photopeak counts per elemental mass density. The ratio of results from the two different methods provides an approximate factor for predicting one from the other.

10.1.1 Derivation of calibration factor

A response matrix was generated from measurements on bottles containing the rock-forming elements sodium, magnesium, aluminum, and silicon, as explained in section 6.1.5. The response matrix equation is repeated here as equation 10-1. Bold typeface in the equation indicates a thermal neutron activation response. The response matrix relates the mass of each element in grams M in the sample to the resulting photopeak area C , per effective source neutron, if all neutrons are emitted instantaneously at a time t_0 and gamma-ray detection proceeds from $t_0 \rightarrow t_\infty$. In other words, all effects of the half-lives are removed from the response.

$$\begin{array}{c}
 C_{1369} \\
 C_{2754} \\
 C_{844} \\
 C_{1014} \\
 C_{439} \\
 C_{391} \\
 C_{586} \\
 C_{975} \\
 C_{1611} \\
 C_{1633} \\
 C_{1779} \\
 C_{1273} \\
 C_{2028} \\
 C_{2426}
 \end{array}
 =
 \begin{array}{ccccc}
 31.4 & \mathbf{78.7} & 23.3 & 0 & \\
 21.0 & \mathbf{45.6} & 13.4 & 0 & \\
 \mathbf{0.702} & 0 & 14.4 & 0.329 & \\
 \mathbf{0.269} & 0 & 5.03 & 0.110 & \\
 0.838 & 7.16 & 0 & 0 & \\
 0.447 & 0 & 0 & 0 & \\
 0.311 & 0 & 0 & 0 & \\
 0.301 & 0 & 0 & 0 & \\
 0.158 & 0 & 0 & 0 & \\
 0 & 22.1 & 0 & 0 & \\
 0 & 0 & \mathbf{25.1} & 35.0 & \\
 0 & 0 & 0 & 0.986 & \\
 0 & 0 & 0 & 0.031 & \\
 0 & 0 & 0 & 0.042 &
 \end{array}
 \times 10^{-9}
 \begin{array}{c}
 M_{Mg} \\
 M_{Na} \\
 M_{Al} \\
 M_{Si}
 \end{array}
 \tag{10-1}$$

A nearly similar response function can be constructed for the measurement of sodium, magnesium, aluminum, and silicon in a borehole situation, using the modeling results of Chapter 9 for the shaly sand. Equation 9-2 cannot be used, because it contains half-life information and assumptions of

a specific set of logging conditions. Also, the mass of each element is a meaningless idea in the borehole situation because a measurement volume is not defined. The desired function will relate elemental mass density ρ to the photopeak areas, which will be called K . The response matrix is formed from the modeled responses to the shaly sand $C_{\text{mod}_{ss}}/\rho$, listed in the fourth column of Tables 9-3 through 9-6. Entries from these tables have been used to form the response matrix of equation 10-2.

$$\begin{array}{c}
 K_{1369} \\
 K_{2754} \\
 K_{844} \\
 K_{1014} \\
 K_{439} \\
 K_{391} \\
 K_{586} \\
 K_{975} \\
 K_{1611} \\
 K_{1633} \\
 K_{1779} \\
 K_{1273} \\
 K_{2028} \\
 K_{2426}
 \end{array}
 =
 \begin{array}{ccccc}
 53015 & \mathbf{199631} & 38641 & 0 & \\
 45809 & \mathbf{194048} & 33600 & 0 & \\
 \mathbf{1044} & 0 & 20717 & 456 & \\
 \mathbf{419} & 0 & 7974 & 176 & \\
 651 & 6250 & 0 & 0 & \\
 349 & 0 & 0 & 0 & \\
 351 & 0 & 0 & 0 & \\
 340 & 0 & 0 & 0 & \\
 213 & 0 & 0 & 0 & \\
 0 & 49065 & 0 & 0 & \\
 0 & 0 & \mathbf{68501} & 71751 & \\
 0 & 0 & 0 & 1485 & \\
 0 & 0 & 0 & 44.4 & \\
 0 & 0 & 0 & 79.0 &
 \end{array}
 \times 10^{-9}
 \begin{array}{c}
 \rho_{Mg} \\
 \rho_{Na} \\
 \rho_{Al} \\
 \rho_{Si}
 \end{array}
 \quad 10-2$$

An entry-by-entry division of Equation 10-2 by Equation 10-1 will result in a matrix that can be used to predict the photopeak counts in a borehole situation from the measured photopeak counts of the experiments. The resulting expression, Equation 10-3, has matrix values that vary by factors as great as 5.5, but there is an order to the values which can be observed by plotting them against the associated gamma-ray energies, as shown in Figure 10-1. Two linear trends are labeled in the plot; one is associated with thermal neutron reactions, and the other with fast neutron reactions. The trends represent variable attenuation of gamma rays in the formation. There is very little attenuation of gamma rays between the sample and detector in the experiments. But, in the formation, and in its associated representation in the model, lower energy gamma rays are attenuated more than higher energy gamma rays.

$$\begin{bmatrix} (K/C)_{1369} \\ (K/C)_{2754} \\ (K/C)_{844} \\ (K/C)_{1014} \\ (K/C)_{439} \\ (K/C)_{391} \\ (K/C)_{586} \\ (K/C)_{975} \\ (K/C)_{1611} \\ (K/C)_{1633} \\ (K/C)_{1779} \\ (K/C)_{1273} \\ (K/C)_{2028} \\ (K/C)_{2426} \end{bmatrix} = \begin{bmatrix} 1688 & 2537 & 1658 & 0 \\ 2181 & 4255 & 2507 & 0 \\ 1487 & 0 & 1439 & 1386 \\ 1557 & 0 & 1585 & 1600 \\ 776 & 873 & 0 & 0 \\ 780 & 0 & 0 & 0 \\ 1128 & 0 & 0 & 0 \\ 1130 & 0 & 0 & 0 \\ 1348 & 0 & 0 & 0 \\ 0 & 2220 & 0 & 0 \\ 0 & 0 & 2729 & 2050 \\ 0 & 0 & 0 & 1506 \\ 0 & 0 & 0 & 1432 \\ 0 & 0 & 0 & 1881 \end{bmatrix} \begin{bmatrix} (\rho/M)_{Mg} \\ (\rho/M)_{Na} \\ (\rho/M)_{Al} \\ (\rho/M)_{Si} \end{bmatrix} \quad 10-3$$

Additionally, more variable attenuation (steeper slope) is observed for gamma rays from thermal neutron reactions than for gamma rays from fast neutron reactions because the activation sites are more dispersed (see Figures 9-2 and 9-3). By the time neutrons have thermalized, they have penetrated on average further into the formation than they were when crossing beneath the threshold for fast neutron activations. The generally higher values of the translation factor for thermal neutron reactions indicate that the experimental irradiation facility is relatively less efficient for thermal neutron reactions than fast reactions, when compared to the formation model. This was anticipated, as the experimental facility was designed to enhance the sensitivity to high energy neutron reactions.

For thermal neutron reactions, the fitted line and the statistics of data points (not shown on the graph) account for 97% of the variation in the data, based on a sum-of-squares analysis. For the fast neutron reactions, the figure drops to 72%. The remaining variation is most likely due to differences in the average depth of neutron penetration associated with each of the reactions, and due to non-statistical uncertainties of the experiments and model.

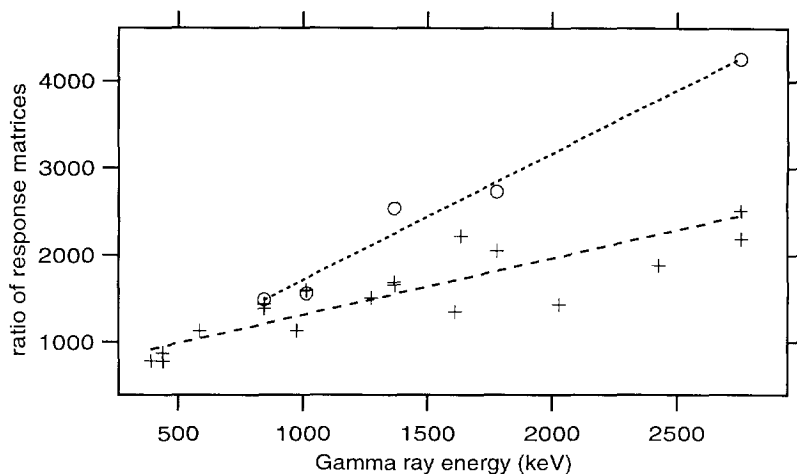


Figure 10-1 The ratio of response matrices for the experiment and the borehole model shows a strong dependence on gamma-ray energy, primarily due to variable attenuation of gamma rays in the formation. Separate trends are apparent for thermal neutron reactions and for fast neutron reactions. Gamma rays from thermal neutron reactions exhibit more variable attenuation because they originate, on average, from deeper in the formation.

The fitted lines of Figure 10-1 may be used to determine an approximate factor for translation of experimental results to a prediction of borehole measurement sensitivity. The translation factors J are given in Equation 10-3, where E is the gamma-ray energy in keV.

$$J_{Thermal} = 254 + 1.456E \quad \& \quad J_{Fast} = 661 + 0.650E \quad 10-3$$

Use of the translation factors is based on the assumption that there are no unknown factors that will cause substantial deviation from the fitted trends. Estimates of the sonde response assume a formation that is similar to the shaly sand on which the translation is based.

10.2 Results

Results are presented in a tabular form in ascending atomic number. The gamma-ray energy E in keV is listed in the first column, followed by the branching ratio b in percent. The experimental results C_{exp} are stated in exactly the same terms as those of Chapter 6, in counts per gram of element in the sample mixture. The translation factor J is calculated by Equation 10-3 using the appropriate segment of Figure 10-1 to give the estimated response of a sonde. For gamma-ray energies beyond the range of the abscissa in Figure 10-1,

an extrapolation is necessary. The estimate is then divided by 1000, so that results are stated as $K_{pred}/(\text{mg}/\text{cm}^3)$, or the response to an elemental density of 1 milligram per cubic centimeter. Then, the assumptions of 10^9 neutrons per second, 600 feet per hour logging speed, three-level averaging, six-inch sampling, and 6 feet separation of source and detector are used to calculate $C_{log}/(\text{mg}/\text{cm}^3)$ in the same manner as in Chapter 9 by Equation 9-1.

A similar calculation of the number of photopeak counts attainable in a station measurement is included as the last column, $C_{station}/(\text{mg}/\text{cm}^3)$. The conditions of the station measurement are five minutes activation time, 15 seconds to reposition the sonde, and five minutes counting time. Estimates are valid for the conditions used in the calibration, that is, the shaly sand. Environmental corrections will need to be applied as conditions change.

Rather than present these results in one massive table, they have been broken up and listed with annotations which provide the size of the gamma-ray peak resulting from a typical elemental concentration.

10.2.1 Fluorine

 $^{19}\text{F}(\text{n,p})^{19}\text{O}$

27.1 sec

E (keV)	b (%)	C_{exp} ($\times 10^9$)	F	$\frac{K_{pred}}{\text{mg}/\text{cm}^3}$	$\frac{C_{log}}{\text{mg}/\text{cm}^3}$	$\frac{C_{station}}{\text{mg}/\text{cm}^3}$
197.47	97	$20.3 \pm 9.8\%$	790	16.0	10.6	427
1357	59	$3.81 \pm 18\%$	1544	5.89	3.88	157

At the 0.1 weight percent level of fluorine in the shaly sand, a station measurement would result in 1000 counts and 370 counts in the two photopeaks.

10.2.2 Sulfur

No sulfur peaks could be found in the experiments. Sulfur was present in the barium sample (1.9 grams) and silver samples (0.4 grams) at low concentrations.

10.2.3 Chlorine

No chlorine peaks could be found in the experiments. Chlorine was only present in the gold sample (0.2 grams).

10.2.4 Potassium



E (keV)	b (%)	C_{exp} ($\times 10^9$)	F	$\frac{K_{\text{pred}}}{\text{mg/cm}^3}$	$\frac{C_{\text{log}}}{\text{mg/cm}^3}$	$\frac{C_{\text{station}}}{\text{mg/cm}^3}$
1293.7	6.7	$3.21 \pm 24\%$	1503	4.83	0.041	44.2

At 2 weight percent potassium in the shaly sand, a station measurement would yield approximately 2000 counts in this photopeak. By contrast, a five minute accumulation of the gamma rays from the natural activity of ^{40}K would result in about five times this many counts.

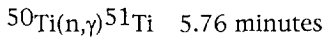
10.2.5 Calcium



E (keV)	b (%)	C_{exp} ($\times 10^9$)	F	$\frac{K_{\text{pred}}}{\text{mg/cm}^3}$	$\frac{C_{\text{log}}}{\text{mg/cm}^3}$	$\frac{C_{\text{station}}}{\text{mg/cm}^3}$
3084.4	91.7	$0.100 \pm 11\%$	4745	0.476	0.048	37.9

In a limestone of 15 pu, the calcium density is 0.92 grams per cubic centimeter. If environmental effects were the same in this limestone as they are in the shaly sand, a logging measurement would result in only 44 counts. The station measurement would yield 35000 counts.

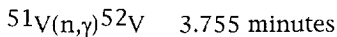
10.2.6 Titanium



E (keV)	b (%)	C_{exp} ($\times 10^9$)	F	$\frac{K_{\text{pred}}}{\text{mg/cm}^3}$	$\frac{C_{\text{log}}}{\text{mg/cm}^3}$	$\frac{C_{\text{station}}}{\text{mg/cm}^3}$
320	95	$2.09 \pm 16\%$	720	1.50	0.223	148

At a concentration of 1 weight percent in the shaly sand, a logging measurement would yield 5 counts, and a station measurement would yield 3500 counts.

10.2.7 Vanadium



E (keV)	b (%)	C_{exp} ($\times 10^9$)	F	$\frac{K_{\text{pred}}}{\text{mg/cm}^3}$	$\frac{C_{\text{log}}}{\text{mg/cm}^3}$	$\frac{C_{\text{station}}}{\text{mg/cm}^3}$
1434.2	99.75	$436 \pm 4.0\%$	2342	1020	221	115000

At a typical concentration of 200 ppm a logging measurement in the shaly sand would yield 104 counts, and a station measurement would yield 54000 counts. There is a competing reaction with manganese.

10.2.8 Chromium

No chromium peaks could be found in the experiments.

10.2.9 Manganese

$^{55}\text{Mn}(n,\alpha)^{52}\text{V}$ 3.755 minutes

E (keV)	b (%)	C_{exp} ($\times 10^9$)	F	$\frac{K_{\text{pred}}}{\text{mg/cm}^3}$	$\frac{C_{\text{log}}}{\text{mg/cm}^3}$	$\frac{C_{\text{station}}}{\text{mg/cm}^3}$
1434.2	99.75	$4.293 \pm 22\%$	1594	6.84	1.49	771

At a typical manganese concentration of 0.04 weight percent in the shaly sand, a station measurement would result in 720 counts, about 1/75 the typical number of counts from the competing reaction on vanadium.

$^{55}\text{Mn}(n,\gamma)^{56}\text{Mn}$ 2.582 hours

846.6	99	$1327 \pm 5\%$	1486	1970	11.9	12900
1811.2	30	$208 \pm 13\%$	2891	601	3.62	3940
2112	15.5	$102 \pm 19\%$	3329	340	2.04	2230

The largest of these photopeaks would yield 12,000 counts in a station measurement at 0.04 weight percent manganese. There is a competing reaction from iron.

10.2.10 Iron

$^{56}\text{Fe}(n,p)^{56}\text{Mn}$ 2.582 hours

E (keV)	b (%)	C_{exp} ($\times 10^9$)	F	$\frac{K_{\text{pred}}}{\text{mg/cm}^3}$	$\frac{C_{\text{log}}}{\text{mg/cm}^3}$	$\frac{C_{\text{station}}}{\text{mg/cm}^3}$
846.6	99	$15.5 \pm 9\%$	1212	18.8	0.113	123
1811.2	30	$3.06 \pm 18\%$	1839	5.64	0.034	36.9
2112	15.5	$1.42 \pm 25\%$	2035	2.89	0.017	18.9

At an iron concentration of 2 weight percent, the 846.6 keV photopeak would yield 6000 counts in a station measurement.

10.2.11 Cobalt

$^{59}\text{Co}(n,\gamma)^{60}\text{Co}(m)$ 10.48 minutes

E (keV)	b (%)	C_{exp} ($\times 10^9$)	F	$\frac{K_{\text{pred}}}{\text{mg/cm}^3}$	$\frac{C_{\text{log}}}{\text{mg/cm}^3}$	$\frac{C_{\text{station}}}{\text{mg/cm}^3}$
58.6	2.1	$88.7 \pm 3\%$	339	30.1	2.55	2130

At 0.1 weight percent cobalt, a station measurement would result in 5000 counts in this photopeak.

10.2.12 Nickel

No nickel peaks could be found in the experiments. There were 2.4 grams of nickel in the sample.

10.2.13 Copper

$^{65}\text{Cu}(n,\gamma)^{66}\text{Cu}$ 10.48 minutes

E (keV)	b (%)	C_{exp} ($\times 10^9$)	F	$\frac{K_{\text{pred}}}{\text{mg/cm}^3}$	$\frac{C_{\text{log}}}{\text{mg/cm}^3}$	$\frac{C_{\text{station}}}{\text{mg/cm}^3}$
1039	9	$5.11 \pm 8\%$	1767	9.03	1.50	937

At 0.1 weight percent copper, a station measurement would result in 2200 counts in this photopeak.

10.2.14 Gallium

$^{71}\text{Ga}(n,\gamma)^{72}\text{Ga}(\text{cum})$ 14.1 hours

E (keV)	b (%)	C_{exp} ($\times 10^9$)	F	$\frac{K_{\text{pred}}}{\text{mg/cm}^3}$	$\frac{C_{\text{log}}}{\text{mg/cm}^3}$	$\frac{C_{\text{station}}}{\text{mg/cm}^3}$
834	100	$159 \pm 12\%$	1468	233	0.257	285

At 200 ppm gallium, a station measurement would result in 133 counts in this photopeak.

10.2.15 Selenium

$^{76}\text{Se}(n,\gamma)^{77}\text{Se}(\text{m})$ 17.5 seconds

E (keV)	b (%)	C_{exp} ($\times 10^9$)	F	$\frac{K_{\text{pred}}}{\text{mg/cm}^3}$	$\frac{C_{\text{log}}}{\text{mg/cm}^3}$	$\frac{C_{\text{station}}}{\text{mg/cm}^3}$
161.9	59.5	$141 \pm 2.6\%$	489	69.1	37.7	962

Selenium concentration of 200 ppm would result in 450 counts in the 161.9 keV photopeak

$^{78}\text{Se}(n,\gamma)^{79}\text{Se}(\text{m})$ 3.89 minutes

95.7	10	$10.9 \pm 8.6\%$	393	4.28	0.901	479
------	----	------------------	-----	------	-------	-----

$^{80}\text{Se}(n,\gamma)^{81}\text{Se}(\text{m})$ 57.3 minutes

103	8	$3.02 \pm 15.6\%$	404	1.22	0.020	20.8
-----	---	-------------------	-----	------	-------	------

10.2.16 Bromine $^{79}\text{Br}(n,\gamma)^{80}\text{Br}(g)$ 17.4 minutes

E (keV)	b (%)	C_{exp} ($\times 10^9$)	F	$\frac{K_{\text{pred}}}{\text{mg/cm}^3}$	$\frac{C_{\text{log}}}{\text{mg/cm}^3}$	$\frac{C_{\text{station}}}{\text{mg/cm}^3}$
617	17.2	$30.4 \pm 4.2\%$	1152	35.0	1.83	1700

 $^{81}\text{Br}(n,\alpha)^{78}\text{As}$ 1.515 hours

613.6	54	$55.6 \pm 9.0\%$	1060	58.9	0.603	648
-------	----	------------------	------	------	-------	-----

 $^{81}\text{Br}(n,\gamma)^{82}\text{Br}(m)$ 6.1 minutes

666		$9.52 \pm 15\%$	1223	11.6	1.641	1120
-----	--	-----------------	------	------	-------	------

Bromine concentration of 500 ppm would result in a station measurement reading of 2000 counts in the 617 keV photopeak, 760 counts in the 613.6 keV photopeak, and 1300 counts in the 666 keV photopeak.

10.2.17 Strontium $^{86}\text{Sr}(n,\gamma)^{87}\text{Sr}(m)$ $^{87}\text{Sr}(n,n')^{87}\text{Sr}(m)$ $^{88}\text{Sr}(n,2n)^{87}\text{Sr}(m)$ 2.81 hours

E (keV)	b (%)	C_{exp} ($\times 10^9$)	F	$\frac{K_{\text{pred}}}{\text{mg/cm}^3}$	$\frac{C_{\text{log}}}{\text{mg/cm}^3}$	$\frac{C_{\text{station}}}{\text{mg/cm}^3}$
388	83	$21.4 \pm 24\%$	819	17.5	0.097	106

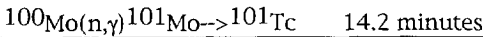
At a typical concentration of 200 ppm, 50 counts would appear in the 388 keV photopeak during a station measurement.

10.2.18 Zirconium $^{96}\text{Zr}(n,\alpha)^{93}\text{Sr}(m)$ 7.5 minutes

E (keV)	b (%)	C_{exp} ($\times 10^9$)	F	$\frac{K_{\text{pred}}}{\text{mg/cm}^3}$	$\frac{C_{\text{log}}}{\text{mg/cm}^3}$	$\frac{C_{\text{station}}}{\text{mg/cm}^3}$
590.9	74	$3.49 \pm 6.5\%$	1046	3.65	0.419	314

At a concentration of 200 ppm, 150 counts would appear in the 590.9 keV photopeak during a station measurement.

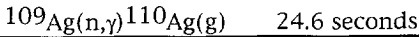
10.2.19 Molybdenum



E (keV)	b (%)	C_{exp} ($\times 10^9$)	F	$\frac{K_{\text{pred}}}{\text{mg/cm}^3}$	$\frac{C_{\text{log}}}{\text{mg/cm}^3}$	$\frac{C_{\text{station}}}{\text{mg/cm}^3}$
306.9	82.8	$1.38 \pm 27\%$	701	0.965	0.061	54.9

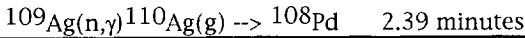
At a molybdenum concentration of 0.1 weight percent, 130 counts would appear in the 388 keV photopeak during a station measurement.

10.2.20 Silver



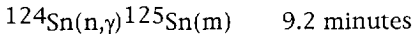
E (keV)	b (%)	C_{exp} ($\times 10^9$)	F	$\frac{K_{\text{pred}}}{\text{mg/cm}^3}$	$\frac{C_{\text{log}}}{\text{mg/cm}^3}$	$\frac{C_{\text{station}}}{\text{mg/cm}^3}$
657.7	4.5	$135 \pm 3.0\%$	1211	163	105	3790

With silver present at the 100 ppm level, 900 counts could be obtained in the 657.7 keV photopeak during a station measurement.

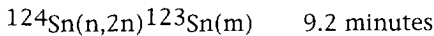
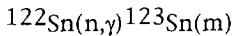


617	2.3	$3.17 \pm 12\%$	1152	3.65	1.15	412
-----	-----	-----------------	------	------	------	-----

10.2.21 Tin



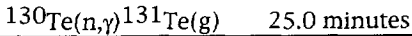
E (keV)	b (%)	C_{exp} ($\times 10^9$)	F	$\frac{K_{\text{pred}}}{\text{mg/cm}^3}$	$\frac{C_{\text{log}}}{\text{mg/cm}^3}$	$\frac{C_{\text{station}}}{\text{mg/cm}^3}$
332	99	$2.16 \pm 12.6\%$	737	1.59	0.153	123



159.7	23.4	$3.79 \pm 30\%$	486	1.84	1.12	102
-------	------	-----------------	-----	------	------	-----

With tin present at the 500 ppm level, 140 counts could be obtained in the 332 keV photopeak and 120 counts could be obtained in the 159.7 keV photopeak during a station measurement.

10.2.22 Tellurium



E (keV)	b (%)	C_{exp} ($\times 10^9$)	F	$\frac{K_{pred}}{mg/cm^3}$	$\frac{C_{log}}{mg/cm^3}$	$\frac{C_{station}}{mg/cm^3}$
149.8	86.7	$0.885 \pm 21\%$	472	0.418	0.015	15.0

The sensitivity to tellurium is very low. To measure tellurium at the 10% precision level, assuming no Compton continuum, the concentration would need to be 0.3 weight percent in the shaly sand.

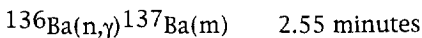
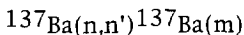
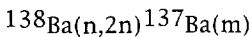
10.2.23 Iodine



E (keV)	b (%)	C_{exp} ($\times 10^9$)	F	$\frac{K_{pred}}{mg/cm^3}$	$\frac{C_{log}}{mg/cm^3}$	$\frac{C_{station}}{mg/cm^3}$
442.9	17.5	$72.1 \pm 5.6\%$	899	64.8	2.38	2330
526.6	1.7	$5.33 \pm 23\%$	1020	5.44	0.199	196

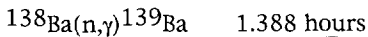
At an iodine concentration of 100 ppm, the number of counts in the 442.9 keV photopeak from a station measurement would be 550.

10.2.24 Barium



E (keV)	b (%)	C_{exp} ($\times 10^9$)	F	$\frac{K_{pred}}{mg/cm^3}$	$\frac{C_{log}}{mg/cm^3}$	$\frac{C_{station}}{mg/cm^3}$
661.6	84.6	$35.3 \pm 1.5\%$	1092	38.6	11.5	4390

At the 500 ppm barium level, there would be approximately 5000 counts in the 661.6 keV photopeak from a five minute station measurement.



165.8	22.6	$6.02 \pm 16\%$	495	2.98	0.033	35.6
-------	------	-----------------	-----	------	-------	------

10.2.25 Lanthanum

 $^{139}\text{La}(n,\gamma)^{140}\text{La}$ 40.23 hour

E (keV)	b (%)	C_{exp} ($\times 10^9$)	F	$\frac{K_{\text{pred}}}{\text{mg/cm}^3}$	$\frac{C_{\text{log}}}{\text{mg/cm}^3}$	$\frac{C_{\text{station}}}{\text{mg/cm}^3}$
1596.2	95.5	265.8 ± 13.7	2578	685	0.266	295
487	46.1	201.3 ± 18.6	963	194	0.075	83.4
328.8	20.6	122.1 ± 20.6	732	89.4	0.035	38.5
815.8	22.3	88.76 ± 22.3	1442	128	0.050	55.0

Lanthanum at the 100 ppm level would result in 70 photopeak counts from a station measurement.

10.2.26 Hafnium

 $^{178}\text{Hf}(n,\gamma)^{179}\text{Hf}(m1)$ 18.7 seconds

E (keV)	b (%)	C_{exp} ($\times 10^9$)	F	$\frac{K_{\text{pred}}}{\text{mg/cm}^3}$	$\frac{C_{\text{log}}}{\text{mg/cm}^3}$	$\frac{C_{\text{station}}}{\text{mg/cm}^3}$
215.5	82	$1154 \pm 2.4\%$	567	655	374	110100
55.7	49	$320.4 \pm 5.8\%$	335	107	61.3	1660
63.5	13	$91.5 \pm 14\%$	346	31.7	18.1	49

Hafnium present in the shaly sand at the 100 ppm level would result in 26000 counts in the 215.5 keV photopeak during a station measurement. At this concentration, a continuous measurement would have 90 counts in the photopeak.

10.2.27 Tungsten

 $^{186}\text{W}(n,\gamma)^{187}\text{W}$ 23.9 hours

E (keV)	b (%)	C_{exp} ($\times 10^9$)	F	$\frac{K_{\text{pred}}}{\text{mg/cm}^3}$	$\frac{C_{\text{log}}}{\text{mg/cm}^3}$	$\frac{C_{\text{station}}}{\text{mg/cm}^3}$
685.7	32	$118 \pm 17\%$	1252	148	0.096	107
478.5	26.6	$118 \pm 18\%$	950	112	0.073	80.9

Tungsten present at the 200 ppm level would yield only 25 and 20 counts in the two photopeaks during a station measurement.

10.2.28 Gold

$^{197}\text{Au}(n,\gamma)^{198}\text{Au}$ 2.695 days

E (keV)	b (%)	C_{exp} ($\times 10^9$)	F	$\frac{K_{\text{pred}}}{\text{mg/cm}^3}$	$\frac{C_{\text{log}}}{\text{mg/cm}^3}$	$\frac{C_{\text{station}}}{\text{mg/cm}^3}$
411	98.8	$5604 \pm 27\%$	0.852	4770	1.15	1280

A station measurement would yield 280 photopeak counts if gold were present at the 100 ppm level.

10.3 Summary and Conclusions

10.3.1 A method to predict the sonde response to other elements

Modeling calculations of the sonde response in a formation require several days of computer time for each element. By contrast, a sample containing several elements may be prepared, activated, and counted in a few hours. Repeat measurements, after setting the sample aside for at least ten half-lives of the nuclides, require only about fifteen minutes. A method has been developed to predict the response of the sonde to any element, using the results of a laboratory activation measurement on a small sample of the element.

A forward response matrix was constructed from the *modeling* calculations of a sonde response to sodium, magnesium, aluminum, and silicon, as described in section 11.2. An analogous forward response matrix was determined using the *experimental* results on the four elements. The ratio of the two response matrices was used in conjunction with a gamma-ray attenuation correction to develop two calibration factors for translating experimental results to estimates of a sonde response. One calibration factor is for thermal neutron activation, and the other is for fast neutron activation.

A shaly sand was used as the basis for the estimates, therefore the predicted elemental responses are valid only for a formation and borehole composition and geometry with similar gross properties. However, sonde responses to magnesium were calculated for ten additional geometries. The magnesium response alone may be sufficient to generate a gamma-ray attenuation correction for these other configurations. This remains to be seen.

10.3.2 Estimation of the sonde response to other elements

Several mixtures containing a total of twenty-eight additional elements were activated for five minutes and counted, resulting in measurable decay gamma-ray intensities and prediction of the sonde response for twenty-four of the elements.

Simulated logging responses were calculated for the twenty-four elements, using an assumed set of conditions for continuous logging and for stationary measurements. Only two of the 24 elements studied, vanadium and hafnium, have large enough activation responses to be measured in a continuous log, at the concentrations in which they normally occur, and using the logging conditions of 600 feet per hour, six feet of separation between source and detector, six-inch sampling, three-level averaging, and a generator output intensity of 10^9 neutrons per second. Five minute station measurements, on the other hand, result in significant responses for most of the elements.

Calculations of the attainable precisions and the limits of detection using the responses presented in the preceding section must take into account the background, or Compton continuum, under the photopeaks. The effect of the continuum on the statistics of peak areas can be substantial. Recent studies have been carried out to characterize and use the Compton continuum as a reproducible and meaningful feature of the germanium pulse height spectrum [62]. The size and effect of the continuum vary substantially, depending on the gross lithology. In sedimentary rocks, the continuum is much larger for activation logging in a sandstone than in a carbonate.

10.3.3 Limits of the measurement system

An obvious way to improve the responses, and conceivably to enable continuous logging of more elemental concentrations, is to increase the neutron generator output intensity. The detector count rates will increase proportionally, but there will be a tradeoff due to increased detector dead time. Excessive detector dead time will cause systematic biasing of measurements.

A few calculations will reveal the extent of the problem. The total count rate of all photopeak and continuum counts in the detector at the assumed logging speed can be extracted from the modeling calculations. In the shaly sand for which the model was run, and for 10^9 neutrons per second emitted from the generator, the total modeled count rate is 2500 counts per second. The dead time of the detector and multichannel analyzer for each event was estimated in section 4.1.5 to be 20 microseconds. This corresponds to a measurable rate of 2380 counts per second, or 4.8% dead-time losses. If the neutron intensity could be increased by a factor of 10, the measurable rate would be 16670 out of 25000 "true" counts per second, or 33% losses due to dead time, an unacceptable situation. The marginal loss at this rate is excessive; an average of 2.25 additional "true" counts are required for one count to be measured.

Another tradeoff exists between the system dead time per event and the energy resolution. Faster amplifier shaping times will result in a loss of energy resolution but permit higher throughput. The pulse width can be reduced so that system dead time for an event is 10 microseconds, which is approaching the practical limit for a Wilkinson analog-to-digital converter typically used with germanium. Energy resolution measured for this condition is still less than 2.5 keV at 1333 keV. The measurable rate would be 20000 out of 25000 "true" counts per second, or 20% losses due to dead time, which is within the range of commonly accepted practices. The marginal loss is lowered so that an average of 1.56 additional "true" counts are required for one count to be measured. This situation of 25000 true counts per second and 20% dead time losses represents the throughput that would be achieved if a downhole accelerator could generate 10^{10} neutrons per second, and is an inherent limit of the measurement system using a Wilkinson ADC. A multi-channel analyzer based on a flash ADC could be used to extend the limits of acceptable count rates and reduce dead-time losses. Faster shaping times of the detector signal may be used without significant loss of energy resolution, so that pulse widths and system dead times of only one or two microseconds can be accomplished.

To assess the possibility of measuring more elemental concentrations than can now be achieved with borehole logging measurements, a first step is to investigate the adequacy of existing high energy neutron activation cross section compilations. Neutron activation measurements on Na, Mg, Al, and Si compounds were used to assess these libraries. The experiments were performed under neutron flux conditions similar to those that would exist in a borehole environment, with a neutron generator in a water tank. The compounds were exposed to a continuous energy distribution of neutrons, permitting fast and thermal neutron activation to occur. Counting of the delayed gamma rays was done with a large germanium spectrometer. Calculations of the neutron activation and gamma-ray counting were performed using the Monte Carlo radiation transport program MCBEND, its associated cross section libraries, and a computerized representation of the experimental geometry and conditions.

Calculations differed significantly from measurements for two fast reactions on magnesium. The $^{26}\text{Mg}(n,\alpha)^{23}\text{Ne}$ reaction cross sections are too optimistic when used to compute the response function integral in the particular mixed flux environment used in this study, requiring a correction of 0.60 ± 0.10 . Similarly, the response function integral calculated in the water tank from $^{25}\text{Mg}(n,p)^{25}\text{Na}$ cross sections must be boosted by 1.44 ± 0.22 to agree with measurements. It must be pointed out that comparisons of this sort are based on the total activation response for a reaction over all neutron energies, and cannot be used to assess the reaction cross section at any one energy. Also, strictly speaking, the results are valid only for a region in which the spatial and energy distribution of the neutron flux is similar to that of the studied conditions.

Geometry of a possible downhole activation sonde were entered into the MCBEND modeling code to assess sonde response to the rock-forming elements Na, Mg, Al, and Si. Activation of these four elements includes several competing reactions, where the same intermediate nuclide and decay gamma-ray energies result from activations of different elements. A technique developed to deal with the competing reactions utilizes a response matrix containing the partial photopeak contributions of each element. Subsequently, a measurement of photopeak intensities may be inverted by a weighted least-squares technique to

solve for elemental concentrations. The results indicated that Mg density of 14 mg/cm³ in a typical shaly sand can be determined with a relative precision of 5%, and Na, Al, and Si densities can be measured to 1% or better. Magnesium density of 338 mg/cm³ in a 15 percent porosity dolomite can be measured to better than 1%.

Modeling calculations of the sonde response were performed for varying borehole and formation conditions. Sonde standoff causes serious count rate degradation for the fast neutron activation reactions. Logging should therefore be performed with an eccentric sonde. Other borehole effects are minor and can be corrected. Formation water salinity or the presence of other thermal neutron absorbers has a deleterious effect on thermal neutron activation response. A neutron decay log could be used to correct the response of an activation measurement for these effects. However, there will also be significant statistical degradation when absorbers are present. Other formation conditions have a minor effect on the signal from fast neutron activation.

An additional outcome of the experiments and sonde model is the development of a formalism to relate the results of laboratory measurements on small samples to what would be obtained in a borehole measurement. Calibrations for translating experimental results to estimates of a sonde response for any element were developed, separately for thermal neutron activation and fast neutron activation.

Several mixtures containing a total of twenty-four additional elements were activated and counted. Logging responses were calculated for the twenty-four elements, using an assumed set of conditions for continuous logging and for stationary measurements. Many additional elemental concentrations can be measured by stationary logging, and a few, most notably vanadium and hafnium, are likely to be detected in a continuous measurement.

References

- 1 Howell, L. G. and A. Frosch (1939) Gamma-ray well logging. *Geophysics* **4**, 106-114.
- 2 Wahl, J. S., J. Tittman, C. W. Johnstone, and R. P. Alger (1964) The dual spacing formation density log. *Journal of Petroleum Technology* **16**, 1411-1416.
- 3 Ellis, D. V., C. Flaum, C. Roulet, E. Marienbach, and B. Seeman (1983) The lithodensity tool calibration. *Tech. Symp. Soc. Pet. Eng.*, San Francisco, Paper SPE12048. Soc. Pet. Eng, Richardson, Texas.
- 4 Ellis, D. V., (1986) Neutron porosity devices, what do they measure? *First Break* **4**(3), 11-17.
- 5 Serra, O., J. Baldwin, and J. Quirein (1980) Theory, interpretation and practical applications of natural gamma ray spectroscopy. *SPWLA 21st Annual Logging Symposium*, Houston, Paper Q. Soc. Prof. Well Log Anal.
- 6 Steinman, D. K., R. A. Adolph, M. Mahdavi, E. Marienbach, W. E. Preeg, And P. D. Wraight, (1986) Dual-burst thermal decay time logging principles. *Tech. Symp. Soc. Pet. Eng.*, New Orleans, Paper SPE15437. Soc. Pet. Eng, Richardson, Texas.
- 7 Lock, G. A. and W. A. Hoyer (1974) Carbon/Oxygen (C/O) log: use and interpretation. *Journal of Petroleum Technology* **26**, 1044-1054.
- 8 Hertzog, R. C. (1978) Laboratory and Field Evaluation of an Inelastic-Neutron Scattering and Capture-Gamma Ray Spectroscopy Tool. *SPE 53rd Annu.Tech.Conf.* Paper SPE 7430, SPE of AIME, 1978.
- 9 Hertzog, R. C., L. Colson, B. Seeman, M. O'Brien, H. Scott, D. McKeon, P. Wraight, J. A. Grau, J. S. Schweitzer, and M. M. Herron (1987) Geochemical logging with spectrometry tools. *Tech. Symp. Soc. Pet. Eng.*, Dallas, SPE paper 16792. Soc. Pet. Eng, Richardson, Texas.
- 10 Scott, H. D. and M. P. Smith, (1973) The aluminum activation log, *Transactions of Fourteenth Society of Professional Well Log Analysts Annual Meeting*, Houston, Texas. Soc. Prof. Well Log Anal.
- 11 Herron, S. L. (1995) private communication of work in progress.
- 12 Anderson, R. ed. (1990) Wireline Logging Manual of the Ocean Drilling Program, Lamont-Doherty Borehole Research Group, New York.
- 13 Grau, J. A., D. V. Ellis, M. M. Herron, J. S. Schweitzer (1987) Geochemical logging in the Siljan Ring, *Third International Symposium on Observation of the Continental Crust through Drilling* ("Deep Drilling in Crystalline Rock"), Sweden.
- 14 Grau, J. A., J. S. Schweitzer, J. K. Draxler, H. Gatto, H. Lauterjung (1992) Elemental logging in the KTB Pilot Hole : 1. NaI - based spectrometry, Submitted to *IEEE 2nd Topical Meeting on Industrial Radiation and Radiosotope Measurement Applications*, Raleigh, N. C.
- 15 Herron, M. M. and S. L. Herron (1990) Geological applications of geochemical well logging, in *Geological Applications of Wireline Logs*, A. Hurst, M.A. Lovell, A. C. Morton, eds., 165-176, Geological Publishing House of London.
- 16 Herron, M. M., (1986) Mineralogy from geochemical well logging. *Clays and Clay Mineralogy* **34**, 204-213.
- 17 Herron, M. M. (1987) Future applications of elemental concentrations from geophysical logging. *Nuclear Geophysics* **1**, 197-211.

- 18 Hastings, A. F. (1990) Log derived elemental concentrations to improve the accuracy of fluid saturations determined from well logs. *Nuclear Geophysics* 4, 305-319.
- 19 Hertzog, R. C. , P. D. Soran, and J. S. Schweitzer (1987) Detection of Na, Mg, Al, and Si in wells with reactions generated by 14 MeV neutrons. *Nuclear Geophysics* 1, 243-248.
- 20 Lonnie, T. P.(1982) Mineralogic and chemical composition of marine, nonmarine, and transitional clay beds on south shore of Long Island, New York. *Journal of Sedimentary Petrology* 52, 529-536.
- 21 Ypma, P. private communication.
- 22 Parry, Susan J. (1991) Activation spectrometry in chemical analysis, Wiley, New York.
- 23 Ellis, D. V.(1987) Well Logging for Earth Scientists, Elsevier, New York.
- 24 Bradley, J. G., J. S. Schweitzer, J. A. Truax, Alan Rice, and T. A. Tombrello (1994) A Neutron activation gamma ray spectrometer for planetary surface analysis, *Proceedings of the IAA Workshop*.
- 25 Hearst, J. R. and P. H. Nelson (1985) Well logging for physical properties, McGraw-Hill, New York.
- 26 Evans, R. D. (1955) The Atomic Nucleus, McGraw-Hill, New York.
- 27 Data courtesy of Schlumberger Well Services.
- 28 Knoll, G. F. (1989) Radiation Detection and Measurement, Wiley, New York.
- 29 Frentrop, A. H. and H. Sherman (1960) *Nucleonics* 18, 72.
- 30 Shope, L. A., R. S. Berg, M. L. O'Neal, and B. E. Barnaby (1981) Operation and life of the zetatron: a small neutron generator for borehole logging, *IEEE Trans. Nuc. Sci.*, NS-28, 1696.
- 31 Foderaro, A. (1971) Neutron Interaction Theory, MIT, Cambridge, Massachusetts.
- 32 Ellis, D. V., Well Logging for Earth Scientists, Elsevier, New York, 1987.
- 33 Erdtmann, G. (1976) Neutron Activation Tables, Weinheim, New York:Verlag Chemie.
- 34 MCNP - A general purpose Monte Carlo code for neutron and photon transport, LA-7396-M (rev.) Version 2B, Los Alamos National Laboratory, 1981.
- 35 AEA Technology, MCBEND, A Monte Carlo Program for General Radiation Transport Solutions, UserGuide for Version 9A, 1994
- 36 Overwater, R.M.W. and J.E. Hoogenboom (1994) Accounting for the thermal neutron flux depression in voluminous samples for instrumental neutron activation analysis, *Nucl. Sci. & Engr.* 117, 141-157.
- 37 Bode, P. and R. M. W. Overwater (1993) Trace element determinations in very large samples; a new challenge for neutron activation analysis, *J. Radioanal Nucl. Chem* 167, 169.
- 38 Oliveira, C. and J. Salgado (1991) Analysis of fast neutron flux distributions in bulk coal by Monte Carlo simulation studies, *Nuclear Geophysics* 5, 315.
- 39 Mendenhall, W. (1987) Introduction to probability and statistics, Duxbury, Boston.
- 40 Schweitzer, J. S.,and D. V. Ellis (1988) Review of nuclear techniques in the oil industry, *IEEE Transactions on Nuclear Science* 35, 800-805.
- 41 Schweitzer, J. S. (1991) Nuclear techniques in the oil industry, *Nuclear Geophysics* 5, 65-90.
- 42 Ellis, D. V., J. S. Schweitzer, J. J. Ullo (1987) Nuclear techniques for subsurface geology, *Ann. Rev. Nucl. Part. Sci.* 37, 213-241.
- 43 Ellis, D. V. (1990) Neutron and gamma ray scattering measurements for subsurface geochemistry, *Science* 250, 82-87.
- 44 Schweitzer, J. S. and C. A. Peterson (1990) Logging with a germanium spectrometer, *KTB Report 90-6a*, 441-449.
- 45 Schweitzer, J. S. (1991) Developments in elemental concentration logging and applications, *IEEE Transactions on Nuclear Science* 38, 497-500.

- 46 Grau, J. A., J. S. Schweitzer, D. V. Ellis, and R. C. Hertzog (1989) A geological model for gamma-ray spectroscopy logging measurements, *Nuclear Geophysics* 3, 351-359.
- 47 Hertzog, R. C. and M. M. Herron (1990) Applications of elemental measurements in geochemical logging, Schlumberger Well Services Engineering Report, presented at the 13th SPWLA European Formation Evaluation Symposium, Budapest, Hungary.
- 48 Everett, R., M. Herron, G. Pirie, J. Schweitzer, H. Edmundson (1987) Faja case study results on a single well, MFM-7S, *SPE Formation Evaluation*, 361-375.
- 49 Watson, C. personal communication.
- 50 Antkiw, S., C. R. Case, P. Albats (1986) Measurements and calculations of neutron spectra in infinite media, *Radiation Effects*, 94, 113 .
- 51 Liberman, A.D., P. Albats, and H. Pftzner, A method to determine the absolute neutron output of small D-T generators *Nucl. Instrum. Meth.* 79, 574 (1993).
- 52 Zobel, V, J eberth, U. Eberth, E. Eube, *Nucl. Instrum. Meth.* 141, 329 (1977) (radium lines)
- 53 Walford, G, and C.E.Doust (1968) *Nucl. Instrum. Meth.* 62, 353.
- 54 Walford, G, and G. E. Coote (1969) *Nucl. Instrum. Meth.* 74, 353.
- 55 R. J. Gehrke, et al. (1977) *Nucl. Instrum. Meth.* 147, 405.
- 56 R. Singh, *Nucl. Instrum. Meth.* 136, 543.
- 57 McNelles, L. A. and J. L. Campbell (1973) *Nucl. Instrum. Meth.* 109, 241
- 58 Ypma, P. private communication.
- 59 Herron, M.M. and A. Matteson (1993) Elemental composition and nuclear parameters of some common sedimentary minerals, *Nuclear Geophysics* 7, 383.
- 60 Herron, S. , private communication.
- 61 Truax, J. A. and P. Albats, (1986) Schlumberger internal document.
- 62 Thakur, A. N., J. R. Arnold, and J. S. Schweitzer (1995) Application of continuum analysis to borehole gamma-ray spectra obtained from the German Continental Deep Drilling Project, *Nuclear Geophysics* 9, 19-33.
- 63 Grau, J. A., J. S. Schweitzer, and R. C. Hertzog (1990) Statistical uncertainties of elemental concentrations extracted from neutron-induced gamma-ray measurements, *IEEE Transactions on Nuclear Science* 37(6).
- 64 Hertzog, R. C. , Soran, P. D. , and Schweitzer, J. S. (1986) Applications of cross section data for nuclear geochemical well logging, *Rad. Effects* 94, 49-52.
- 65 Herron, M. M., R. Dove, J. Grau (1992) Compensation for mineral sodium interference in Ca and Gd thermal neutron capture gamma-ray logging measurements *Nuclear Geophysics* 6, 173..
- 66 Heath, R. L. Scintillation Spectrometry, Gamma Ray Spectrum Catalog, 2nd ed., Vol.1, IDO-16880-1 (1964) (det. efficiency)
- 67 Kerr, S. A, J.A. Grau, and J. S. Schweitzer (1991) Borehole Elemental Analysis, A comparison of core and log data, IAEA, Vienna.
- 68 Clayton, C. G. and J. S. Schweitzer (1992) A review of aspects of nuclear geophysics, *Nuclear Geophysics* 6, 143.
- 69 Herron, M.M. and A. Matteson (1993) Elemental composition and nuclear parameters of some common sedimentary minerals, *Nuclear Geophysics* 7, 383.
- 70 Draxler, J. K. (1995) Personal communication
- 71 Scott, H. D., C. toller, B. A. Roscoe, R. E. Plasek, and R. A. Adolph (1991) A new compensated through-tubing carbon/oxygen tool for use in flowing wells, *Transactions SPWLA 32nd Annual Logging Symposium*, Paper MM.
- 72 Grau, J. A., PEAKFIND fortran code for spectral analysis, modified by J. A. Truax.
- 73 NASA, GANYMEDE code for analysis of pulse height spectra.
- 74 Canberra Industries, PEAK code for analysis of pulse height spectra

List of Symbols

<i>A</i>	atomic mass	
<i>C</i>	counts	
<i>D</i>	rate of decay	/sec
<i>D_∞</i>	saturation decay rate	/sec
<i>E</i>	energy	eV, keV, MeV
<i>F</i>	Fano factor	
<i>H</i>	ionization energy	eV
<i>I</i>	gamma-ray intensity	/sec/cm ²
<i>J</i>	translation factor, lab-to-borehole	counts/counts
<i>K</i>	photopeak area	
<i>L</i>	characteristic length	
<i>L_s</i>	slowing down length	cm
<i>M</i>	counts per channel	
<i>N</i>	number of particles	
<i>N_{Avo}</i>	Avogadro's number	
<i>R</i>	resolution	%
<i>s</i>	source strength	/sec
<i>S₀</i>	effective source strength at <i>t</i> ₀	/sec
S	pulse height spectrum (vector)	
<i>U</i>	pulse height	Volts or channels
<i>V</i>	volume, space	
<i>W</i>	window, counts in window	
<i>Y</i>	reaction rate	/sec
<i>Z</i>	atomic number	
<i>b</i>	branching ratio	%
<i>c</i>	speed of light	cm/sec
<i>f</i>	fraction of energy retained (chapter 2)	
<i>f</i>	spectral gate subtraction factor (chapter 3)	
<i>g</i>	saturation fraction	
<i>m₀</i>	rest mass of an electron	
<i>p</i>	probability	
<i>r</i>	radius	cm
<i>r</i>	residual of a fit	
<i>t</i>	time	sec

$t_{1/2}$	half life	sec
t_0	duration of irradiation	sec
t_n	time of counting onset in nth gate	
w	weight	
w	time bin width (chapter 5)	sec
z	final time bin	
α	element of inverted response matrix	
β	corrective element of triangular inverted response matrix	
δ	duty factor	
ϵ	efficiency	
$\epsilon_{3 \times 3}$	efficiency at 1333 keV relative to a 3" X 3" NaI	%
θ	deflection angle (0 for no deflection)	
η	number of activated nuclei	
μ	linear attenuation coefficient	cm
ρ	density	g/cm ²
ρ_b	bulk density	g/cm ²
σ	neutron cross section	barns (= 10 ⁻²⁴ cm ²)
σ	uncertainty, one standard deviation	
τ	time constant (natural)	sec, min, hour
ϕ	neutron flux	/sec/cm ²
ξ	mass attenuation coefficient	cm ² /g
ζ	element of forward response matrix	
Θ	scattering angle (0 for backscatter)	
Σ	macroscopic cross section	/cm
Ω	gamma-ray transmission efficiency	

Appendix A Effect of Detector Properties on Statistics

The example presented in section 2.7 will be used to illustrate the effects of spectral shape on the statistics of peak areas. Data from the example is reproduced here as Figure A-1. The significance of the peak area in terms of its standard deviation σ can be estimated by summing the effect of standard deviations in each channel, using the basic rule of error propagation, as follows. If y is a function of independent variables x_i where $i = 1$ to n , then the standard deviation is calculated as follows.

$$\sigma_y^2 = \sum_{i=1}^n \left(\frac{\partial y}{\partial x_i} \right)^2 \sigma_{x_i}^2 \quad \text{A-1}$$

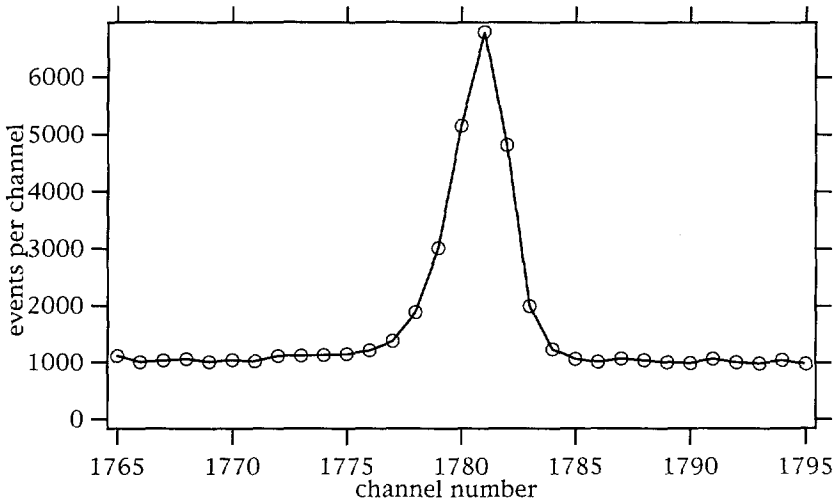


Figure A-1. Portion of a pulse height distribution with an essentially flat background component.

For a summation of thirteen channels across the region of the pulse height spectrum, minus a background level established by six flanking channels, the peak area and standard deviation are given by Equations A-1 and A-2.

$$y = \left[\sum_{i=1773}^{1785} x_i \right] - \frac{1785 - 1773 + 1}{6} \left[\sum_{i=1770}^{1772} x_i + \sum_{i=1786}^{1788} x_i \right] = 18325 \quad \text{A-2}$$

$$\sigma_y^2 = \left[\sum_{i=1773}^{1785} x_i \right] + \left(-\frac{13}{6} \right)^2 \left[\sum_{i=1770}^{1772} x_i + \sum_{i=1786}^{1788} x_i \right] = 61443 = 248^2 \quad \text{A-3}$$

Data from Figure A-1 are listed in Table A-1, in addition to the intermediate numbers from calculation of the peak area and standard deviation using the preceding equations. Examination of the equations and data in the table will reveal a few useful notions about the statistics of spectroscopy. Most of the contribution to the variance in this case, about 52%, is from the determination of the background. If we had used more channels for the background determination, the peak area would not have changed very much, except for the statistical fluctuation added by the use of additional and slightly different data. But, the variance could have been reduced substantially. Say that 13 channels had been used to determine the background (average background = 1048 counts per channel); then the approximate variance of the peak area would be

$$\sigma_y^2 = 18325 + \left(-\frac{13}{13} \right)^2 * 13 * 1048 = 45567 = 213^2 \quad \text{A-4}$$

In reality, the shape of the background and Compton continuum under the peaks, and the presence of adjacent peaks, may preclude the use of wide background windows.

A similar analysis can be used to demonstrate the improvement to be gained by using a detector with improved resolution. Suppose the detector had good enough resolution and peak definition that the peak was squeezed into 7 channels of the multi-channel analyzer, rather than 13 channels. If we still used three channels at each flank for background determination, then the approximate variance would be

$$\sigma_y^2 = 18325 + \left(-\frac{7}{6} \right)^2 * 6 * 1048 = 26884 = 164^2 \quad \text{A-5}$$

Also, it is clear that a reduction in the background is desirable. The Compton continuum can usually be reduced by using a larger detector. In the

limit of no continuum beneath the peak, the variance would be simply equal to the number of counts in the peak, or approximately

$$\sigma_y^2 = 18325 = 135^2$$

A-6

Channel number	Counts per channel	weight in peak area	addition to peak area	weight in variance	addition to variance
i	x_i	$\partial y / \partial x_i$	$x_i * \partial y / \partial x_i$	$(\partial y / \partial x_i)^2$	$x_i * (\partial y / \partial x_i)^2$
1770	1,037	-13/6	-2,247	4,694	4,867
1771	1,022	-13/6	-2,214	4,694	4,796
1772	1,112	-13/6	-2,410	4,694	5,220
1773	1,119	1	1,119	1	1,119
1774	1,133	1	1,133	1	1,133
1775	1,147	1	1,147	1	1,147
1776	1,213	1	1,213	1	1,213
1777	1,375	1	1,375	1	1,375
1778	1,889	1	1,889	1	1,889
1779	3,009	1	3,009	1	3,009
1780	5,153	1	5,153	1	5,153
1781	6,794	1	6,794	1	6,794
1782	4,816	1	4,816	1	4,816
1783	1,997	1	1,997	1	1,997
1784	1,234	1	1,234	1	1,234
1785	1,064	1	1,064	1	1,064
1786	1,010	-13/6	-2,188	4,694	4,739
1787	1,065	-13/6	-2,307	4,694	4,998
1788	1,039	-13/6	-2,253	4,694	4,880
Totals			$\bar{N} = 18325$		$\sigma^2 = 61443$
			$\sqrt{\bar{N}} = 135$		$\sigma = 248$

Table A-1 The data in Figure A-1 is listed, along with intermediate numbers used in calculation of peak area and variance.

Appendix B

Calculations of Neutron Spectra in Infinite Media

In the course of the project, some insights were gained by looking at infinite media calculations of neutron spectra. Ten sets of Monte Carlo calculations were performed with MCBEND, using a 14 MeV point source. The neutrons are scored in 272 energy bins, with the upper boundary of the highest bin at 14.6 MeV and the upper boundary of the lowest bin at 8.85×10^{-11} MeV. Each of the bins has

$$\frac{E_{upper}}{E_{lower}} = 1.1$$

The average flux is tallied in each of ten concentric spherical shells between the following eleven radii:

0, 5, 10, 15, 20, 30, 40, 50, 60, 70, and 100 cm.

The uppermost curve on each plot represents the average flux between 0 and 5 cm radius. The lowermost curve on each plot represents the average flux between 70 and 100 cm radius. The vertical scale on the plots has units "neutrons per cm^2 per source neutron per bin".

Calculations were performed for the following materials:

Dolomite 0, 1, 5, 10, and 15 pu

(Ca,Mg)CO₃ $\rho_b = 2.87$ with fresh-water filled porosity

Water

Quartz sandstone 30 pu

SiO₂ $\rho_b = 2.65$ with fresh-water filled porosity

Arkose 22 hydrogen index

mineral	weight percent
quartz	38.5
feldspar	25.4
calcite	2.6
kaolinite	2.6
illite	15.8
smectite	6.1
gadolinium	2.5×10^{-4}
water	9.0

Salty arkose 22 hydrogen index

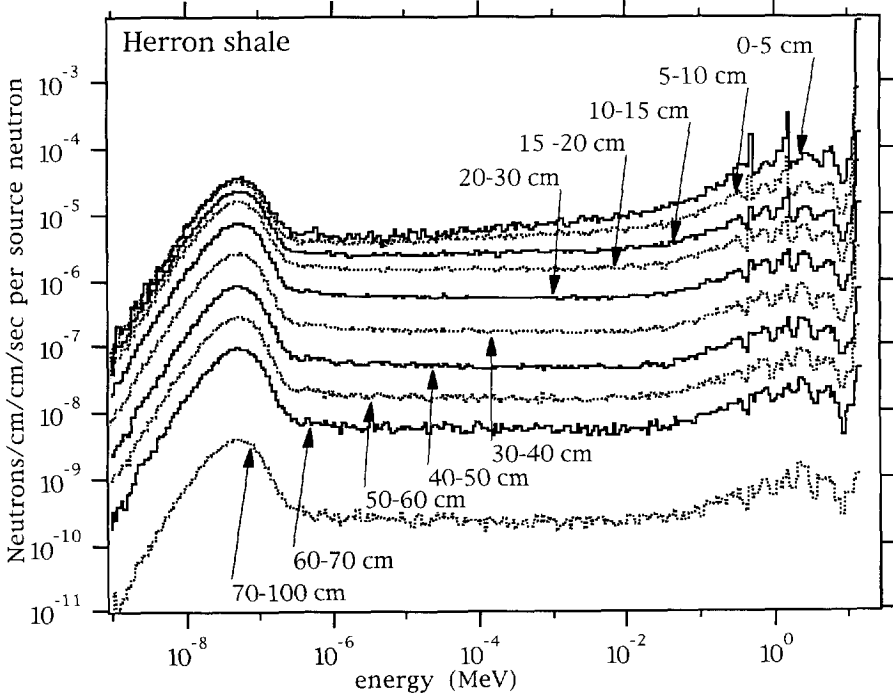
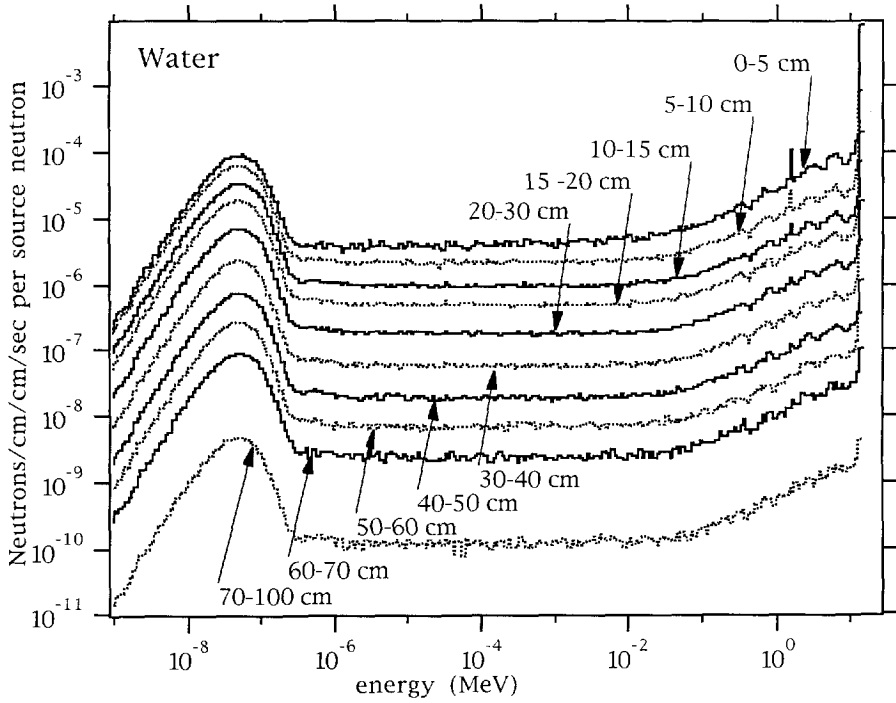
mineral	weight percent
quartz	38.3
feldspar	25.2
calcite	2.6
kaolinite	2.6
illite	15.7
smectite	6.1
gadolinium	2.5e-4
saltwater	9.4

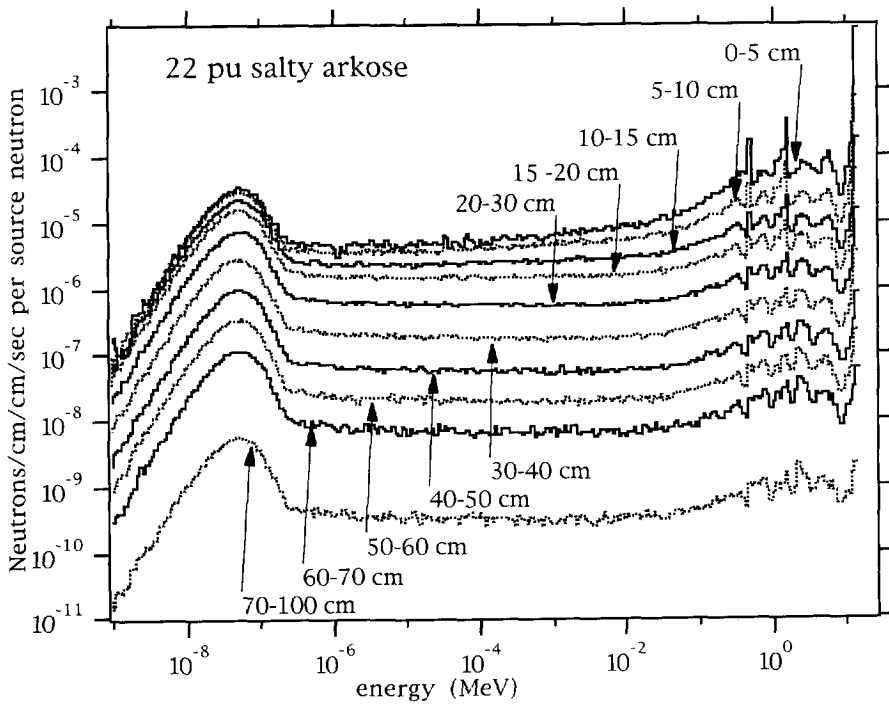
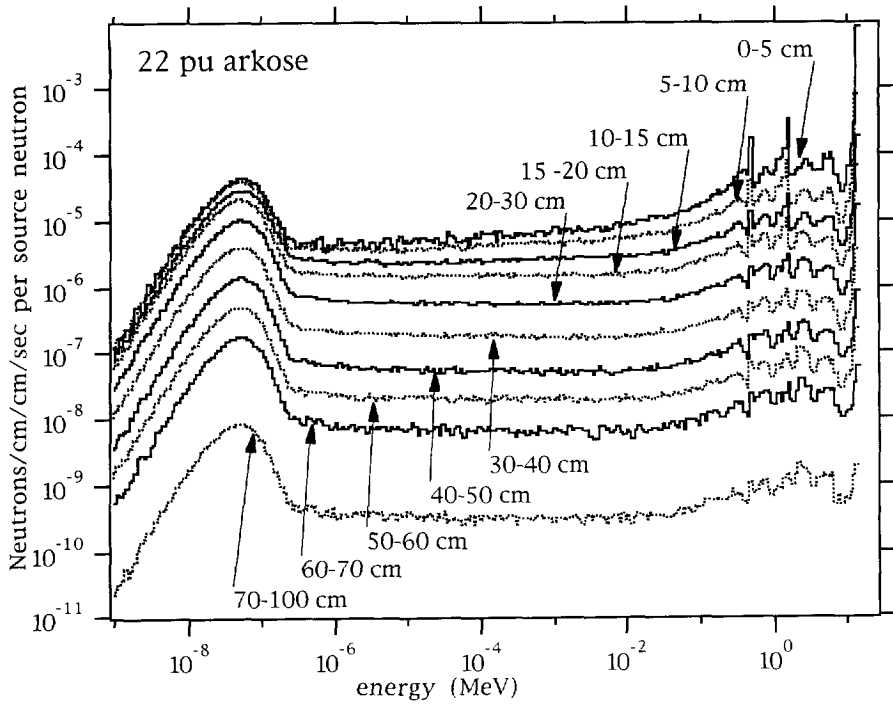
The Herron shale

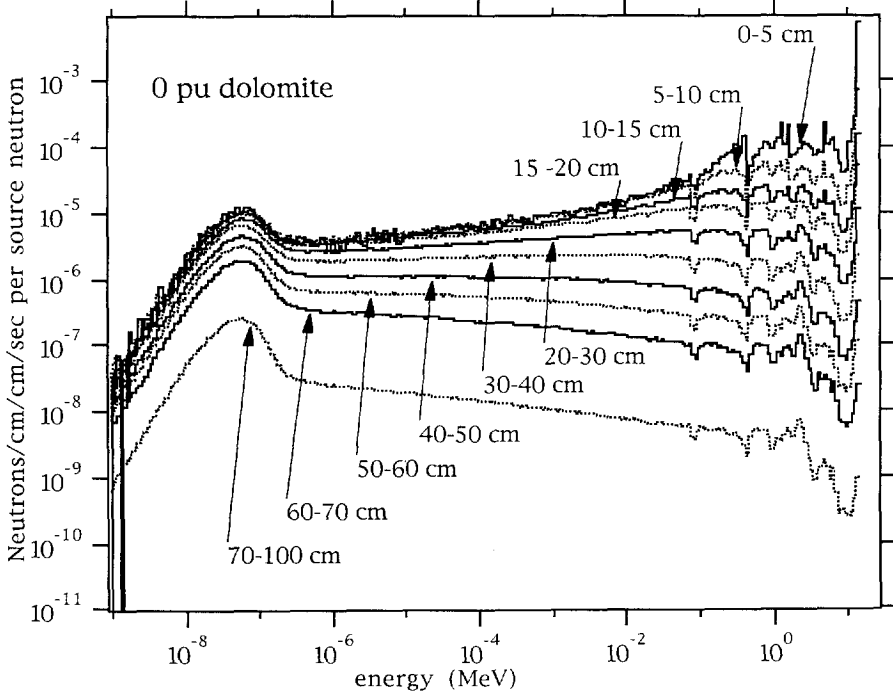
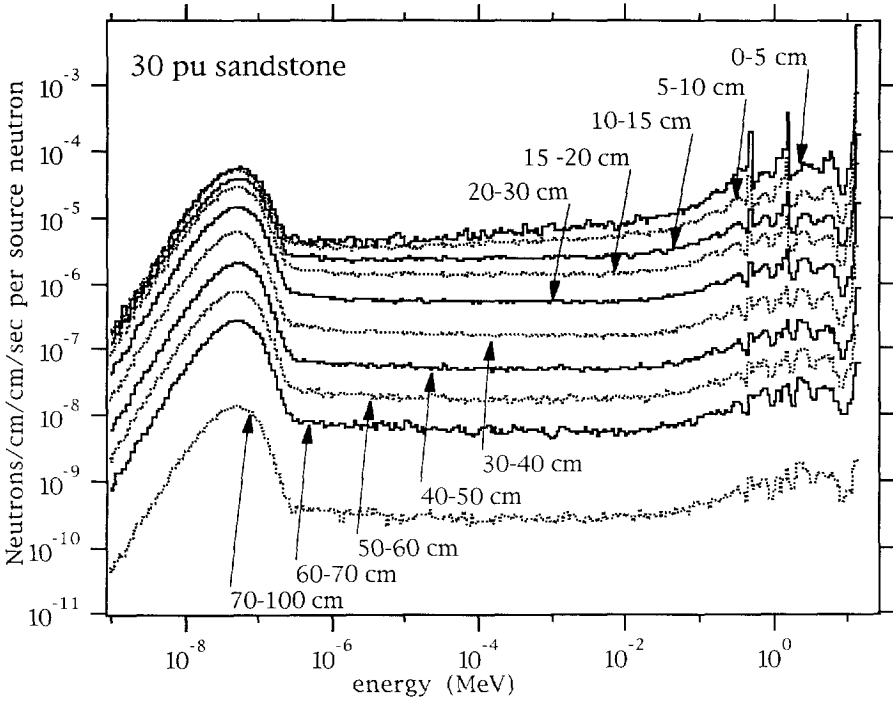
mineral	weight percent
quartz	23.0
feldspar	8.6
calcite	0.4
kaolinite	9.6
illite	42.1
smectite	11.5
pyrite	0.3
rutile	0.3
gadolinium	6.3e-6
water	4.2

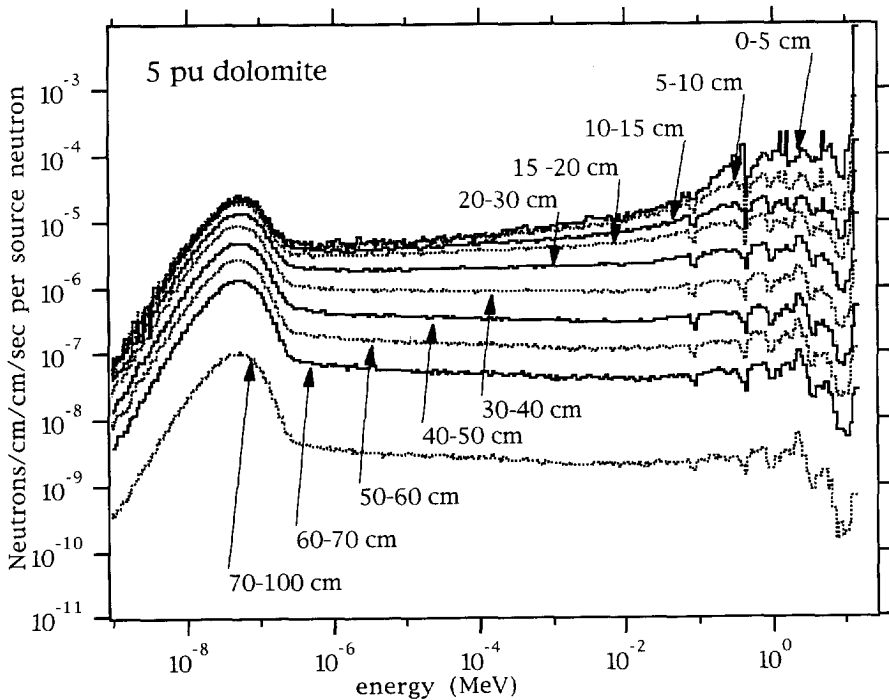
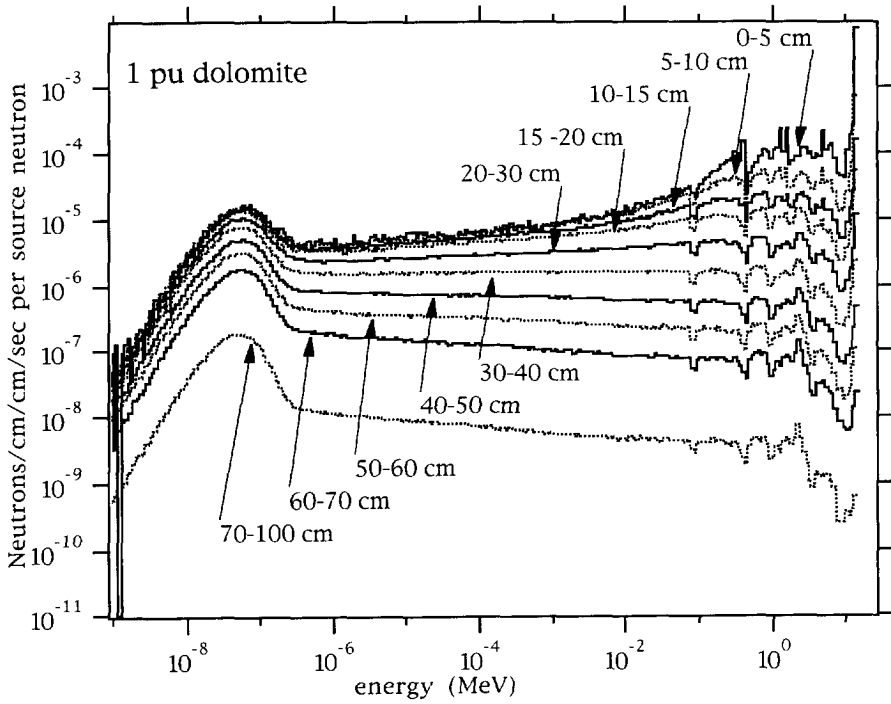
The minerals used in these rocks

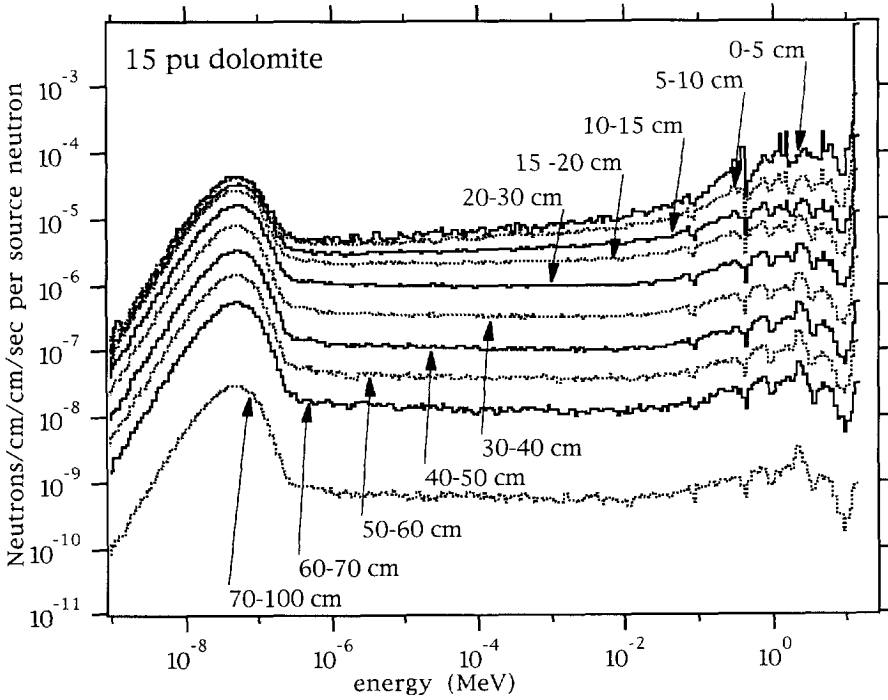
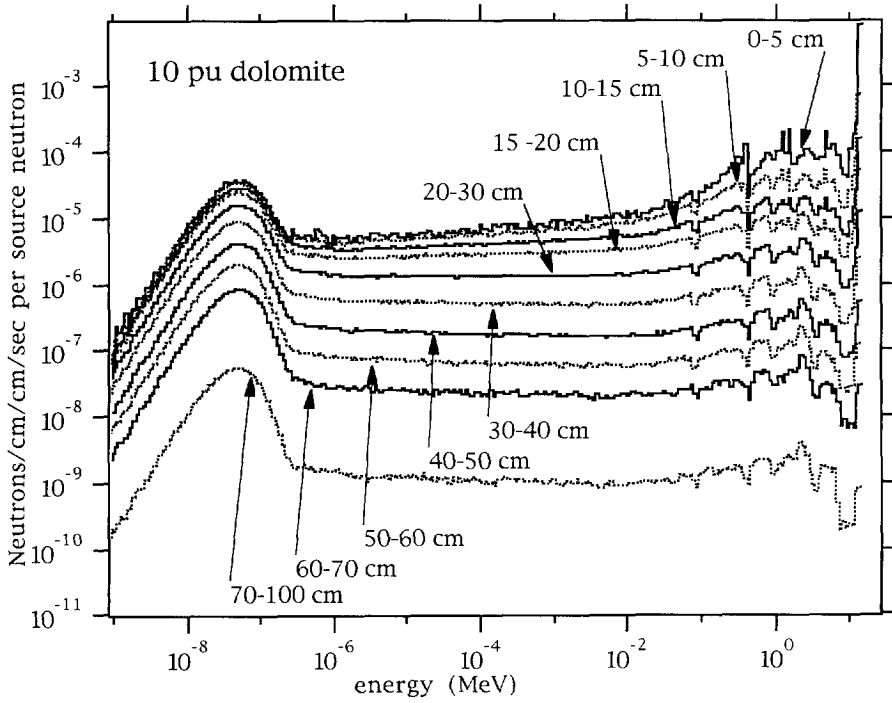
mineral or element	ρ_b g/cc	elemental percent by weight											
		Si	O	K	Ca	Al	C	Fe	Ti	H	S	Na	Cl
quartz	2.65	46.7	53.3										
feldspar	2.59	30	49	10	1	1							
calcite	2.71		48		40		12						
kaolinite	2.59	22	55.7			19		0.8	0.9	1.5			
illite	2.64	24	48.3	4		14		8	0.8	0.89			
smectite	2.06	22	63.5	0.5	0.2	9		1	0.2	3.55			
pyrite	5.01							47				53	
rutile	4.25		40						60				
gadolinium	7.89												
water	1.0												
saltwater	1.06		82.2							10.3		3.0	4.6











Appendix C

Germanium Detector and Signal Electronics

Details of the germanium signal electronics, the analog-to-digital conversion, and a drawing of the cryostat assembly are included in this section. A standard Ortec preamplifier contained within the detector package (figure C-2) has its output directed to an Ortec 632 shaping and spectroscopy amplifier (Figure C-1). Standard input and pole zero circuitries of the spectroscopy amplifier are used, along with the automatic pole zero compensation setting, to accommodate the 50 μsec decay constant of the preamplifier pulse, which is driven through 3 meters of cable. With a setting of 6 μsec pulse shaping, individual outputs from the amplifier have a total pulse width of 20 μsec . The spectroscopy amplifier gain is adjusted so that there is 1 keV width in each of the 4K pulse height channels used in a Canberra 8077S module, containing a 450 MHz Wilkinson-type ADC.

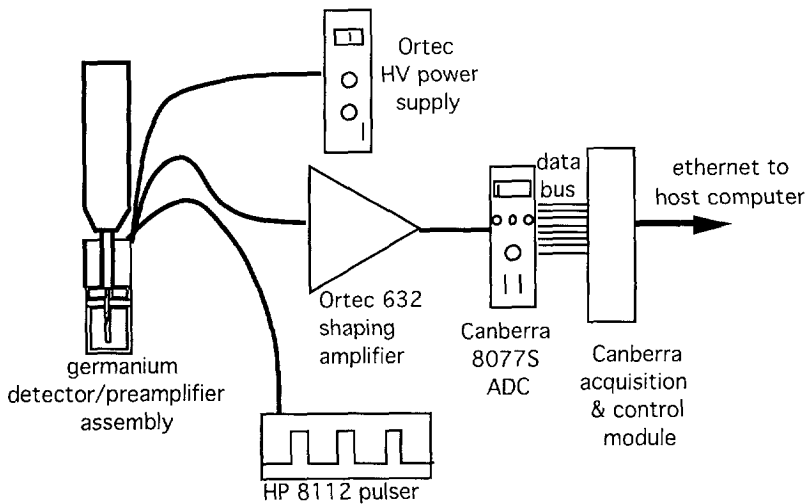


Figure C-1 The high resolution spectroscopy system includes constant-rate-and-amplitude pulse injection at the preamplifier output for monitoring of pulse pileup.

Conversion time for the ADC is quoted by the manufacturer as $1.7 \mu\text{sec} + 0.0022 \mu\text{sec}$ per channel, which amounts to $4.6 \mu\text{sec}$ for the 1333 keV gamma ray (and $10.5 \mu\text{sec}$ for a 4000 keV gamma ray). The beginning of conversion time is at the apex of the pulse. So with a setting of $6 \mu\text{sec}$ shaping time, the fall time of the pulse is greater than the conversion time, and total system dead time of $20 \mu\text{sec}$ is determined by the pulse width. Shorter pulse shaping ($3 \mu\text{sec}$) results in less system dead time and a closer match between the fall time of the pulse and the conversion time, but at the cost of substantial degradation of the energy resolution. Longer pulse shaping ($12 \mu\text{sec}$) would provide only a marginal improvement in energy resolution at the considerable expense of pulse pileup and doubling of system dead time. Pulse shaping of $6 \mu\text{sec}$ is a good compromise. No active baseline restoration circuitry is required in the amplifier because of the low count rates.

If 16K channels are used with the same gain setting of the shaping amplifier, the system resolution is found to be 2.3 keV FWHM for 1.333 keV gamma rays. The ADC has very little degrading effect upon the resolution since each ADC channel corresponds to 0.25 keV in this configuration, or about one-ninth the FWHM. Degradation effects are added in quadrature, so it can be estimated that the ADC only degrades the peak resolution by 0.014 keV . When using 4K channels, the resolution will be degraded to 2.5 keV , *on average*, in the vicinity of the 1.333 MeV peak due to the non-finite channel width. Granularity effects of the ADC channel juxtaposition with detector response may cause the resolution to be slightly better or worse. This slightly degraded resolution is acceptable because of the greatly increased system dead time and pulse pileup that would result from the use of 16K channels. Conversion times would be $13.2 \mu\text{sec}$ for the 1333 keV gamma ray and $37 \mu\text{sec}$ for a 4000 keV gamma ray, and would dominate the system dead-time. In addition a very slight statistical degradation in the background subtraction process must be accepted when using 4K rather than 16K channels.

The ADC provides a signal indicative of the system dead time to the host computer. The beginning of a pulse is sensed by a discriminator in the ADC and represents the onset of dead-time. An "ADC busy" signal is provided to the host computer. When the conversion is complete and the level of the sensed pulse falls beneath the discriminator level, the "ADC busy" signal is turned off. The host computer is set up to keep track of "ADC busy" time for every five seconds of active data acquisition, providing a means for dead time correction.

A pulser provides a signal of fixed rate and amplitude that is mixed with the output stage of the detector preamplifier, resulting in "virtual" events in

Details of the neutron monitor configurations are contained in this section. Three neutron detectors are used to monitor the flux in different regions of the energy spectrum. A bare proportional counter of dimensions 6 X 25 mm, with 10 atmospheres ^3He gas pressure is used to record the thermal flux. A similar detector, clad with 0.6 mm cadmium, is sensitive to the flux somewhat above 0.5 eV. Both these detectors are operated in the plateau mode at +900 VDC. Their signals are routed to Canberra 1706 preamplifiers (see Figure D-1) modified for fast fall times of about 15-20 μsec and then to Tennelec 205A shaping amplifiers whose input circuitry has been modified to accept the faster signals. Shaping times of 0.25 μsec result in a Gaussian-shaped pulse whose full width at the base is under 1.3 μsec , meaning that at count rates of 35,000 per second as typically seen by the thermal neutron detector, system dead time is 4.5%. Count rates in the epithermal detector are only about one-tenth that of the thermal detector.

Outputs from the shaping amplifier are driven over 30 m of cable to the control room and discriminated in a LeCroy 623B module before being routed to a multichannel scaler. The response of the ^3He tubes is nearly linear to the neutron intensity in this range of dead time. However, dead-time corrections are applied to the detector data. The dead-time corrections are based on the measured pulse width and a measurement of system dead time using the two-source method.

The third detector is a 10 X 10 mm plastic scintillator coupled to a 13 mm photomultiplier, employing a feedback gain stabilization system, for measurement of the 14 MeV flux. The photomultiplier, operated at negative high voltage in the range of 1000 VDC, has its output routed to a Canberra 150 spectroscopy preamplifier and then to a Tennelec 205A shaping amplifier. The circuitry of both amplifiers has been modified to handle faster shaping of the photomultiplier pulses. Output of the shaping amplifier is split three ways, one of which is routed to the control room where a Wilkinson-type ADC records the pulse height spectrum (Figure D-2) in several contiguous acquisition gates during the irradiation time. These data are currently only being used for diagnostic examination of the plastic scintillator acquisition system.

The other two shaping amplifier outputs are routed to window discriminators, whose window levels are open to different regions of the pulse

height spectrum, essentially a flat part and a sloping part. Discriminator outputs provide feedback to an electronics module that controls the operating voltage of the photomultiplier tube; the module continuously adjusts the high voltage if necessary, maintaining a constant ratio between counts in the two different spectral regions. Outputs from one of the discriminator channels, proportional to the MeV neutron flux, is driven to the control room for recording by a multichannel scaler. The response of this detector is also linear over the expected range of neutron intensity.

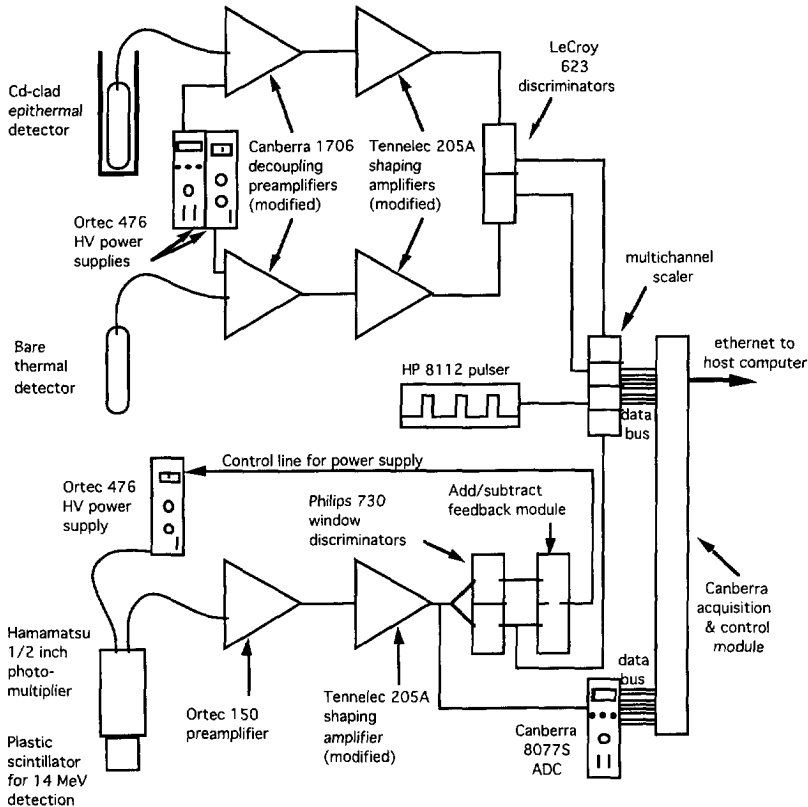


Figure D-1 The schematic of neutron monitor electronics shows three separate detector channels, plus a precision-rate pulser channel, for simultaneous recording of the detector histories during irradiation. The proportional counters are run in plateau mode, while the scintillator/photomultiplier has its gain controlled via a feedback loop. For diagnostic purposes, a pulse height spectrum from the plastic scintillator is also recorded.

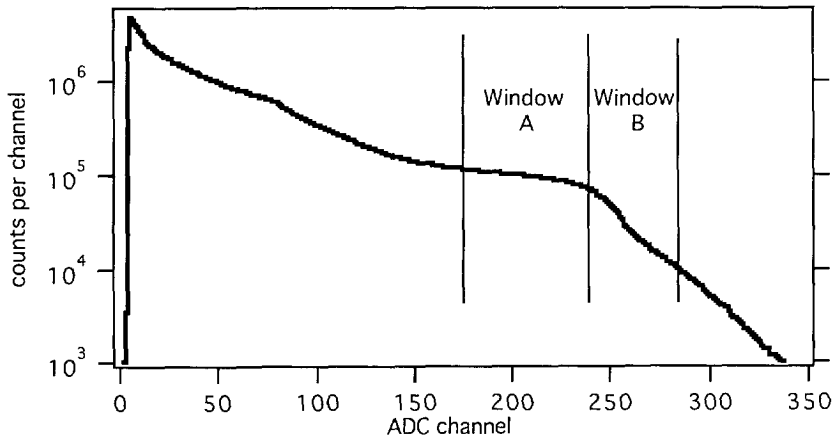


Figure D-2 Gain stabilization is accomplished in the plastic scintillator by maintaining a constant ratio between the counts in the two windows

Appendix E

Sample Constituents

This section contains descriptions and tabulations of the sample contents used in experiments. Materials used were pure enough that there would be no measurable contribution to the recorded gamma rays from competing reactions. Powders of purified chemical compounds were obtained from commercial suppliers. These compounds, or mixtures of compounds, were used for most of the samples. When mixtures were used, complete mixing was ensured by an electric mixer which rolled and tilted the sample container for several hours. The sample bottles were all filled to the same level to minimize geometrical inconsistencies between experiments. Following is a list of the constituents of samples used in the research.

element	mass (g)	wt %
---------	----------	------

Mix G	silica powder	
Si	190.21	46.7
O	216.75	53.3
	406.96	100

Mix I	alumina powder	
Al	184.68	52.9
O	164.26	47.1
	348.94	100

Mix L	sodium carbonate powder	
Na	143.97	43.4
C	37.61	11.3
O	150.29	45.3
	331.86	100

Mix M	magnesium oxide powder	
Mg	79.45	60.3
O	52.3	39.7
	131.75	100

element	mass (g)	wt. pct.
---------	----------	----------

MIX 4		
Ca	156.50	40.0
C	46.90	12.0
O	187.42	48.0
	390.82	100.0

MIX 5		
Mg	12.09	5.4
O	116.01	52.0
Si	94.84	42.5
	222.94	100.0

MIX 6		
Al	1.49	1.1
Ca	54.32	39.2
C	16.28	11.8
O	66.37	47.9
	138.46	100.0

MIX 7		
Al	4.57	3.0
Ca	57.21	37.8
C	17.14	11.3
O	72.58	47.9
	151.50	100.0

MIX 8		
Si	196.45	46.7
O	223.82	53.3
	420.27	100.0

MIX 9		
Na	23.85	6.3
C	6.23	1.6
O	197.96	52.1
Si	151.90	40.0
	379.93	100.0

element	mass (g)	wt. pct.
---------	----------	----------

MIX 10		
Mg	8.75	5.6
Ca	52.77	33.7
C	16.99	10.9
O	73.67	47.0
	156.70	100.0

MIX 11		
Al	1.46	0.9
Na	6.54	3.9
Ca	60.62	35.8
C	19.87	11.7
O	80.72	47.7
	169.21	100.0

MIX 12		
C	20.53	12.0
Ca	68.51	40.0
O	82.04	48.0
	171.08	100.0

MIX 13		
Ca	55.77	33.6
C	16.71	10.1
O	73.95	44.6
V	0.11	660 ppm
Cu	2.80	1.7
Fe	16.48	9.9
	165.82	100.0

MIX 14		
Ca	63.47	38.1
C	20.53	12.3
O	80.14	48.1
H	0.44	0.3
Co	1.85	1.1
Cr	0.12	715 ppm
	166.56	100.0

element	mass (g)	wt. pct.
---------	----------	----------

MIX 15		
C	16.31	11.0
O	72.47	48.9
Mn	0.47	0.3
Ni	2.43	1.6
S	1.60	1.1
H	0.52	0.4
	148.21	100.0

MIX 16		
Ca	73.66	38.7
C	22.07	11.6
O	88.21	46.3
K	2.17	1.1
Br	4.44	2.3
	190.56	100.0

MIX 17		
Ca	74.02	40.0
C	21.46	11.6
O	85.76	46.4
K	0.35	0.2
I	1.15	0.6
F	2.28	1.2
	185.03	100.0

MIX 18		
Ca	66.33	35.0
C	19.88	10.1
O	87.12	46.0
Ti	5.76	3.0
Ba	8.27	4.4
S	1.92	1.0
	189.28	100.0

MIX 19		
Ca	74.62	39.0
C	22.36	11.7
O	90.31	47.2
Au	0.35	0.2
H	0.01	0.0
Ag	2.91	1.5
S	0.43	0.2
Cl	0.25	0.1
	191.24	100.0

element	mass (g)	wt. pct.
---------	----------	----------

MIX 20		
Si	164.11	46.7
O	186.97	53.3
	351.08	100.0

MIX 21		
Ca	79.89	21.7
Mg	48.46	13.2
C	47.88	13.0
O	191.34	52.1
	367.57	100.0

MIX 22		
Al	204.26	52.9
O	181.68	47.1
	385.95	100.0

MIX 23		
Ca	61.52	37.0
C	18.44	11.1
O	76.93	46.3
Zr	9.26	5.6
	166.15	100.0

MIX 24		
Ca	69.38	39.6
C	20.79	11.9
O	83.45	47.7
Te	1.44	0.8
	175.05	100.0

MIX 25		
Ca	66.92	37.9
C	20.06	11.4
O	82.89	46.9
Se	6.79	3.8
	176.66	100.0

MIX 26		
Ca	67.21	38.9
C	81.23	47.0
O	20.14	11.7
La	4.25	2.5
	172.83	100.0

element	mass (g)	wt. pct.
---------	----------	----------

MIX 27		
Ca	53.12	38.5
C	15.92	11.5
O	64.96	47.1
Ga	3.92	2.8
	137.92	100.0

MIX 28		
Ca	54.91	38.6
C	16.46	11.6
O	67.43	47.4
Mo	3.35	2.4
	142.15	100.0

MIX 29		
Ca	52.97	37.8
C	15.90	11.4
O	65.10	46.5
Sr	0.23	0.2
W	5.91	4.2
	140.10	100.0

MIX 30		
Ca	55.57	38.4
C	17.04	11.8
O	68.33	47.2
Sr	2.82	2.0
W	0.91	0.6
	144.66	100.0

MIX 31		
Ca	55.36	38.8
C	16.59	11.6
O	67.26	47.1
Hf	0.07	0.1
Sn	3.53	2.5
	142.82	100.0

MIX 32		
Ca	56.03	39.4
C	16.79	11.8
O	67.55	47.5
Hf	0.76	0.5
Sn	1.15	0.8
	142.28	100.0

Appendix F

Isotopic and Nuclear Data

Activation cross sections used in the Monte Carlo calculations are from the IRDF-85 (IAEA-NDS-41) compilations. The data are in the SAND-II scheme, which uses 641 energy groups from 20 MeV to 10^{-10} MeV.

The following table of cross section values for Na, Mg, Al, and Si, for 14.5 MeV neutrons and thermal neutrons, are taken from Gerhard Erdtmann's book of neutron activation data [33].

initial nuclide	reaction	intermediate nuclide	Q-values (MeV)	14.5 MeV x-sect (barns)	thermal (0.0253 eV) x-sect (barns)
²³ Na	(n,γ)	²⁴ Na	+6.96	-	400 ± 30 mb
²⁴ Mg	(n,p)		-4.73	190 ± 19 mb	-
²⁷ Al	(n,α)		-3.13	116 ± 3 mb	-
²⁶ Mg	(n,γ)	²⁷ Mg	+6.44	-	38.2 ± 0.8 mb
²⁷ Al	(n,p)		-1.83	75 ± 8 mb	-
³⁰ Si	(n,α)		-4.20	70 ± 10 mb	-
²⁷ Al	(n,γ)	²⁸ Al	+7.73	-	232 ± 3 mb
²⁸ Si	(n,p)		-3.86	230 ± 30 mb	-
²³ Na	(n,p)	²³ Ne	-3.59	43 ± 6 mb	-
²⁶ Mg	(n,α)		-5.41	77 ± 8 mb	-
²³ Na	(n,α)	²⁰ F	-3.87	150 ± 15 mb	-
²⁵ Mg	(n,p)	²⁵ Na	-3.05	44 ± 5 mb	-
²⁹ Si	(n,p)	²⁹ Al	-2.90	120 ± 20 mb	-

Isotope ratios used in analysis of the experimental data for Na, Mg, Al, and Si are taken from Gerhard Erdtmann's book of neutron activation data [33].

Isotope	Abundance (%)
²³ Na	100
²⁵ Mg	78.99
²⁶ Mg	10.00
²⁷ Mg	11.01
²⁷ Al	100
²⁸ Si	92.2
²⁹ Si	4.7
³⁰ Si	3.1

Acknowledgements

My spouse, Judy, and two young children, Katherine and Meredith, have been patient and supportive while I have been away from home most of the time these last few years. Their tolerance has enabled the completion of this project. I thank them, and expect to spend much more time with them, hoping that their patience will continue. My 11 year old daughter, Katherine, also performed duty as a laboratory assistant and accelerator operator in the past few years, for which I also thank her.

Jeff Schweitzer has been involved in the project from start to finish, from his conception of the research to the final proofreading. His scientific and political creativity in keeping the project on track, as well as the many hours he spent, are greatly appreciated.

The involvement and interest of the promotor, Professor Peter Ypma, has also spanned the duration of the research project. His straightforward and energetic approach to research issues, and his ability to look beyond the red tape of small problems has led to the timely completion of this thesis.

I wish to express my gratitude to Joel Groves, who advised me at the onset of the project that the demands on my time would be most problematic, and that it would be very difficult to complete the research and thesis because of these demands. In the next breath, he became a strong sponsor and advocate for me with the Schlumberger management, despite the demands it would place on him.

While spending several months at Delft Technical University, I had the good fortune to share the office of Professor Max Peeters, who is also a co-promotor of the research. His enthusiasm for the project and personal good will provided a substantial help for efforts at Delft and Schlumberger. Exhaustive, critical, and practical reviews of draft thesis versions have been most helpful.

While at Delft, I spent many daylight and evening hours with Oscar Kelder, who has selflessly devoted much time and effort in taking care of details. I am surely not even aware of matters he has quietly handled in the past year.

Peter Wraight has been instrumental in completion of the thesis by enabling me to spend several months at Delft, where I could work uninterrupted by the demands of Schlumberger. I thank him for these opportunities.

I thank Thijs Rademaker, who patiently and meticulously translated the summary of the thesis into Nederlands.

Finally, I thank my colleague, advisor, editor, and friend, Darwin Ellis. He has constantly pushed me toward completion of the thesis.

Curriculum vitae

- 1954 Born in Pipestone, Minnesota USA
- 1973-1975 Engineering studies at North Hennepin College, Minneapolis,
Minnesota
- 1975-1978 B. S. in Geological Engineering at University of Minnesota
- 1978-1980 Mining engineer at U. S. Bureau of Mines in Minneapolis,
Minnesota
- 1980-1985 Well-logging engineer at Schlumberger field office in
Pleasanton, Texas
- 1985-1988 Development engineer at Schlumberger Houston Downhole
Sensors in Houston, Texas
- 1985-1987 Graduate studies in Petroleum Engineering at University of
Houston in Houston, Texas
- 1988-1994 Associate research scientist at Schlumberger-Doll Research in
Ridgefield, Connecticut
- 1988-1991 M. A. in Oceanography and Limnology at Western Connecticut
State University in Danbury, Connecticut
- 1991-1995 Research for this Ph.D. thesis at Schlumberger-Doll Research
and Delft University of Technology
- 1994-present Research scientist at Schlumberger-Doll Research in
Ridgefield, Connecticut